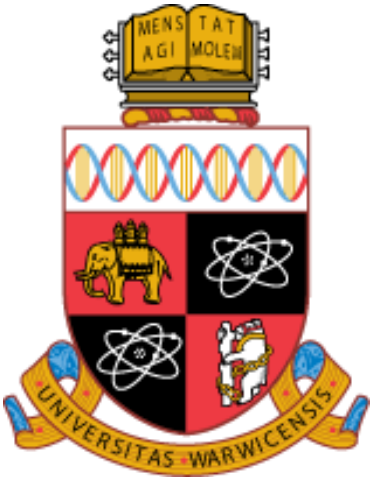

Low Thermal Conductance Platforms for mK Tunnelling Coolers

by

Chalermwat Wongwanitwattana

Thesis

Submitted to the University of Warwick

in partial fulfilment of the requirements

for admission to the degree of

Doctor of Philosophy

Department of Physics

THE UNIVERSITY OF WARWICK

Declaration

This thesis is submitted to the University of Warwick in support of my application for the degree of Doctor of Philosophy. All experimental data presented and simulations were carried out by the author, except where specially stated.

Acknowledgments

First of all, I would like to thank my supervisors Prof. E. H. C. Parker, Prof. T. E. Whall and Prof. D. R. Leadley for their valuable guidance, discussions and continual support throughout my studies. My thanks are also due to Dr V. A Shah, Dr M. Myronov and Dr M. J. Prest for their sample fabrication, experimental and data analysis support. I am very grateful to Dr Mark Crouch, Department of Engineering and Dr Aleix Guell , Department of Chemistry for clean room experimental support. I am also very grateful to all my colleague and friends for their assistance, discussions and continual encouragement.

My greatest acknowledgements go to my parents and my family without their constant reinforcement this work would not have been finished. Finally, I would like to acknowledge the Thai Government for providing a scholarship for my PhD.

Publications arising from this work

C. Wongwanitwattana, V. A. Shah, M. Myronov, E. H. C. Parker, T. E. Whall, and D. R. Leadley, "Precision plasma etching of Si, Ge and Ge:P by SF_6 with added O_2" J. Vac. Sci. Technol. A (2014), JVSTA-A-13-419R (Accepted).

V . A. Shah, M. Myronov, C. Wongwanitwattana, L. Bawden, M. J. Prest, J. S. Richardson-Bullock,S. Rhead, E. H. C. Parker, T. E. Whal, and D. R. Leadley, "Electrical isolation of dislocations in Ge layers on Si(001) substrates through CMOS-compatible suspended structures", Sci. Technol. Adv. Mater. 13 (2012) 055002.

C. Wongwanitwattana, V. A. Shah, M. Myronov, E. H. C. Parker, T. E. Whall, and D. R. Leadley, "Accurate reactive ion etching of Si, Ge and P doped Ge in an SF_6-O_2radio-frequency plasma ", 2012 Si, SiGe, and Related Compounds: Materials, Processing, and Devices Symposium, Honolulu, Hawaii October 7-12, 2012.

V. A. Shah, M. Myronov, C. Wongwanitwattana, R. J. H. Morris, M. J. Prest, J. S. Richardson-Bullock,S. Rhead, E. H. C. Parker, T. E. Whall, and D. R. Leadley., "Simple fabrication of suspended Germanium structures and their electrical properties from high quality Ge on Si(001) layers.", 2012 Si, SiGe, and Related Compounds: Materials, Processing, and Devices Symposium, Honolulu, Hawaii October 7-12, 2012.

V.A. Shah, M. Myronov, C. Wongwanitwattana, R.J.H. Morris, M.J. Prest, J. Richardson-Bullock, E.H.C. Parker, T.E. Whall and D.R. Leadley
"Simple fabrication of suspended germanium structures and their electrical properties from high quality Ge on Si(001) layers" International SiGe Technology and Device Meeting (ISTDM 2012), Berkeley, June 4-6, (2012)

V. A. Shah, A. Shchepetov, M. Myronov, M. J. Prest, M. Prunnila, C. Wongwanitwattana, T. E. Whall, E. H. C. Parker, and D. R. Leadley, "The Effects of Tensile and Compressive Strain on Ge Membranes", 7th International Conference on Si Epitaxy and Heterostructures (ICSI-7), Leuven, Belgium, Sept. (2011)

C . Wongwanitwattana, V. A. Shah, M. J. Prest, M. Myronov, E. H. C. Parker, T. E. Whall, and D. R. Leadley, “Electron-Phonon Interaction in P-doped Ge (Ge:P)” , (processing to submit)

Abstract

The impact of the O_2 content in SF_6-O_2 gas mixtures on the etch rate and sidewall profile of Silicon (Si), Germanium (Ge) and phosphorous doped Germanium (Ge:P) in reactive ion etching has been studied. The characteristics of etch rate and sidewall profile were greatly affected by the O_2 content. Below 50% of O_2 content, a large variation in Ge etch rates was found compared to that of Si, but for O_2 content above 50% the etch rates followed relatively the same trend. Lightly doped Ge showed the highest etch rate at a O_2 concentration up to 20%. Sidewall angles range from a minimum of 80° to a maximum of 166°, with O_2 concentration of 20% yielding perfect anisotropic mesa etch. Also at this O_2 concentration, reasonable Si/Ge selectivity was possible. These observations indicate that by adjusting the O_2 concentration, precision plasma etching of Si, Ge and Ge:P was possible.

Suspended Ge structures were fabricated: micro wires, spiderweb and the van der Pauw Greek-cross. The micro wires' size could be reduced to fabricate suspended Ge nanowires devices. The suspended spiderweb could be fabricated for bolometers. The van der Pauw Greek-cross structure could reveal the electrical properties of thin expitaxial layer such as resistivity and mobility via hall measurement as a function of temperature. Removal of dislocations was shown to enhance the electrical isolation.

Thermal properties of germanium doped with phosphorus ($4x10^{19}$ cm^{-3}) were investigated in this study. At lowest T_{bath} of 312 mK , the results indicate that heat flow from hot electrons to phonons was proportional to T^7 and the electron-phonon coupling constant is $1.31x10^9$ W/m^3K^7. The temperature dependence of doped Ge was higher than doped Si (which has a T^6 temperature dependence) because the band structure was different. Moreover, the heat flow between electrons and phonon that is proportional to T^7 could possibly be explained by a combination of strong disorder and surface modes.

Contents

User's Declaration.....i
AUTHOR: Chalermwat Wongwanitwattana DEGREE: Ph.D......i
TITLE: Low Thermal Conductance Platforms for mK Tunnelling Coolers.....i
AUTHOR'S SIGNATURE.....i
USER'S DECLARATION.....i
Declaration..... iii
Acknowledgments.....iv
Publications arising from this work.....v
Abstract.....vii
Contents..... viii
List of Figures.....xi
List of Table.....xvii
List of Abbreviations..... xviii
List of Variable.....xx
1 Introduction.....1
1.1 Background to the research.....1
1.1.1 The need for low temperature operation.....1
1.1.2 Conventional cryogenics.....1
1.1.3 Electronic cooling via tunnel junctions.....2
1.1.4 Semiconductor based cooler junctions.....4
1.1.5 Platform cooling.....5
1.2 Objectives of this research.....5
1.3 Chapter summaries.....6
2 Background Theory.....8
2.1 Germanium and application.....8
2.2 Thermal conductivity.....10
2.2.1 Kinetic theory of gases.....11
2.2.2 Drude model.....11
2.2.3 Lattice thermal conductivity.....12
2.2.4 Phonon dimensionality.....18
2.3 Tunnel junction coolers.....21

2.3.1 The normal-insulator-superconductor (NIS) tunnel junction 22
2.3.2 The double junction SINIS structure 25
2.3.3 The superconductor-semiconductor-superconductor (S-Sm-S) tunnel junction 27
2.4 Electron-Phonon coupling 30
2.5 Dislocations in crystals 34
3 Experimental Techniques 39
3.1 Introduction 39
3.2 Epitaxial growth of crystalline semiconductors 39
3.2.1 Molecular beam epitaxy (MBE) 40
3.2.2 Chemical vapour deposition (CVD) 42
3.3 Material characterization 45
3.3.1 Electron microscope (EM) 45
3.3.1.1 The scanning electron microscope (SEM) 46
3.4 Device fabrication 51
3.4.1 Photolithography 51
3.4.2 Etching 53
3.4.3 Etch rate 55
3.5 Electrical characterisation 59
3.5.1 Hall measurement 59
3.5.2 Mobility measurement 62
4 The Dry Etching Process in SF_6-O_2 Radio-Frequency Plasma 63
4.1 Introduction 63
4.2 Wafer growth and trench etching procedure 66
4.3 Etch rate 68
4.4 Sidewall profile 71
4.5 Conclusion 78
5 Creation of Suspended Ge Structure 79
5.1 Introduction 79
5.2 Sample fabrication 81
5.2.1 Photolithography 81
5.2.2 Wet etching 82
5.3 Results and discussion 84

5.3.1 Suspended micro wire 84
5.3.2 The suspended spiderweb 86
5.3.3 The van der Pauw Greek-cross 89
5.3.4 Suspended membrane 90
5.3.5 Nanotube 92
5.4 Electrical conductivity measurement 94
5.5 Conclusion 98
6 Electron-Phonon Interaction in P-doped Ge (Ge:P) 100
6.1 Introduction 100
6.2 Experiment 102
6.2.1 Experimental outline 102
6.2.2 Measurement of electron temperature 103
6.2.3 Measurement of electron-phonon coupling 107
6.3 Discussion 112
7 Conclusions and Further Work 114
7.1 Conclusion 114
7.1.1 The dry etching process of Ge in a SF_6-O_2 radio-frequency plasma 114
7.1.2 Creation of suspended Ge structure 117
7.1.3 Electron-Phonon (EP) interaction in P-doped Ge (Ge:P) 118
7.2 Further work 120
7.2.1 The dry etching process of Ge in SF_6-O_2 radio-frequency plasma 120
7.2.2 Creation of suspended Ge structure 120
7.2.3 Electron-Phonon (EP) interaction in P-doped Ge (Ge:P) 121
Bibliography 122
Appendix A 132
Appendix B 137

List of Figures

Figure 2.1: The phonon dispersion curves for Ge [From Ref. 35].....13

Figure 2.2: The thermal conductivity of germanium (Ge_1) and silicon (Si_1) as a function of temperature on a logarithmic scale. The inset shows the same curve plotted on a linear scale. [From Ref. 39] 16

Figure 2.3: The lattice thermal conductivity of Si and Ge versus temperature, (a) The lattice thermal conductivity of Si as a function of temperature (b) The lattice thermal conductivity of Ge as a function of temperature. [From Ref. 40].....17

Figure 2.4: The comparison of the lattice thermal conductivity of Si with theory in which various phonon scattering mechanism. [From Ref. 40].....18

Figure 2.5: The branches of dispersion relations of phonon eigenmodes (a) *h*-modes (b) *s*-modes (c) *a*-modes [From Ref. 42].....19

Figure 2.6: The three lowest branches in the long wavelength limit [From Ref. 42].....20

Figure 2.7: (a) The full membrane, l_1 xl_2 μm^2 (b) the bridge form, *w* width, cutting from (a) [From Ref. 43] 20

Figure 2.8: Thermal conductivity of silicon nitride, full membrane (circles) $\kappa \propto T^2$, bridge form(triangles) $\kappa \propto T^{3/2}$ Inset represents a typical dc measurement in the bridge [From Ref. 43] 21

Figure 2.9: The energy diagram of the normal-insulator-superconductor(NIS) tunnel junction, Δ is a half-band gap and V is a bias voltage. [From Ref.47].....22

Figure 2.10: The I-V characteristic of NIS thermometer at various relative temperature T/T_C where T_C the transition temperature. [From Ref. 55].....25

Figure 2.11: Energy diagram of SINIS junction. [From Ref. 59] 26

Figure 2.12: (a) The I-V characteristic of SINIS thermometer. The horizontal dashed lines are the constant current bias I= 500pA and I=10pA. (b) The two black circles are the calibration curves of SINIS thermometer, BCS theory with Δ(T): grey line, BCS theory with Δ(0): red dashed line. [From Ref. 60].....26

Figure 2.13: The energy diagram of the superconductor-semiconductor-superconductor.....27

Figure2.14: (a) The I-V characteristics of the superconductor-semiconductor-superconductor(S-Sm-S) tunnel junction at different temperatures. (b) The temperature calibration curve. [From Ref. 66] 29

Figure 2.15: Schematic illustration of the Si intervalley, six-fold degenerate [From Ref. 76]32

Figure 2.16: Schematic diagram of the growth of a lattice mismatched layer under (a) compressive and (b) tensile strain. [Adapted from Ref. 88].....35

Figure 2.17: A physical representation of the threading and misfit dislocations as the boundary of a slipped plane which shows the order of bonds which are broken. [Adapted from Ref. 89].....36

Figure 3.1: MBE-V90S-ANT at Nanosilicon group, Department of Physics, University of Warwick.....41

Figure 3.2: The diffusion of adatoms on the hot substrate surface to form the layer. [From Ref. 103] 42

Figure 3.3: Schematic of a typical cold wall CVD reactor [From Ref. 108].....43

Figure 3.4: LP-CVD-ASM Epsilon 2000E at Nanosilicon group, Department of Physics, University of Warwick.....43

Figure 3.5: Sequence of events during CVD: (a) diffusion of reactants through boundary layer, (b) adsorption of reactants on substrate, (c) chemical reaction takes place,

(d) desorption of adsorbed species, and (e) diffusion out of by-products through boundary layer [From Ref. 109].....44

Figure 3.6: The structure of a scanning electron microscope (SEM) [From Ref. 110].....47

Figure 3.7: Comparison of light microscope with scanning electron microscope at the same magnification a) light microscope image b) SEM image [From Ref. 111].....47

Figure 3.8: The SEM, Zeiss Supra InLens secondary electron detector at Department of Physics, University of Warwick 49

Figure 3.9: The Specimen (a) Full size specimen (b) Cleaved specimen.....49

Figure 3.10: The slotted head for mounting specimen 50

Figure 3.11: The SEM holder 50

Figure 3.12: The top view look like seen by InLens of SEM.....50

Figure 3.13: The basics process of photolithography: (a) Photoresist deposition (b) Photoresist exposure (c) Development (d) SiO_2 sample etching process (e) Photoresist removment [From Ref. 114] 52

Figure 3.14: Wet etching process.....53

Figure 3.15: Plasma interaction with the surface [From Ref. 115].....54

Figure 3.16: a) Patterned mesa array using photolithography b) Plasma dry etching with SF_6-O_2 c) Removal of photoresist.....56

Figure 3.17: The step height of array of mesas that was measured by Ambios XP-100 step profilometer for calculation of the etching rate, etched by SF_6-O_2 gas mixture (30 sccm) : (a) 5% O_2 (b) 20% O_2 (c) 35% O_2 (d) 50% O_2 (e) 70% O_2 (f) 90% O_2 of 30 sccm 59

Figure 3.18: The Hall effect in a bar of conducting material [From Ref. 117] 60

Figure 3.19: Arrangement for resistivity measurement [From Ref. 118].....61

Figure 3.20: Arrangement for Hall voltage measurement [From Ref. 119] 62

Figure 4.1: The schematics of samples : a) Ge (undoped layer) b) Ge:P[L] ($1x10^{18}$ cm^{-3}) c) Ge:P[H] ($3x10^{19}$ cm^{-3}) 67

Figure 4.2: The Ge mesa pattern using RIE, removed photoresist (PR), still have residual PR on top of mesa 68

Figure 4.3: RIE etch rates of Si and Ge as a function of percentage of O_2 in the SF_6-O_2 69

Figure 4.4: Mesa profiles produced by anisotropic and isotropic etching (PR = photoresist) : a) Isotropic b) Partially Anisotropic c) Perfect Anisotropy 71

Figure 4.5: SEM images of the surface morphology of Si mesa after dry etching with SF_6-O_2 of various O_2 percentages 72

Figure 4.6: SEM images of the surface morphology of Germanium (intrinsic) mesa after dry etching with SF_6-O_2 of various O_2 percentages 73

Figure 4.7: SEM images of the surface morphology of lightly doped germanium ($1x10^{18}$ cm^{-3}) mesa after dry etching with SF_6-O_2 of various O_2 percentages.....74

Figure 4.8: SEM images of the surface morphology of heavily doped germanium ($3x10^{19}$ cm^{-3}) mesa after dry etching with SF_6-O_2 of various O_2 percentages.....75

Figure 4.9: The anisotropic angle as a function of percentage of oxygen, dash line is eye guide line.....76

Figure 4.10: The proposed etch mechanism, (a) the F* find the site of least potential energy, the step and therefore etch slightly laterally. (b) GeO_xF_y is sputtered from the bottom surface and redeposited onto the sidewall 77

Figure 5.1: (a) dislocation(black line) acts like a wire to connect contacts, leading to electrical leakage (b) suspended structure can remove part of dislocation, and remove the leakage path 80

Figure 5.2: The smallest 2μm mesa pattern.....81

Figure 5.3: a) Ge on Si wafer b) topside and back side of Ge membrane 82
Figure 5.4: (a) The initial structures (b) The suspended micro wire (c) micro wire attached to the substrate surface due to a lack of tension.....85
Figure 5.5: The micro wire pattern is tiled by 45º to lie along the (100) direction 85
Figure 5.6: (a) The completed micro wire (b) uncompleted micro wire that presents the underneath slowest etching plane 86
Figure 5.7: The suspended spider web platform is etched by SF_6-O_2 (80%-20%) and TMAH (25wt%, 80°C) 87
Figure 5.8: The two underneath bridges in {111} 88
Figure 5.9: Some legs of spiderweb are broken due to liquid trap 88
Figure 5.10: (a)The van der Pauw Greek-cross structure (b) The centre of cross structure ..89
Figure 5.11: (a) The bridged structure, 20μm wide legs (b) Centre of the bridged structure.90
Figure 5.12: (a) Suspended cross bridge structure diagram (b) The optical images of suspended cross bridge structure 91
Figure 5.13: The Si pillar.....92
Figure 5.14: Nanotube formation (a) method I (b) method II (c) 12 μm long nanotube from method I (d) 50 nm diameter nanotube from method I (e) 12 μm long nanotube from method II [From Ref. 159].....93
Figure 5.15: The optical image of nanotube and wire 94
Figure 5.16: The SEM image of nanotube and wire, the larger sheets start to bend beneath their own weight (40μm and 50μm) 94
Figure 5.17: (a) The van der Pauw Greek-cross bulk structure (b) The centre of cross bulk structure.....95

Figure 5.18: (a) the electrical resistivity of suspended and bulk van der Pauw Greek-cross structure (b) the mobility of intrinsic carriers in suspended and bulk van der Pauw Greek-cross structure 96

Figure 6.1: Sample Geometry 102

Figure 6.2: The corresponding current *I* as a function of sample biased voltage 103

Figure 6.3: The I-V characteristics of a S-Sm-S thermometer for bath temperatures between 312 mK and 600 mK. The horizontal dashed line allows the junction voltage at different temperatures to be read off when biased by a constant 10 nA current. 104

Figure 6.4: S-Sm-S thermometer calibration curve, biased by a constant current (10 nA)...104

Figure 6.5: The electron temperature as a function of power for T_{bath} from 312 mK to 600mK 105

Figure 6.6: The electron temperature as a function of power for T_{bath} = 312 mK, with dashed lines showing regions where input power is either less than (blue) or greater than (red) the power extracted by e-ph coupling. 106

Figure 6.7: The power density removed by electron phonon coupling as a function of the excess temperature expressed as $T_e^n - T_{ph}^n$ for T_{ph}=T_{bath} = 312 mK, for different values of the exponent *n*. Dashed lines have unit gradient on this log-log plot and allow the e-ph coupling constant to be found via Equation 6.1. It can be seen that the experimental data best follow a line of unit gradient for the green points with *n*=7. 108

Figure 6.8: As Figure 6.7 for a range of different bath temperatures and with *n*=7 only. 109

Figure 6.9: Electron-phonon coupling constant extracted from Figure 6.8 for a range of bath temperatures. The line is a linear extrapolation through the data. 109

Figure 6.10: The electron-phonon thermal conductance as a function of electron temperature at 312 mK T_{bath}.....110

Figure 6.11: Noise equivalent power as a function of temperature. 111

List of Tables

Table 2.1: Carrier mobility of germanium and silicon [From Ref. 19] 9

List of Abbreviations

ACVD	Atmospheric pressure chemical vapour deposition
AFM	Atomic force microscope
BJTs	Bipolar junction transistors
CMOS	Complementary metal–oxide–semiconductor
CVD	Chemical vapour deposition
DRAM	Dynamic random access memory
EM	Electron microscope
EP scattering	Electron phonon scattering
FIM	Field ion microscope
LEDs	Llight emitting diodes
LPCVD	Low pressure chemical vapour deposition
MBE	Molecular beam epitaxy
MEMS	Microelectromechanical structures
MOCVD	Metal organic chemical vapour deposition
NEP	Noise equivalent power
NIS	Normal metal-insulator-superconductor junction
PECVD	Plasma enhance chemical vapour deposition
PR	Photoresist
REM	Reflection electron microscope
RIBE	Reactive ion beam etching
RIE	Reactive ion etching
RPCVD	Reduced pressure chemical vapour deposition
SEM	Scanning electron microscope
SINIS	Back-to-back normal metal-insulator-superconductor junction
SOI	Silicon on insulator

S-Sm-S	Superconductor-semiconductor-superconductor junction
STEM	Scanning transmission microscope
STM	Scanning tunnelling microscope
TDD	The threading dislocation density
TEM	Transmission electron microscope
TES	Transition edge sensor
TES	Transition edge sensor
TMAH	Tetramethylammonium hydroxide
UHV	Ultra-high vacuum
UV	Ultraviolet light
VLSI	Very large scale integration
XRT	X-ray diffraction topography

List of Variables

Δ	Half-band energy gap
Σ	Electron-phonon coupling constant
ρ	Resistivity
μ	Mobility
τ	Relaxation time
Ω	Volume
G_{e-ph}	Electron-phonon thermal conductance
T_{bath}	Bath temperature
θ_D	Debye temperature
ω_D	Debye frequency
$\emptyset$	Total flux of particles
B	Magnetic field
c	Heat capacity
E	Electric field
E_F	Fermi energy
f	Fermi-Dirac distribution function of electron
I	Current
k_B	Boltzmann constant
l	Mean free path of electron
N	Carrier concentration
P	Power
q	Phonon wave vector
Q	Heat energy
R_H	Hall coefficient

R_S	Sheet resistance
R_T	Tunnel resistance
T_e	Electron temperature
T_{ph}	Phonon temperature
V	Voltage
v	Velocity
V_H	Hall voltage
K	Thermal conductivity
$g(E)$	Density of states

1 Introduction

1.1 Background to the research

1.1.1 The need for low temperature operation

It is well known that electronic devices and sensors can perform much more efficiently at low temperature than at room temperature. Low temperature operation can improve the performance of the electronic device and sensor instruments through improvement of the related properties of materials, such as electronic carrier mobility, thermal conductivity, and electrical conductivity. Reducing the temperature of operation also reduces the effect of thermal vibrations that shows up as noise in electronic systems. Since the noise level scales exponentially with temperature, even modest cooling can have a dramatic important in performance. The advantage for low temperature enhancement of complementary metal–oxide–semiconductor (CMOS) performance has been recognized[1]. For example, the switching time of semiconductor devices is faster; the circuit speed is increased because of the lower electrical resistance of interconnecting materials[2]; and the possibility of thermally induced failures of devices and components is reduced[3]. Moreover, low temperature cooling technologies are used to keep the operating temperatures of system below the functional temperature limit of the components.

1.1.2 Conventional cryogenics

At this time, the way to reach very low temperature (sub-Kelvin temperature) operating regions is through cryogenic technology and electronic cooling. Cryogenics is a study of the characteristics of materials at very low temperatures. This technique requires a cryostat, which is a device used to conserve low temperatures of samples or devices. In a typical installation, a cryostat first requires liquid helium to cool down the temperature of the system

to the boiling point of liquid helium which is 4 K at atmospheric pressure, but can be further lowered to around 1 K by reducing the pressure. After that, helium-3 was used as refrigerant to reduce temperature below 300 mK. Temperatures below 300 mK can be accessed by using a dilution refrigerator, which uses a mixture of helium-3 and helium-4 as the cryogenic medium to potentially reach temperatures of a few mK. However, such systems tend to be large, consume significant amounts of power and require helium-3 that is becoming a scarce and expensive resource[4]. An alternative cryogenic technique is adiabatic demagnetization that can reduce temperature down to the mK region[5]. A disadvantage of this technique is the difficulty of screening the cooled region from very high magnetic fields. Moreover, cooling is a single-shot operation with a limited operation time and needs time for recharging, which can lead to practical systems running pairs of adiabatic demagnetisation refrigerators in parallel with all the attendant increase in complexity, bulk and cost[4]. In recent years considerable advances have been made in using mechanical cooling systems, especially Gifford McMahon coolers, based on the controlled compression and expansion of helium gas, and pulse tube coolers that can reach below 2 K[6]. However, these systems generate a certain amount of vibration from moving parts and the continual expansion and contraction of the refrigerant gases can affect the cooled sample/sensor position.

1.1.3 Electronic cooling via tunnel junctions

This thesis will consider an alternative methodology of electronic cooling where the electrons in a material are used as the thermodynamic medium. In some applications these electrons are the active device and are the only part of a system that really need to be cooled; in other cases, cooled electrons in a device can be used to extract heat from another object. Electronic cooling has a number of advantages over the cryogenic approach: it requires lower power; only the investigated part is cooled; electronic cooling can operate for an unlimited

period and can be switched on/off rapidly. Furthermore, electronic cooling produces less wasted heat.

Electronic cooling can take place across a normal metal-insulator-superconductor (NIS) junction, where the insulator acts as a tunnel barrier for the electrons[7]. When a voltage bias V is applied across the junction such that the Fermi energy E_F in the metal is within the superconducting energy gap Δ (i.e. $0 < V < \Delta/e$) only hot electrons in the normal metal, with energies suitably higher than E_F , can tunnel to the superconductor. Each hot electron that tunnels removes energy from the normal metal, producing a cooling power corresponding to the energy loss in the normal metal. If there is only weak coupling between the electronic system and the phonons of the lattice then an electron temperature T_e can be defined that can be much lower than the lattice temperature T_{ph}. If electron-phonon coupling (section 2.3) is stronger, heat can be extracted from the lattice through the electron system leading to cooling of the whole object. With $V > \Delta/e$, cold electrons (from below E_F) in the normal metal can also tunnel to the superconductor, which results is a negative cooling power i.e. heating. The maximum cooling power occurs when the bias voltage closely approaches Δ/e[8]. This means that the electronic cooler can operate in the range of bias voltages that corresponds to the superconducting material and its energy gap. A significant development of NIS cooling is the usage of two NIS junctions (back-to-back as a SINIS structure) that leads to approximately twice the cooling power[9]. The electric current flows into the normal metal through one tunnel junction, as cold electrons to fill states below E_F, and out through the other, as hot electrons from states above E_F, while the heat current flows out of the normal metal through both tunnel junctions.

1.1.4 Semiconductor based cooler junctions

An alternative tunnelling cooler is the superconductor-semiconductor-superconductor (S-Sm-S) junction. The basic idea is to use a degenerate semiconductor to replace the normal metal with the natural Schottky barrier forming the required tunnel barrier without the necessity of an additional insulator[10]. The basic principles of NIS junctions are still valid in S-Sm-S junctions, but present some benefits when compared with NIS. Since the electron-phonon coupling strength is weaker in a semiconductor than in a normal metal, it can more easily reduce the heat flow between electrons and the lattice. Coupled with the fact that the density of free electrons is much lower in a semiconductor than in a metal, this means that the rate of heat transfer from the electronic system to reach a given base temperature can be less, or a lower electron temperature can be reached with the same cooling power. One downside of using a semiconductor is the higher resistivity than in the normal metals, which generates more Joule heating as a current flows and serves to limit the cooler performance. The semiconductor resistance, Schottky barrier height and electron-phonon coupling can all be adjusted to optimise the efficiency of a S-Sm-S junction, by changing the doping level and/or strain in the semiconductor as well as the superconductor material. In terms of general and well-known technology, heavily doped silicon could be the best choice as a degenerate semiconductor to replace the normal metal[10]. Another possibility, that is explored in this thesis, would be to use germanium which has a higher mobility for both electrons and holes than in silicon. An important part of this study will be to investigate the electron-phonon coupling in doped Ge that is a critical parameter for the operation of tunnel junction coolers.

Because the properties of germanium are similar to silicon, Ge can be relatively easily incorporated into the existing Si technology. Indeed, it can be said that Ge is already a key material for advanced technology. Ge is used in many applications such as infrared detector devices[11], spintronic devices[12], fiber optic[13], electronic devices[14] and solar cells[15]. As the

electronic mobility of Ge is superior to Si it may even replace Si as a channel material in fast transistors. In this thesis, Ge is investigated for low temperature applications.

1.1.5 Platform cooling

In addition to the principles of electronic cooling with tunnel junctions, explained above, for cooling an electronic device, the cooling of a platform is also important in cases where a separate electronic device is mounted on a platform. The platform can be cooled by using the electronic coolers to exact heat from the platform via a set of cold fingers that couple to phonons within the platform materials. The platform must also control the heat leak from the environment into the device being cooled, for which the platform requires a low thermal conductivity. Ideally, the platform would be totally isolated from its surroundings, but a practical solution is for the platform to be fabricated as a suspended structure, with support and thermal contact with the environment only through its edges, or better still, along narrow beams. The first step was demonstrated by the Aalto group[16], which used Si_3N_4 as an isolated membrane. Alternative membrane materials are porous Si or a crystalline Si wafer that is stronger than Si_3N_4. However, the crystalline membrane has more advantages than porous Si. For the same mechanical strength, the crystalline membrane could be thinner and less thermal massive than porous Si. To fabricate such a crystalline membrane, both Si and Ge have been considered. This thesis will concentrate on how Ge might be used to construct platforms for electronic cooling.

1.2 Objectives of this research

Germanium (Ge) is a challenging material to work with, and has been less studied than silicon. The principal requirement in fabricating a suspended Ge membrane structure is specific knowledge of the reactive ion etching (RIE) of Ge. This forms the first part of the investigation reported here. The reactive ion etching with SF_6-O_2 gas mixture, dry etching

process is selected to investigate the etching process of undoped and doped Ge. This work investigates the influence of O_2 content in gas mixture on etch rate and sidewall profile

The second part is the fabrication of various types of suspended Ge platform. The fabrication techniques achieve from the first part, etching process, to get the perfect anisotropic sidewall profile. The fabrication of various types of suspended Ge platform is demonstrated. As an example of how these can be useful, improvements in electrical properties (resistivity and mobility) are measured on some of these suspended structures.

Final part of this work is devoted to studying the strength of the electron phonon coupling in Ge, which is one of the important parameters for low temperature application such as bolometers that were fabricated by using the suspended platform.

1.3 Chapter summaries

- **Chapter 1:** The introduction of this thesis discusses the background, motivation and objectives of this thesis and also presents the outline of this thesis
- **Chapter 2:** The background theories required for an understanding of the work are reviewed in this chapter. The behaviour of phonons is explained with reference to the kinetic theory of gases and the Drude model, and used to discuss thermal conductivity. The various types of tunnelling junction employed for low temperature applications are described, including the electron-phonon interaction and the power law behaviour of heat transfer. Characteristics of the semiconductor material that affect its electrical and thermal properties are discussed and in particular the effect of dislocations.
- **Chapter 3:** This chapter explains the methodology of all the experiments and the associated analysis techniques applied to achieve the objectives of this thesis. Sample preparation by epitaxial growth and subsequent fabrication by photolithography and

etching is outlined. This chapter also explains how the etch rate was calculated and how scanning electron microscopy (SEM) was used to determine the side wall profile. Measurement of electrical properties via the Hall effect is outlined.

- **Chapter 4:** This chapter reports original research on reactive ion etching (RIE) of Ge by using an SF_6-O_2 gas mixture. It investigates the influence of O_2 content in the gas mixture on the etch rate and sidewall profile.
- **Chapter 5:** The fabrication of various types of suspended Ge platform such as suspended micro wires, spiderwebs and van der Pauw Greek-cross is demonstrated in this chapter. The electrical properties (resistivity and mobility) are measured using the Hall effect to show the influence of suspending the Ge layer.
- **Chapter 6:** This chapter reports the experimental measurement of electron phonon coupling in Ge, which is one of the important parameters for low temperature application such as bolometers that were fabricated by using the suspended platforms.
- **Chapter 7:** The conclusions and further work are discussed in this chapter.
- **Bibliography**
- **Appendix A** : Data of step height measurement
- **Appendix B** : Data of angle of sidewall profile measurement

2 Background Theory

This chapter will provide an introduction to some important concepts that are used in the thesis. A central issue of the work is how to cool part of a system. This requires heat to be extracted and then to flow elsewhere. First, it is necessary to know something about thermal conductivity since this determines how heat can flow through materials. Then the basic refrigeration device used to extract heat– the tunnel junction cooler – will be described. Heat leakage limits the minimum temperature that can be reached by an electron gas and this is determined largely by the electron-phonon coupling that will be discussed. Finally, dislocations in semiconductor crystals are mentioned as these imperfections in the crystal are an inevitable content of strained layers and have detrimental effects on electron transport through the material.

2.1 Germanium and application

Germanium is a group IV semiconductor, the same as Si. They have the same crystallographic structure (diamond) and they are face-centered cubic crystal structures. Germanium is a potentially important material to improve modern technology. Ge can be used as a dopant in fiber optic glasses and in semiconductor devices, both in activating conduction in layers and also as a substrate for epixtaxy. The mobility in germanium is higher than silicon for both electrons and holes, as shown in Table 2.1, because germanium has a lower transport mass for both electrons and holes[17]. As a result of the high hole mobility, a very fast Ge-based photodetector can be fabricated[18].

Carrier mobility (cm^2/Vs)	Germanium(Ge)	Silicon(Si)
Hole	1900	480
Electron	3900	1350

Table 2.1**:** Carrier mobility of germanium and silicon [From Ref. 19]

For low temperature applications, the germanium bolometer was developed in 1960 by Low[20]. It is the most widely used broadband detector at infrared wavelength $\lambda \leq 100$ μm[21]. As a result of its broad spectral response and high sensitivity, this has possible uses in astronomical observation and spectrometry. For example, the low temperature germanium bolometer developed by T. R. Lyle[22] is suitable to stimulate efforts toward perfecting a 1.2 mm radiometer for astronomical observations.

Ideally, a bolometer should have a low heat capacity, low thermal conductance, and its mechanical resonant frequencies should be higher than the operating frequency of the bolometer. The fabrication of a suspended platform is the main way in which thermal insulation is achieved in IR bolometers[23]. The suspended membranes used as platforms for bolometers are fabricated by knowledge of reactive ion etching of the membranes with a photoresist mask[24-28]. Many authors[29,30] commonly use a SiN suspended membrane of a thickness of about 1μm to be a platform for IR bolometers. However, a SiN suspended membrane can be quite fragile. An alternative structure to replace the SiN suspended membrane is a thick porous Si layer on a Si substrate, because of its better thermal isolation property and greater strength[31]. However, this porous Si platform will be more massive and consequently have a greater heat capacity unless the active area can be further isolated by nanostructuring.

Since the silicon nitride membrane is fragile and the amorphous materials are massive further alternatives should be considered. One option is provided by replacement with a

crystalline membrane. Compared with amorphous materials, a crystalline membrane will be thinner for the same mechanical strength, with lower thermal mass, and have a smoother surface, which could allow better integration of subsequent devices on the platform. In this thesis, the fabrication of a low thermal conductivity, crystalline platform from a Ge membrane has been investigated. At low temperature the conductivity of germanium follows a power law with temperature, having an exponent of 2.4 which is similar to 2.5 for silicon. This means that the thermal conductivity of the platform drops rapidly with decreasing temperature for regimes below 1 K.

2.2 Thermal conductivity

The transmission of heat energy through a solid is determined by its thermal conductivity. Heat can be transmitted via electrons, holes, lattice vibrations (phonons), electromagnetic waves and spin waves, so each of these processes contributes to the overall value of thermal conductivity as well as its variation with temperature. The thermal conductivity of solids also varies with the physical characteristic of materials, e.g. sample size for single crystals or grain size for polycrystalline materials, and in each case lattice defects, imperfections, or dislocations. In metals, the main contributors to heat flow are electrons and holes, whereas lattice waves (phonons) are the main heat carriers in non-metals. For semiconductors, studied in this work, both contributions are important.

In a solid, lattice waves also known as phonons are the quantized energy of the vibration of atoms about their equilibrium points. Every vibration can be represented as a phonon. Hence the large number of phonons that exists in the material. By assuming that these phonons are moving randomly, the lattice vibrations can be characterized by a phonon gas model that is analogous with the ideal gas model[32]. Thus, a simple way to understand the thermal conductivity of a solid should be to start from the kinetic theory of gases.

2.2.1 Kinetic theory of gases

An ideal gas is comprised of particles considered as perfect spheres or point masses. Each particle is very far apart. The distance between particles is many orders of magnitude compared with the diameter of the particles. The particles move randomly. Over time, each particle moves in many different directions and many different speeds. The motion of particles obeys Newton's Laws of motion. The collision between particles is elastic, i.e. particles do not lose energy when they collide.

Within the gas half the particles are travelling in the positive x-direction, so the flux of particles in the x-direction is $\emptyset = \frac{1}{2} n < |v_x| >$, where *n* is the concentration of particles and v_x is the velocity of particles in the positive x-direction and < > represents the average value[33]. In equilibrium there is a flux of equal magnitude in the opposite direction. The particles move from a region at temperature T + ΔT to a region at temperature T (and a similar flux moves in the negative x-direction from a region at T - ΔT to one at T). If a particle has heat capacity, *c* then the release of heat energy is $Q = - c\Delta T$.

In term of average time between collision τ

$$Q = - c(\frac{dT}{dx} v_x \tau) \quad . \tag{2.1}$$

The net flux of energy ($\vec{Q} = \emptyset \cdot Q$) is

$$\vec{Q} = -n v_x^2 c\tau \frac{dT}{dx} = -\frac{1}{3} C v l \frac{dT}{dx} \quad , \tag{2.2}$$

where $l \equiv v\tau$ and $C \equiv nc$

Thus the thermal conductivity (K) is $K = \frac{1}{3} C v l$. (2.3)

2.2.2 Drude model

The kinetic theory of gas considers that gas molecules move in straight lines with random motion. In metals, ion cores of atoms are immobile and valence electrons are loosely bound,

free electrons. The free electrons wander around the entire metal. A very high electron density (~ 10^{22} cm^{-3}) is present in metals. Therefore, Drude treats the dense electron gas in metal using the kinetic theory of gas. Below are the basic assumptions of Drude model.

1. Electrons move in straight line before collision, absence of an any electromagnetic field For the simplest case, the effect of electron-electron interaction, electron-ion interaction are completely ignored.

2. The only possible interaction is the instantaneous collision between a free electron and a lattice, which happens in an infinitesimal time.

3. τ is the mean free time between collisions. It is an independent of electron's position or velocity.

According to the Drude model, the thermal current density, $\overline{J_Q}$ is a vector that is parallel to the direction of heat flow with a magnitude equal to unit time that crosses a unit area perpendicular to the flow, $\overline{J_Q} = \frac{1}{3} l_e \bar{v} c_V (-\nabla T)$. In addition, the Fourier Law defines the thermal current density as $\overline{J_Q} = -\mathrm{K}_e \nabla T$, where K_e is the thermal conductivity of electron. Then, the thermal conductivity of electron is

$$\mathrm{K}_e = \frac{1}{3} l_e \bar{v} c_V \,, \tag{2.4}$$

where l_e is the mean free path of electron, $\bar{v}$ is the mean velocity of electron and c_V is the electronic specific heat per unit volume.

2.2.3 Lattice thermal conductivity

In non-metals e.g. insulators, the dominant thermal conductivity is lattice thermal conductivity(K_L). The vibrations that couple only neighbouring atoms can be characterized by normal mode, uniform oscillations at a given frequency or standing waves. The energy of atom vibration is a quantum referred to as a phonon. Each phonon has energy of $\hbar\omega$. The dispersion curves for acoustic and optical phonons of Ge are shown in Figure 2.1. At reduced

wave vector q =0, the transverse optical branches (TO) and longitudinal optical branches (LO) are degenerate[34].

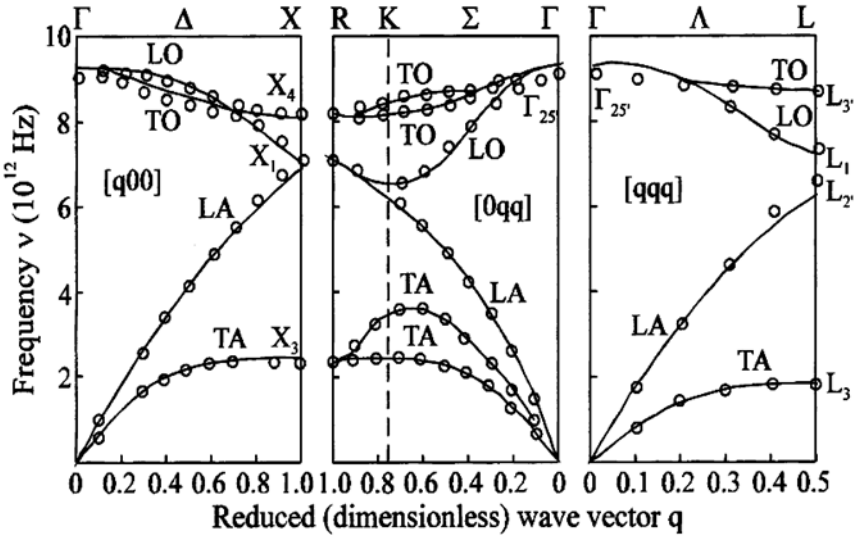

Figure 2.1: The phonon dispersion curves for Ge [From Ref. 35]

At low temperature, the acoustic phonons are normally the main heat conductors, as they have no minimum energy, while the optical phonons "freeze out" since there is insufficient thermal energy to excite these higher energy modes[36].

The phonon distribution function in equilibrium is $N_{\vec{q}}$

$$N_{\vec{q}} = 1/[\exp\left(\frac{\hbar\omega}{k_B T}\right) - 1] \ , \tag{2.5}$$

where ω is the frequency of oscillation

The heat flux of a phonon mode ($\bar{q}$) can be defined by the product of the average phonon energy and the group velocity(v_g). Hence the total heat flux of all phonon modes is

$$\vec{Q} = \sum_{\vec{q}} N_{\vec{q}} \bar{h}\omega_{\vec{q}} v_q \ . \tag{2.6}$$

$$K_L = -\frac{\vec{Q}}{\overrightarrow{\nabla T}} = \frac{1}{3}\sum_{\vec{q}} \bar{h}\omega_{\vec{q}} v_g^2 \tau_g \ \frac{\partial N_{\vec{q}}}{\partial T} \ . \tag{2.7}$$

The equation (2.7) can be solved easily by the assumption of Debye theory. The group velocity,v_g is replaced by the average velocity *v* that approximately equal to the velocity of

sound in solids. For all phonon branches, the frequency of vibration $\omega_{\bar{q}} = vq$, where q is the wave vector and the average velocity is the same for all polarizations.

$$K_L = \frac{k_B}{2\pi^2 v}\left(\frac{k_B}{\bar{h}}\right)^3 T^3 \int_0^{\theta_D/T} \tau_q(x) \frac{x^4 e^x}{(e^x-1)^2} dx \ , \tag{2.8}$$

where $x = \bar{h}\omega/k_B T$, the Debye temperature $\theta_D = \frac{\bar{h}\omega_D}{k_B}$ where $\omega_D$is Debye frequency that corresponds to equation (2.5), $N_{\vec{q}}$ the total number of all distinguishable phonon modes and $\tau_q(x)$ are the phonon scattering relaxation time.

$$3N = \int_0^{\omega_D} \frac{3\omega^2}{2\pi^2 v^3} d\omega \ . \tag{2.9}$$

From Debye approximation the lattice heat capacity is

$$C(x)dx = \frac{3k_B}{2\pi^2 v^3}\left(\frac{k_B}{\bar{h}}\right)^3 T^3 \frac{x^4 e^x}{(e^x-1)^2} dx \ . \tag{2.10}$$

Then equation (2.8) can be rewritten in term of the lattice heat capacity

$$K_L = \frac{1}{3}\int_0^{\theta_D/T} C(x) v l(x) dx \ , \tag{2.11}$$

where $l(x) = v\tau_q$ is the mean free path of a phonon.

It can be seen that the equation (2.11) is analogous to equation (2.4). If the relaxation times $\tau_i(x)$ for various phonon scattering process in solids can be calculated, the phonon scattering relaxation time $\tau_q(x)$ can be changed to

$$\tau_q^{-1}(x) = \sum_i \tau_i^{-1}(x) \ . \tag{2.12}$$

For phonon-phonon Umklapp scattering, this scattering generates a phonon with momentum k-vector outside the first Brillouin zone.

$$\tau_U^{-1} \approx \frac{\bar{h}\gamma^2}{Mv^2\theta_D}\omega^2 T exp\left(\frac{-\theta_D}{3T}\right) \ , \tag{2.13}$$

where *M* is average atomic mass in the crystal and γ is the Grüneisen constant

For phonon-boundary scattering, the scattering does not depend on phonon frequency and temperature.

$$\tau_B^{-1} = \frac{v}{d} \quad , \tag{2.14}$$

where d is the size of a single crystal or the grain size of in polycrystalline material.

For the phonon point-defect scattering, the linear dimensions of the defects are smaller than the phonon wavelength.

$$\tau_{PD}^{-1} = \frac{V}{4\pi v^3}\omega^4 \sum_i f_i \left(\frac{\bar{m}-m_i}{\bar{m}}\right)^2 \quad . \tag{2.15}$$

For the isotropic scattering proposed by Klemens[37] , the scattering results of point imperfections.

$$\tau_I^{-1}(\omega) = \frac{3V_0\Gamma\omega^4}{\pi v^3} \quad , \tag{2.16}$$

where V_0 is average volume per atom in crystal, and Γ is point impurity scattering parameter[38].

To understand the lattice thermal conductivity, the work of Rosenberg[39] and Glassbrenner and Slack[40] were considered. Rosenberg[39] has investigated the thermal conductivity of a single germanium and a polycrystalline silicon in the range 2 K to 100K as shown in Figure 2.2. They tends are similar but the thermal conductivity of germanium is higher than silicon. At low temperature, the thermal conductivity of Ge and Si are linear on a log-log plot which indicates that they are proportional to a power of T. These powers are 2.4 and 2.5 for Ge and Si respectively.

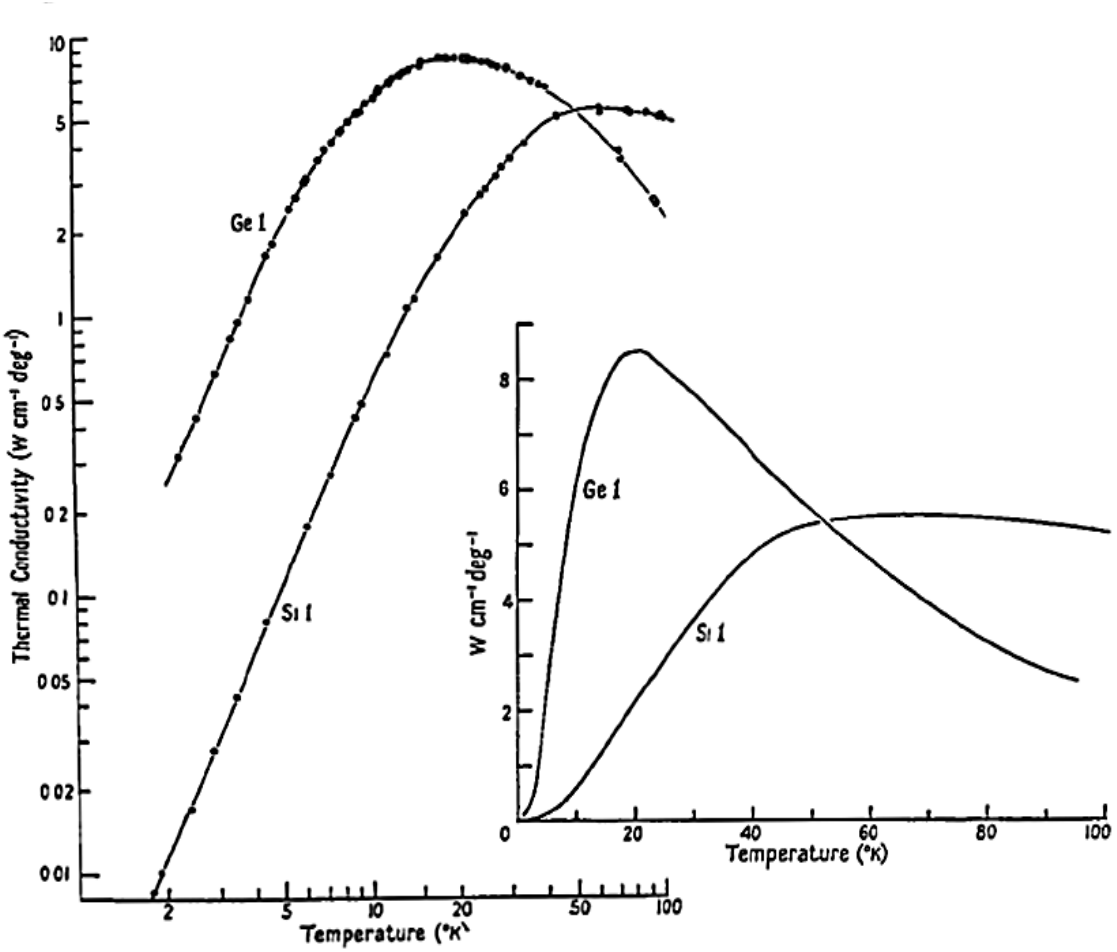

Figure 2.2: The thermal conductivity of germanium (Ge_1) and silicon (Si_1) as a function of temperature on a logarithmic scale. The inset shows the same curve plotted on a linear scale. [From Ref. 39]

Another interesting work was presented by Glassbrenner and Slack[40]. They investigated the thermal conductivity of Si and Ge from 3 K to 1190 K, Figure 2.3. The results show that phonons are the dominant carriers of heat in Si and Ge at temperature from 3K to their melting point. At low temperatures, the lattice thermal conductance of Si and Ge rise when temperature increases due to the increase in carrier density with temperature. On further increasing temperature the lattice thermal conductance of Si and Ge decreases, which is due to the increased amount of phonon scattering.

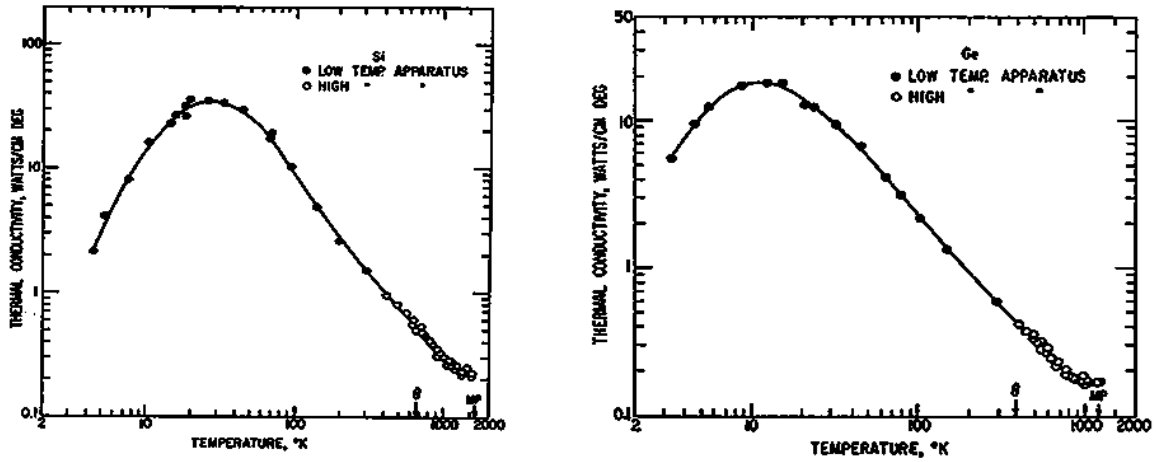

Figure 2.3: The lattice thermal conductivity of Si and Ge versus temperature, (a) The lattice thermal conductivity of Si as a function of temperature (b) The lattice thermal conductivity of Ge as a function of temperature. [From Ref. 40]

To understand the characteristic of the lattice thermal conductivity, the results of Si were compared with theoretical fit which the possible mechanism of phonon scattering as shown in Figure 2.4. It can conclude that the characteristic of the phonon thermal conductivity is the combination of the relaxation times for Umklapp, diffuse, boundary and isotope scattering. In addition, the essential conclusion of Glassbrenner and Slack[40] is that phonons are the dominant carriers of the thermal energy at temperature from 3 K to their melting point. The electronic thermal conductivity contributes to the total thermal conductivity of Ge at 700 K and Si at 1000 K.

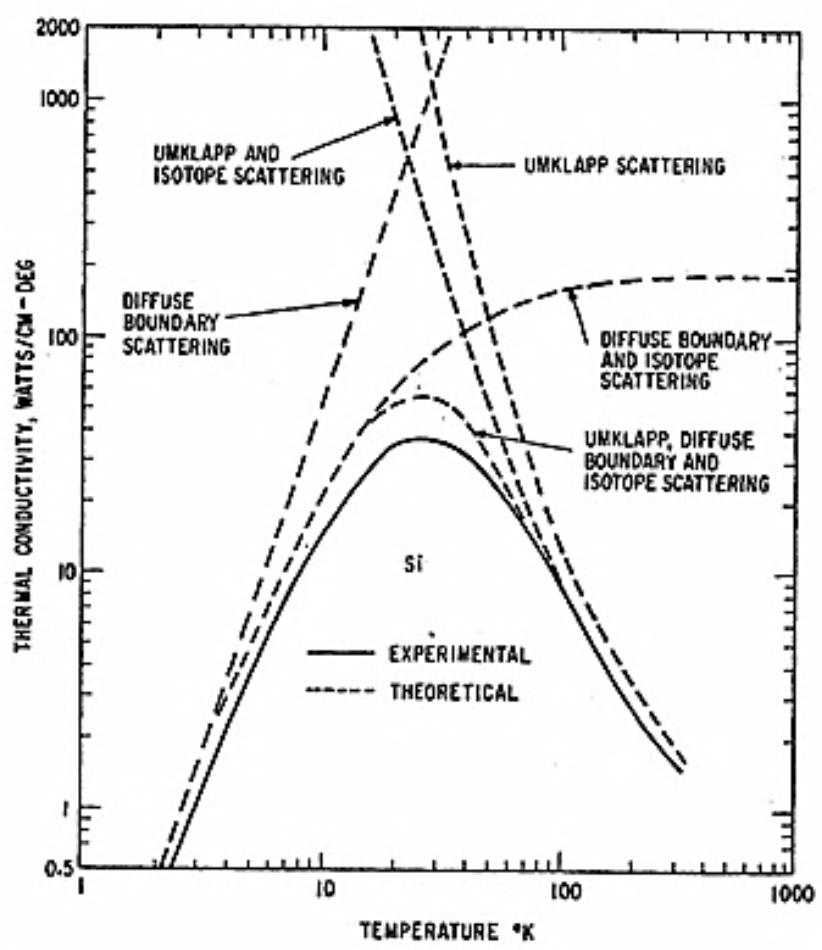

Figure 2.4: The comparison of the lattice thermal conductivity of Si with theory in which various phonon scattering mechanism. [From Ref. 40]

2.2.4 Phonon dimensionality

As a result of advances in fabrication techniques, thin suspended structures can be produced in which it is expected that phonons can move freely only within the plane of a membrane (2D system), instead of travelling freely within fully bulk materials (3D system). In this case, the bulk transversal and longitudinal phonon modes couple to each other and transform to new eigenmodes. The new eigenmodes are the horizontal shear modes (*h*), symmetric (*s*) Lamb modes and anti-symmetric (*a*) Lamb modes. The branches of the dispersion relation are shown in Figure 2.5. The three lowest branches in the long wavelength

limit are shown in Figure 2.6. The three lowest branches are dominant for thin membranes at low temperature[41]. Their low frequency analytical expressions are $\omega_h = c_t k_{//}$ for *h*-modes, $\omega_s = c_s k_{//}$ for *s*-modes and $\omega_a = \frac{\bar{h}}{2m} k_{//}^2$ for *a* modes where $k_{//}$ is the wave vector component parallel to the membrane surface, c_t and c_l are transversal and longitudinal sound velocities respectively, $c_s = 2c_t \sqrt{\frac{(c_l^2 - c_t^2)}{c_l^2}}$ is the effective sound velocity of *s*-modes and $m = \bar{h}\left[2c_t d\sqrt{\frac{(c_l^2 - c_t^2)}{3c_t^2}}\right]^{-1}$ is the effective mass for *a*- modes.

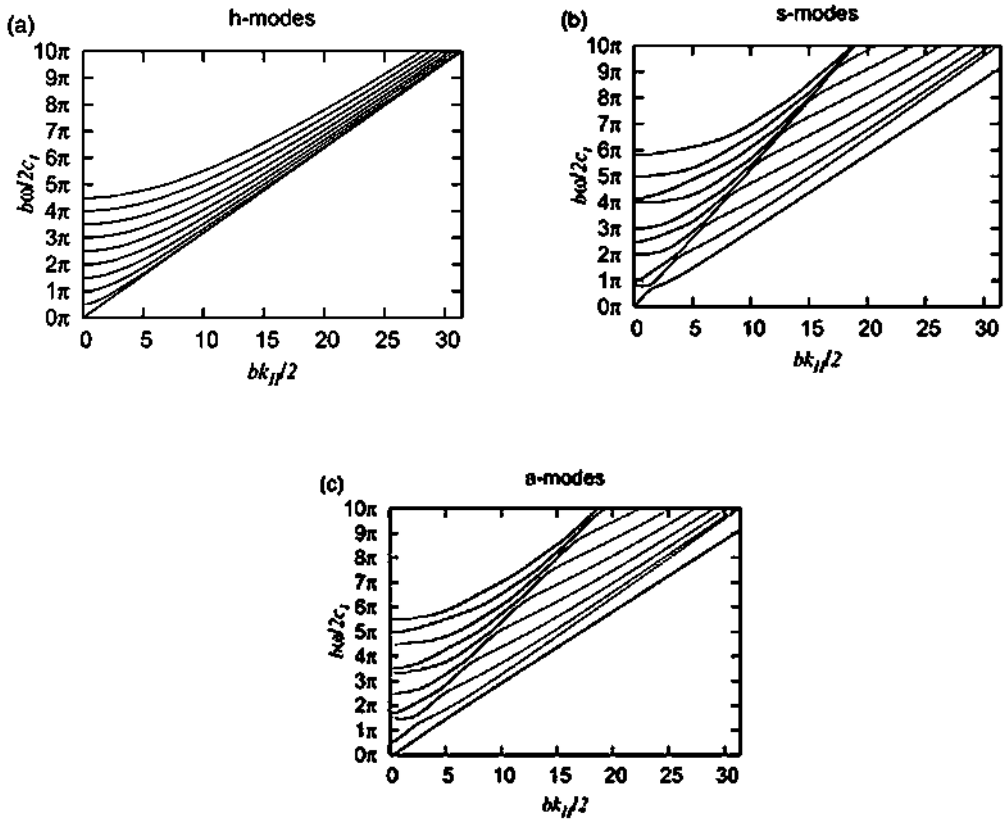

Figure 2.5: The branches of dispersion relations of phonon eigenmodes (a) *h*-modes (b) *s*-modes (c) *a*-modes [From Ref. 42]

Greater thermal insulation of a membrane from its surroundings can be achieved by cutting the membrane to be a bridge form[42] as shown in Figure 2.7. Calculation of the thermal conductivity (κ) of a bridge form assumes diffusion of phonons at the bridge edges. If the width of the bridge decreases below a certain value (depending on the mean free path of phonons in the uncut membrane) the interaction with the edges becomes the main scattering process for the phonons. At low temperatures it is found that $\kappa \propto T^{3/2}$ for the bridge, whereas $\kappa \propto T^2$ for the full membrane, as shown in Figure 2.8.

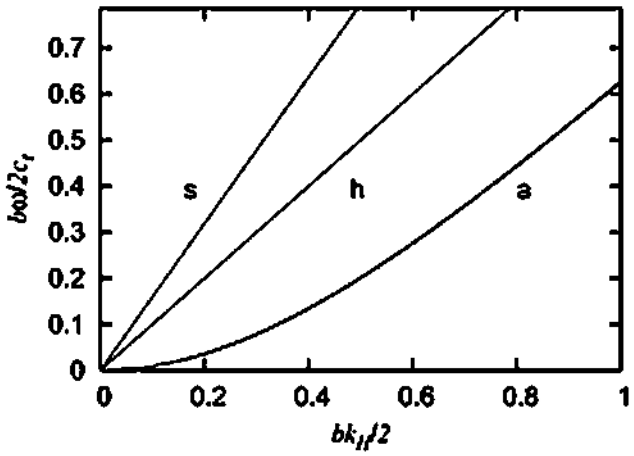

Figure 2.6: The three lowest branches in the long wavelength limit [From Ref. 42]

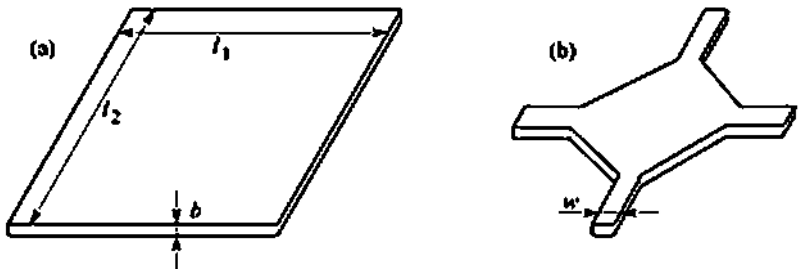

Figure 2.7: (a) The full membrane, l_1 xl_2 μm^2 (b) the bridge form, *w* width, cutting from (a) [From Ref. 43]

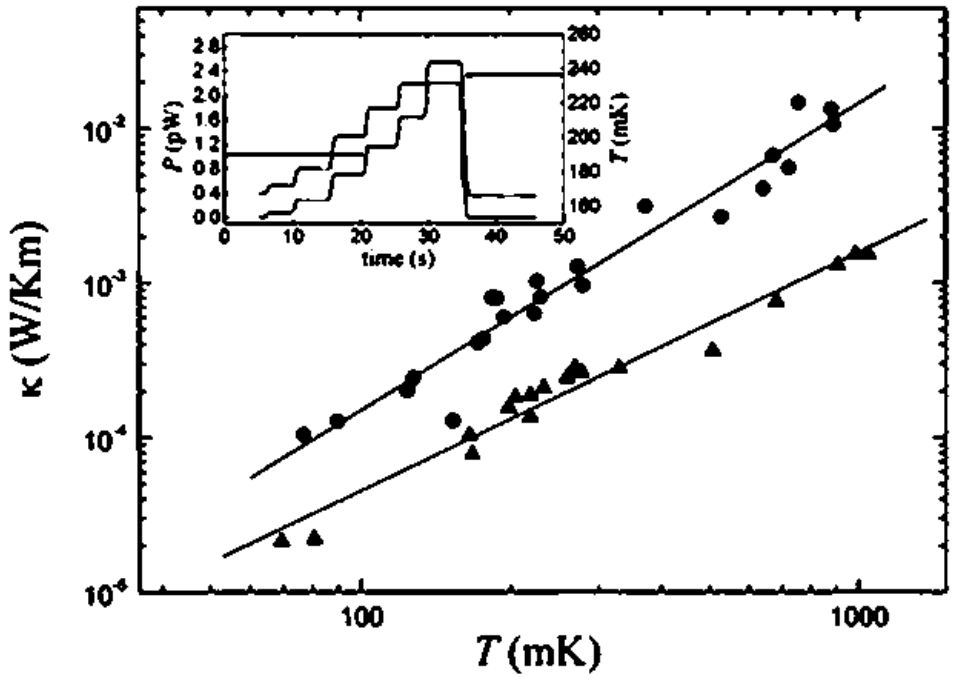

Figure 2.8: Thermal conductivity of silicon nitride, full membrane (circles) $\kappa \propto T^2$, bridge form(triangles) $\kappa \propto T^{3/2}$. Inset represents a typical dc measurement in the bridge [From Ref. 43]

2.3 Tunnel junction coolers

The tunnel junction is a potential barrier between two electrically conducting materials such as a normal metal, semiconductor and superconductor. Quasiparticles such as electrons can pass through the barrier by the quantum mechanical tunnelling process[44]. In classical physics, the probability of quasiparticles that can pass through the barrier is zero (although with sufficient energy they can go over the barrier). On the other hand, the quasiparticles have some probability for passing through the barrier according to quantum mechanics, with a tunnelling probability dependant on the height (energy) and width (physical) of the barrier.

Tunnel junctions were first recognized in the 1990s[45] . The tunnel junction uses an energy selective tunnel barrier to extract high energy (hot) electron. As a refrigerator, the cooling power of a tunnel junction is typically low, just in order of pW. However, if the volume to be cooled is small and the heat load (that is usually heat from the lattice) is sufficiently low, for example at mK temperatures, a tunnel junction is able to cool the electron temperature from an initial bath temperature about 300 mK to 100 mK and below[46].

2.3.1 The normal-insulator-superconductor (NIS) tunnel junction

The normal-insulator-superconductor (NIS) tunnel junction consists of a normal metal, a thin layer of insulator and superconductor, as shown in Figure 2.9.

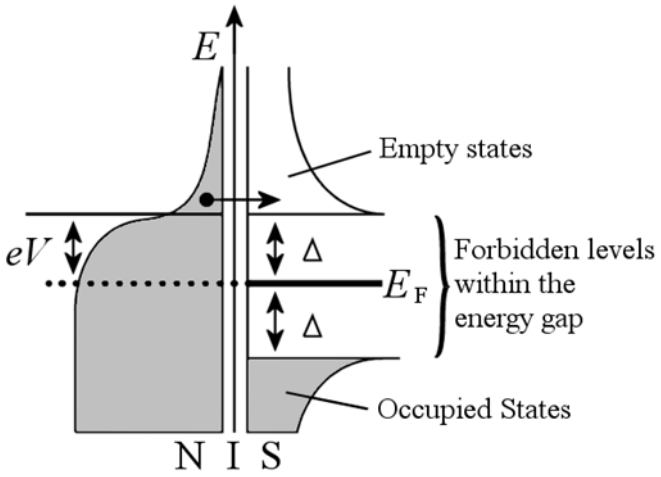

Figure 2.9: The energy diagram of the normal-insulator-superconductor(NIS) tunnel junction, Δ is a half-band gap and V is a bias voltage. [From Ref.47]

In NIS tunnel junctions under certain bias voltages $V \leq \Delta/e$, the flow of electric current carried by electrons is accompanied by a heat transfer from the normal metal into the superconductor[45,48]. The superconducting energy gap Δ induces selective tunnelling of high energy (hot) electrons out of the normal metal as only those electrons with energy E higher than Δ (compared to the Fermi level) can tunnel out of the normal metal[49]. It means that the

single particle current and associated heat current are generated. Colder electrons with lower energies $E < \Delta$ are blocked by the energy gap of the superconductor since they have no final states to tunnel into. Each electron removes energy equal to $(E - eV)$ from the metal corresponding to a cooling power of order $I\, k_B T/e$ where I is the current through the junction. The maximum cooling power occurs for voltages closely near $V = \Delta/e$[30]. If the bias voltage $V > \Delta/e$, the Fermi energy of the normal metal is above the edge of superconductor gap and cold electrons can also be extracted from the normal metal. This condition removes the cooling effect of selectively extracting only hot electrons and even leads to heating due to passing a current through the resistive metal.

The current of high energy electrons that leave the normal metal is given by equation (2.16).

$$I = \frac{1}{eR_T}\int_{-\infty}^{\infty} F(V, T_e, T_b)\, g(E)\, dE\ , \tag{2.16}$$

where $F(V, T_e, T_b) = f(E - eV, T_e) - f(E, T_b)$ and $f(E, T) = 1\Big/\left[1 + exp\left(\frac{E}{k_b T}\right)\right]$.

R_T is the normal state tunneling resistance, f is the Fermi-Dirac distribution function, T_e is the electron temperature in the normal metal and T_b is the temperature of the superconductor assumed to be equal to the thermal bath temperature, $g(E)$ is the density of states within the superconductor[50].

$$g(E) = \begin{cases} 0 & when\ |E| < \Delta \\ \frac{|E|}{\sqrt{E^2 - \Delta^2}} & otherewise \end{cases}\ . \tag{2.17}$$

This current removes energy at a rate of cooling power, P_{cool}

$$P_{cool} = \frac{1}{e^2 R_T}\int_{-\infty}^{\infty} (E - eV) F(V, T_e, T_b)\, g(E)\, dE\ . \tag{2.18}$$

The cooling power P_{cool} is positive (positive cooling power) for $eV < \Delta$. It means that heat transfers to the superconductor and the normal metal is cooled. On the other hand, when

P_{cool} is negative (negative cooling power) for $eV > \Delta$, the current increases rapidly which heats the normal metal.

Electron-phonon coupling provides a heat transfer from the phonons of the lattice to the electrons and is given by[51]

$$P_{e-ph} = \Sigma\Omega\left(T_e^n - T_{ph}^n\right) \ , \tag{2.19}$$

where Σ is the electron-phonon coupling constant, Ω is the volume of the sample, and T_{ph} is phonon temperature, which will usually be the same as the bath temperature T_b. The power n depends on the material: usually n=5 for a pure metal according to theoretical[52] and experimental[53] evidence.

In the simplest case, the heat balance can be used to calculate the temperature to which the electrons are cooled by the solution of equation 2.20[54]

$$P_{cool} + P_{e-ph} = 0 \quad . \tag{2.20}$$

The NIS junction can also be used to measure the temperature. Equation (2.16) shows that the current crossing the junction depends on the electron temperature of the normal metal. At low temperature ($k_BT << \Delta$) and voltages ($0 < V < \Delta/e$), the current can be reduced to

$$I(V,T) \approx I_0 e^{\frac{eV-\Delta}{k_B T_{e,N}}} \quad , \tag{2.21}$$

where $I_0 = \frac{\Delta}{eR_T\sqrt{\frac{\pi k_B T_{e,N}}{2\Delta}}}$.

Obviously, the I-V characteristic of a NIS junction (Figure 2.10) relies strongly on the electron temperature of the normal metal. This characteristic allows a NIS to be used as a thermometer. The low temperature current is nearly zero when $V < \Delta/e$ where the tunneling cannot occur. For $V \sim \Delta/e$, the current increases sharply. Therefore the cooling power is a maximum at $V \sim \Delta/e$.

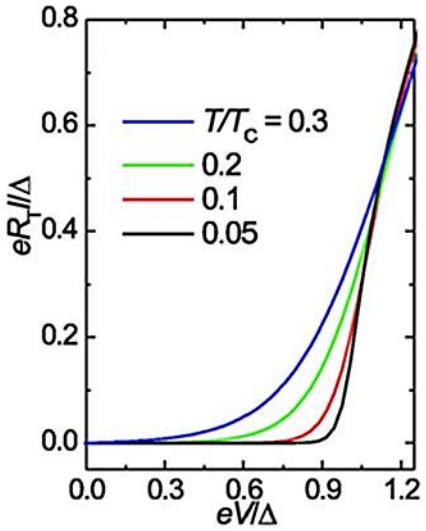

Figure 2.10: The I-V characteristic of NIS thermometer at various relative temperature T/T_c where T_c the transition temperature. [From Ref. 55]

Nahum *et al.*[56] fabricated the first NIS tunnel junction. A single NIS tunnel junction was used in order to cool a small normal metal strip. Later Leivo *et al.*[57] showed that the cooling power of an NIS junction is an function of the applied voltage. Moreover, they have fabricated a refrigerator with a double junction (SINIS), which offers a reduction of the electronic temperature from 300 mK to about 100 mK. This significant temperature reduction shows that NIS junctions have the possibility of being used for on-chip cooling of nano-sized systems like high-sensitivity detectors and quantum devices[58].

2.3.2 The double junction SINIS structure

The cooling power of a NIS device can be doubled by using two NIS junctions back-to-back, so-called double junction SINIS, as shown in Figure 2.11, with the I-V characteristic of a SINIS junction shown in Figure 2.12.

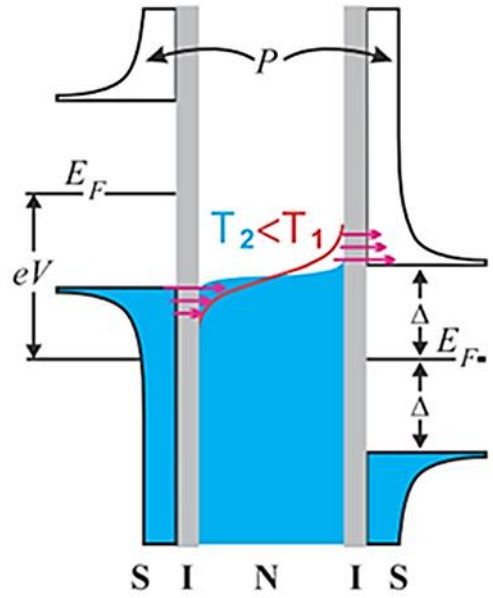

Figure 2.11: Energy diagram of SINIS junction. [From Ref. 59]

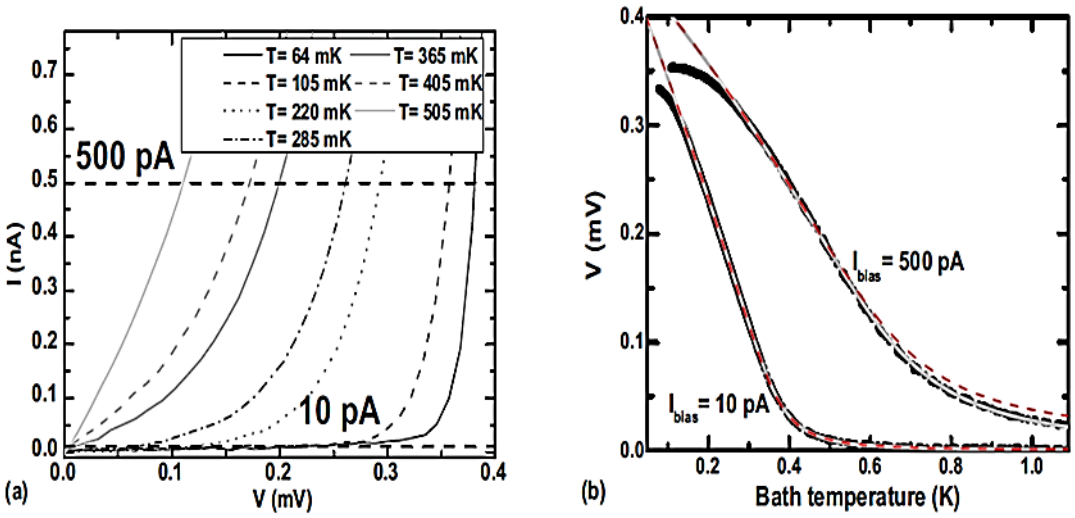

Figure 2.12: (a) The I-V characteristic of SINIS thermometer. The horizontal dashed lines are the constant current bias I= 500pA and I=10pA. (b) The two black circles are the calibration curves of SINIS thermometer, BCS theory with Δ(T): grey line, BCS theory with Δ(0): red dashed line. [From Ref. 60]

The bias potential V is divided evenly between the 2 junctions, which have equal tunnel resistance R_T . Hot electrons above the Fermi level can tunnel out from the normal metal and only cold electrons below the Fermi level can tunnel into the normal metal, electrons enter at the left hand junction. Then electric current flows from right to left. In case of both junctions are assumed that the two tunnel resistance are equal, a factor of two can be included in equations of cooling power

$$P_{cool} = \frac{2}{e^2 R_T}\int_{-\infty}^{\infty}(E - eV)F(V, T_e, T_b)g(E)dE \ , \qquad (2.22)$$

where R_T is the normal state tunnel resistance of a single NIS junction.

2.3.3 The superconductor-semiconductor-superconductor (S-Sm-S) tunnel junction

Savin *et al.*[61] replaced the normal metal with a degenerate semiconductor (Sm), in the arrangement shown in Figure 2.13.

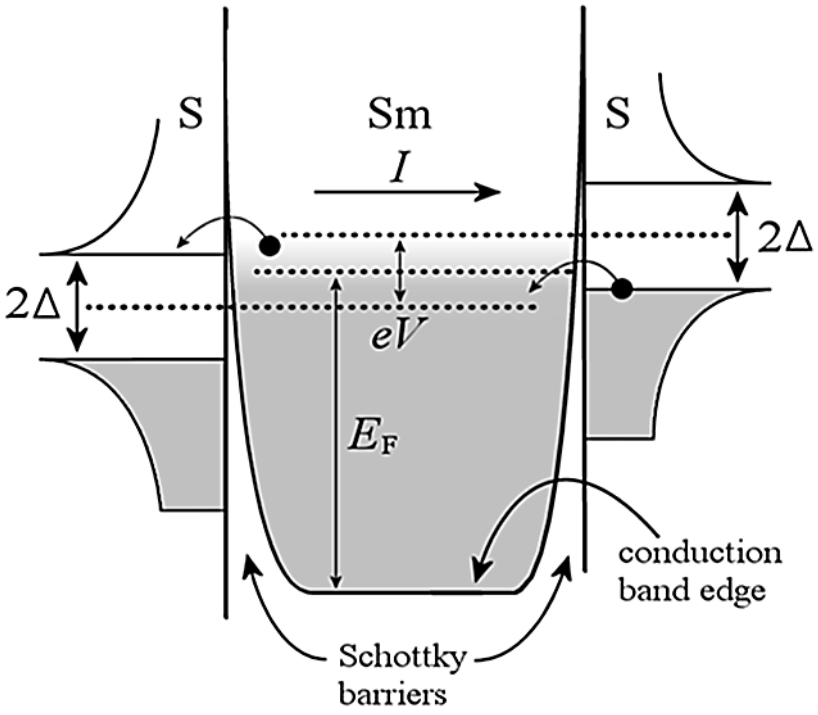

Figure 2.13: The energy diagram of the superconductor-semiconductor-superconductor (S-Sm-S) tunnel junction, Δ is a half-band gap and V is a bias voltage. [From Ref. 62]

The advantage of this junction over the NIS structure is that the oxide barriers are eliminated, which is desirable because oxide barriers are difficult to form and prone to the formation of pinholes in the thinner oxides. Moreover, the electron-phonon interaction in semiconductors is weak compared with normal metals. This means that the electrons can easily heat, or cool, in thermal isolation from the phonons.

The cooling process occurs when a small bias voltage $V < 2\Delta /e$ is applied across the structure. The hot electrons in the thermal tail of the Fermi distribution can tunnel from the semiconductor through the left Schottky junction to the superconductor. In contrast, the cold electrons that have an energy below the energy gap in the right superconductor can tunnel to the semiconductor. Thus, electrons are removed from above and added below the Fermi level in the semiconductor. This reduces the total energy of the electron gas and leads to a cooling effect. The maximum cooling power for a S–Sm–S cooler with two symmetric junctions is given by[63,64]

$$P_{max} \approx 2\left[0.6\frac{\sqrt{\Delta}}{e^2 R_T}(k_B T_e)^{3/2}\right], \tag{2.23}$$

where R_T is the tunnelling resistance for a single junction and T_e is the electron temperature in semiconductor. The maximum cooling power is obtained when bias voltage is slightly below Δ/e.

To first order, the current transport in S-Sm-S tunnel junction is given by[65]

$$I = \frac{\sqrt{2\pi\Delta k_B T}}{2eR_T}\exp\left(\frac{eV-\Delta}{k_B T}\right) \tag{2.24}$$

From equation (2.24), the S-Sm-S tunnel junction can be used as a thermometer by using a constant bias current. The I-V characteristic of the tunnelling junction is displayed in Figure 2.14.

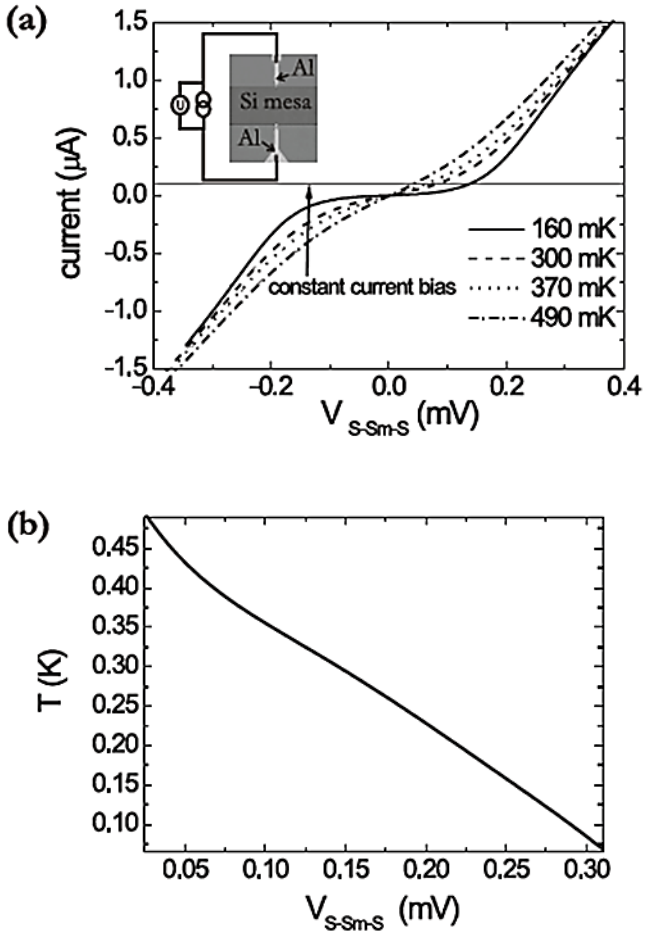

Figure 2.14: (a) The I-V characteristics of the superconductor-semiconductor-superconductor(S-Sm-S) tunnel junction at different temperatures. (b) The temperature calibration curve. [From Ref. 66]

As a result of the high resistance compared with NIS tunnel junctions, the power extraction is limited. Higher dopant densities in Si can reduce the tunnel resistance[67]. Unfortunately, when the tunnel resistance was reduced an additional heating mechanism appeared. The additional heating was most dominant at low temperature and low applied bias. This heating was modeled as an additional leakage path through the tunnel junction[67]

and subsequently attributed to back tunnelling of quasiparticles (electrons) and phonons from the superconductor[68].

2.4 Electron-Phonon coupling

Electron-phonon (e-ph) coupling is the dominant mechanism for electron energy relaxation at low temperatures (below 1 K). The e-ph coupling is a weak interaction and this can lead to a situation, in which electrons and phonon are at significantly different temperatures. At low enough temperatures, power applied to the electron system can elevate the electron temperature (T_e) significantly above the phonon temperature (T_p), so-called hot electron effects[69]. The strength of e-ph coupling depends on the material. The e-ph coupling can be divided into two cases depending on the parameter ql. where q is the wave vector of the dominant thermal phonon and l is the mean free path of electrons. The first case is the clean limit when $ql >> 1$. In this case, it has only electron-phonon interaction mechanism. The second case is dirty limit when $ql << 1$. In this case, electrons also scatter from impurities such as defects and boundaries.

In general, the electron-phonon scattering rate between electrons and phonons strongly relies on temperature as[70]

$$\tau_{e-p}^{-1} = \alpha T^m \quad . \tag{2.25}$$

and thus the corresponding net power flow between hot electrons at temperature T_e to phonons at temperature T_p is

$$P = \Sigma\Omega\left(T_e^n + T_p^n\right) \ , \tag{2.26}$$

where Σ is the e-ph coupling constant which depends on material, Ω is the volume where the e-ph interaction takes place and $n = m+2$.

The value of m depends on the dimensionality of the phonon system and the electron gas as well as the type and density of impurities within the material[70]. For ordered metals in the

clean limit *ql* >> 1 at low temperature, the assumption that the electrons scatter only from longitudinal phonons gives *n* =5 or *m* = 3[69,71] . If both longitudinal and transverse phonon modes interact with electrons, the e-ph scattering rate is

$$\tau_{e-p}^{-1} = \frac{3\pi^2\beta_t T^2}{(p_F u_t)}\frac{\tau}{\tilde{\tau}} + \frac{7\pi\varsigma(3)\beta_l T^3}{2(p_F u_l)^2} \quad , \qquad (2.27)$$

where u_t and u_l are the transverse and longitudinal sound velocities, $\beta_t = \beta_l\left(\frac{u_l}{u_t}\right)^2 = \left(\frac{2\epsilon_F}{3}\right)^2 \frac{mp_F}{2\pi^2\rho u_t^2}$ where ϵ_F is Fermi energy, p_F is Fermi momentum and ρ is mass density, $\tau = \frac{l}{v_F}$ can be determined by electron scattering from impurities and the static potential, and $\tilde{\tau} = \frac{\tilde{l}}{v_F}$ is the electron momentum relaxation rate correspond to scattering from impurities[51]. From equation (2.27) if the transverse modes are dominant, the exponent of temperature dependence is *m* =2 and $\Sigma \propto \frac{1}{l}$. On the other hand, if the intensities of both modes are equal, it is more complex. The temperature dependence *m* can vary from 2-3 and the coupling constant $\Sigma \propto \frac{1}{l} - l^0$.

In the dirty limit *ql* << 1, the processes include scattering from impurities, defects and boundaries. The e-ph interaction can be explained via interference process between electron-phonon and electron-impurity scattering. From the model of Sergeev *et al.*[72] in which the scattering can happen either from vibrating or static impurities the scattering rate is

$$\frac{1}{\tau_{e-p}} = \frac{\pi^4 T^4}{5\hbar^2}(p_F l)\left(\frac{\beta_l}{(p_F u_l)^3} + \frac{3\beta_t}{2(p_F u_l)^3}\frac{\tau}{\tilde{\tau}}\right) + \frac{3\pi^2 T^2}{2p_F l}\left(1 - \frac{\tau}{\tilde{\tau}}\right)\left(\frac{\beta}{p_F u_l} + \frac{2\beta_t}{p_F u_l}\frac{\tau}{\tilde{\tau}}\right). \quad (2.28)$$

In the case of fully vibrating impurities i.e. they are fully moving with phonon mode ($\frac{\tau}{\tilde{\tau}} = 1$), the temperature dependence *m* is equal to 4 and $\Sigma \propto l$. In the static scattering potential, ($\frac{\tau}{\tilde{\tau}} = 0$) only longitudinal phonons contribute. In this case *m* is equal to 2 and $\Sigma \propto \frac{1}{l}$ at low

temperature. Between these two case, both scattering processes affect the rate and the exponent of temperature dependence can vary between m = 2 - 4 and $\Sigma \propto \frac{1}{l} - l$.

In many-valley semiconductors, for example Si is six-fold degenerate as shown in Figure 2.15, the intervalley scattering is a more significant process than the intravalley scattering in relaxing the momentum and energy of the conducting electrons[73]. The electron-phonon interaction can be considered to be caused by deformation potential coupling when the intervalley processes are taken into account. In the many-valley semiconductors acoustic waves are strongly attenuated when the strain associated with them destroys the equivalence of the valleys[74] as shown in Figure 2.15. Strain can lift the valley degeneracy in the conduction band which leads to the electron-phonon coupling decreasing by Mean-field theory[75].

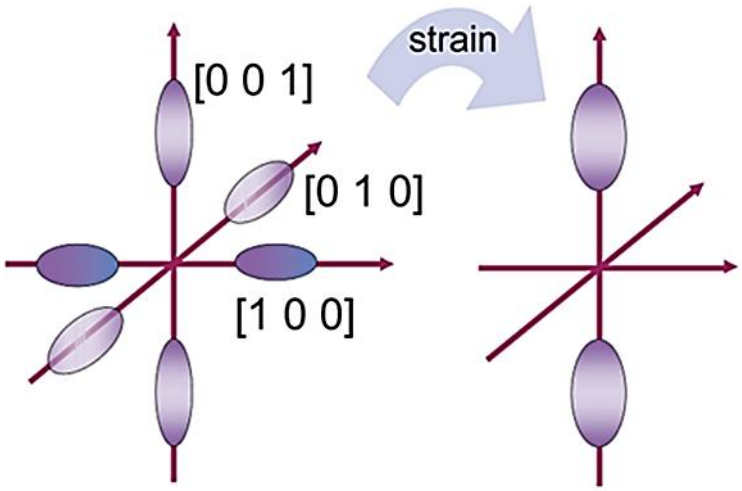

Figure 2.15: Schematic illustration of the Si intervalley, six-fold degenerate [From Ref. 76]

Equation 2.29 presents the heat flow from electrons to phonons[77]

$$P = -\sum_{\lambda} \int d\vec{q} \, \frac{1}{(2\pi)^2} \hbar\omega_{q\lambda} \frac{\partial N\left(\hbar\omega_{\vec{q}\lambda}\right)}{\partial t} \quad , \tag{2.29}$$

where $N\left(\hbar\omega_{\vec{q}\lambda}\right)$ is the phonon energy distribution function, $\hbar\omega_{\vec{q}\lambda}$ is the phonon energy, $\vec{q}$ is the phonon wave vector, *d* is the dimensionality of the phonons and λ includes all the possible phonon modes[78]. The magnitude of $\vec{q}$ depends on the direction, but after integration over this directional dependence the result is a scalar constant. For approximation[79,80], the heat flow between electron and phonon, *P* is written as

$$P = \Sigma\Omega\left(T_e^{\nu+4} - T_{ph}^{\nu+4}\right) . \tag{2.30}$$

$\Sigma \propto \tau_{iv} N^{1/3}$, where τ_{iv} is the intervalley scattering relaxation time and *N* is the carrier concentration.

For the clean limit defined as $ql >> 1$, the temperature dependence for electron-phonon interaction follows the power law T^5 [81,82]. The previous was done by Roukes *et al.(*1985)[82] and Wellstood *et al.*(1994)[83] found that $\tau_{e-ph}^{-1} \alpha T^3$ or $P \alpha T^5$ for Cu. In addition, Echternach *et al.*(1993)[65] reported the same results for Au.

For disordered metals in the dirty limit when $ql << 1$, the temperature dependence for electron-phonon interaction follows the power law T^6 [81,82]. Gershenson *et al.*[84] examined the electron-phonon relaxation in ultrathin disordered metal films, of Hf and Ti. The power flow is $P \alpha T^6$ which means that that electron-phonon relaxation rate follows $\tau_{e-ph}^{-1} \alpha T^4$. Karvonen *et al.*[85] studied the electron phonon interaction of thin Cu and Au films. The research showed that the electron phonon scattering rate followed a T^4 temperature dependence, or the power flow followed a T^6 temperature dependence in both materials. However, Echternach *et al.*[86] investigated the electron phonon scattering rates in disordered metallic films, Au and Bi. They reported the power flow rate is proportional to T^5. Karvonen

and Maasilta[87] used the hot electron technique to measure the electron phonon coupling in a Cu wire. The experiment show that n = 4.5 for a wire thickness equal to 30 nm and n = 5 for wire thickness more than 30 nm. It indicates that n should be size dependent.

For semiconductor in the dirty limit when $ql \ll 1$, the theoretical prediction indicate that power flow between electron and phonon has a T^6 dependence[71]. Kivinen *et al.*[70] investigate the electron-phonon interaction in thin, heavily n-type, phosphorous doped silicon-on-insulator (SOI). They found that the temperature dependence of the heat flow followed a T^6 dependence according to the theory of 3D phonon[71]. However, Prunil *et al.*[66] studied the electron-phonon coupling in a degenerate n type silicon-on-insulator (SOI) film. They found that the energy transfer from hot electron to phonon, power flow is proportion to T^5 according to the theory of 2D phonon[66].

2.5 Dislocations in crystals

Dislocation is a result of discontinuities in the crystal structure. A discontinuity is generated when a lattice mismatched layer is grown, as shown in Figure 2.16. The misfit interface stores an associated areal elastic energy density, E_h. When the thickness of the layer increases, E_h will become large enough to break atomic bonds at the strained interface and plastic deformation of the crystal will induce relaxation towards its bulk lattice constant. These deformations displace material along lines which form discontinuities in the lattice structure and break the commensurate nature of the misfit interface.

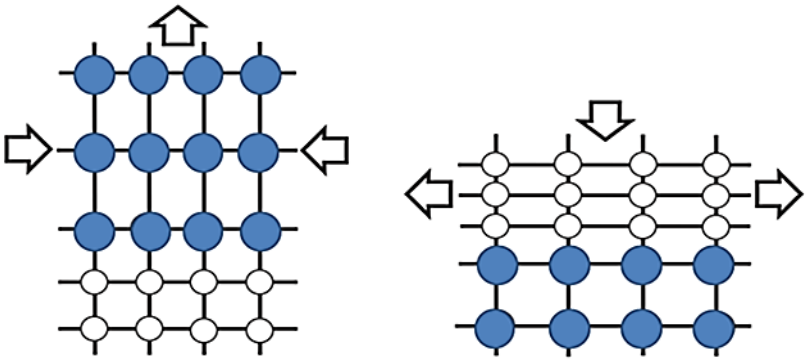

Figure 2.16: Schematic diagram of the growth of a lattice mismatched layer under (a) compressive and (b) tensile strain. [Adapted from Ref. 88]

The Burgers vector of a dislocation is a magnitude and direction of the distortion of the crystal lattice caused by the deformation. Dislocations have two primary types: edge dislocations and screw dislocations. If the Burgers vector is perpendicular to the dislocation line direction it is termed an edge dislocation. Otherwise, when the Burgers vector is parallel to the line direction it is termed a screw dislocation. Mixed dislocations are intermediate between edge and screw dislocations.

When dislocations are the boundaries of a slipped plane and generally comprise of two components; misfit dislocations and threading dislocations (Figure 2.17). The arms of the misfit dislocations that terminate at a free surface are called threading dislocations. The threading dislocation density (TDD) is the density of threading arms which reach the surface of a layer, and is usually quoted per unit area (in cm^{-2}).

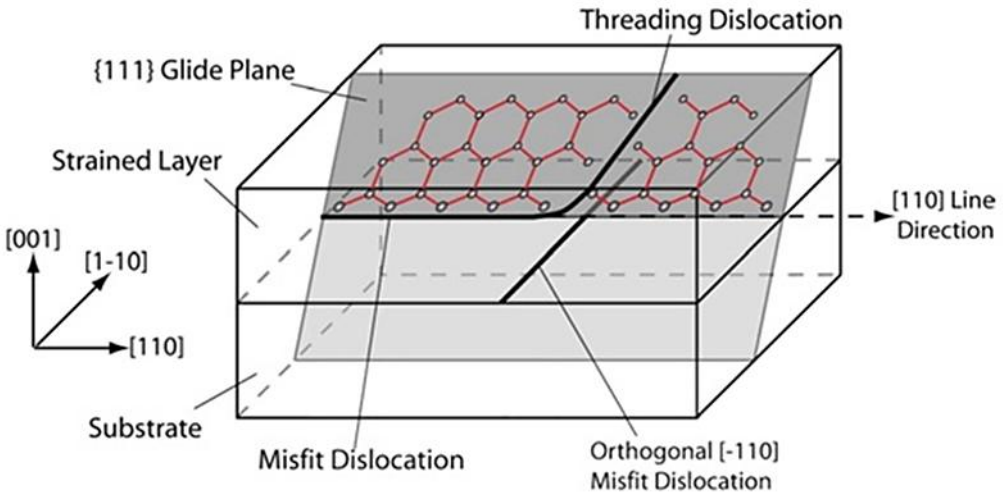

Figure 2.17: A physical representation of the threading and misfit dislocations as the boundary of a slipped plane which shows the order of bonds which are broken. [Adapted from Ref. 89]

When E_h stored in the epitaxial layer exceeds a certain threshold, the film strain tends to give way to misfit dislocations. The E_h is proportional to the thickness of the epitaxial layer, leading to a thermodynamically stable "critical thickness." The critical thickness of a strained layer is the maximum thickness for which it remains fully strained. Frank and van der Merwe were first to introduce this concept[90]. They obtained the critical thickness by minimizing the sum of the energy of interface incoherency, and the strain energy of the epitaxial film. After that Matthews and Blakeslee[90] explicitly derived an expression for the critical thickness by balancing the driving force from the epitaxial strain, and the force due to the line tension of a misfit dislocation. More recently, People and Bean[91] considered the misfit dislocations explicitly, but by taking an energy approach.

Dislocations have a pronounced effect on the electrical properties of germanium[92]. The dislocation creates energy states that lie in the energy gap between conductiona nad valance bands[92]. Previous works found that these dislocations act as acceptor centres[93,94]. When

dislocations are induced in materials, conduction electrons are scattered and thereby decrease the mobility[92]. Bardeen and Shockley's model[93] is approximately that the scattering potential of a charge carrier in a distorted semiconductor can be written in the form

$$V(r) = \left(\frac{E_1}{e}\right)\Delta(r) \ , \tag{2.31}$$

where E_1 is an experimentally defined parameter in the order of a few electron volts (eV). $\Delta(r)$ is the dilation of the lattice at the point r.

Koehler[94] use the theory of elasticity for a continuous isotropic medium to estimate the dilation around an edge-type dislocation. Therefore the scattering potential can be written in the form

$$V(r) = \left(\frac{\lambda}{2\pi}\right)\left(\frac{E_1}{e}\right)\left[\frac{(1-2\nu)}{(1-\nu)}\right] sin\,{}^{\theta}/_{r} \ , \tag{2.32}$$

where λ is the unit crystallographic slip distance, ν is the Poisson ratio, r is the distance from the dislocation axis (assumed straight line) and θ is the angle measured from the slip direction.

The average change in resistivity $(\Delta\rho)$ can be written in the form of equation (2.33). This equation was calculated by Dexter[95] with the assistance of $\langle k'|eV|k\rangle$, the scattering of electron in momentum state k to momentum state k'.

$$\Delta\rho = \frac{3\pi}{32}\frac{E_1\lambda^2}{k_0 T\hbar}\left(\frac{1-2\nu}{1-\nu}\right)^2 N\frac{m^*}{ne^2} \ , \tag{2.33}$$

where k_0 is Boltzmann's constant, T is the absolute temperature, E_1 is the density of dislocation lines per unit area, and n is the density of carriers.

The theoretically by Dexter and Seitz[96] presented that the reciprocal mobility is proportional to T, the absolute temperature. The reciprocal mobility can be written as

$${}^{1}/_{\mu} = \alpha_l T^{3/2} + \alpha_i T^{3/2} + \alpha_d T^{-1} \ , \tag{2.34}$$

and

$$\alpha_d = 300enT\Delta\rho \ , \tag{2.35}$$

where the α's are temperature independent parameter and the subscripts *l, i, d* denote the contributions to the scattering from the lattice, the impurities, and the dislocations.

In this, Ge was considered to be a suspended platform for low temperature application such as bolometer. Epitaxial grown Ge layers on Si substrates can be fully relaxed and have low defects. However, there is still has problem about electrical leakage because of conduction due to dislocation. The effect of dislocations on conductivity will be investigated in Chapter 5 where comparison will be made using structures where the majority of dislocations have been removed by fabricating an etched membrane.

3 Experimental Techniques

3.1 Introduction

In this chapter the principal methods of preparing and characterising samples will be outlined: chemical vapour deposition (CVD) used to grow material considered in this thesis; scanning electron microscope (SEM) used to examine the surface morphology; photolithography and dry etching to fabricate the mesa patterns investigated; and Hall measurements to determine the resistivity and mobility of the samples. All of these activities were performed at the University of Warwick, using facilities in the Department of Physics and School of Engineering.

3.2 Epitaxial growth of crystalline semiconductors

An essential feature of the material used in this work is that it consists of thin layers of crystalline material, which should be as free from defects and imperfections as possible. These layers were produced by a process of epitaxial growth[97]. Epitaxy is successfully employed in silicon-based manufacturing processes for bipolar junction transistors (BJTs)[98], complementary metal–oxide–semiconductors (CMOS)[99] and dynamic random access memory (DRAM)[100]. Moreover, epitaxy is more generally used in nanotechnology and in semiconductor fabrication[101].

'Epitaxial' means the growth of a single crystal film on top of a crystalline substrate in an ordered way such that both materials should have the same structure and orientation[102]. It is called 'non-epitaxial growth' if the overlayer forms a random orientation with respect to the substrate or does not form an ordered overlayer. If the epitaxial layer is fully commensurate with the substrate, in other words if the atomic positions align, then the growth is termed 'pseudomorphic'.

Homoepitaxy is the epitaxial deposition process in which overlayer material and the substrate are the same e.g. a Si layer deposits on top of a Si substrate.

Heteroepitaxy is the epitaxial deposition process in which overlayer material is different from the substrate, leading to unmatched lattice parameters e.g. AlGaAs epitaxy on GaAs substrate or SiGe epitaxy on Si substrate. This is a powerful technique that can be used to construct essentially new materials where the electronic, optic, thermal and mechanical properties can be different in the heterostructure from those in either of the constituent materials. Since the lattice parameters can be significantly different, for instance by 4.2% between Si and Ge, pseudomorphic growth, where the overlayer takes on the in-plane lattice parameter of the much thicker substrate, will lead to a strained epilayer. If the layer is under biaxial compression then the lattice parameter in the growth direction will be elongated such that the unit cell volume remains almost constant. There is a critical thickness for strained layers[75] that can be supported before relaxation of the strain takes place by formation of misfit dislocations at the interface, this is termed 'metamorphic' growth. The misfit segments that lie along the interface will relieve strain, but they are of finite length and terminate in threading dislocations which can penetrate up through the epilayer and degrade the properties of the material, so steps need to be taken to minimise this threading dislocation density (TDD).

There are two main processes of epitaxial growth, molecular beam epitaxy (MBE) and chemical vapour deposition (CVD).

3.2.1 Molecular beam epitaxy (MBE)

Molecular Beam Epitaxy (MBE) is an ultra-high vacuum (UHV) technique that operates at about total pressure $< 10^{-10}$ Torr[103] to make epitaxy such as compound semiconductor with extreme precision less than 0.01 nanometer and purity higher than 99.99999% due to the

absence of carrier gases as well as the ultra-high vacuum environment. This epitaxy is layered one on top of another to form semiconductor devices, such as transistors and lasers. These devices are being used in applications such as fiber optics, cellular phones, satellites, radar systems, solar cells, and display devices. These also include the growth and development of mid- and far-infrared (terahertz) quantum cascade lasers and the fabrication of advanced materials such as low-temperature gallium arsenide and related compounds that is used for optical mixers and electro-optic switches. A molecular beam epitaxy (MBE) growth chamber is shown in Figure 3.1.

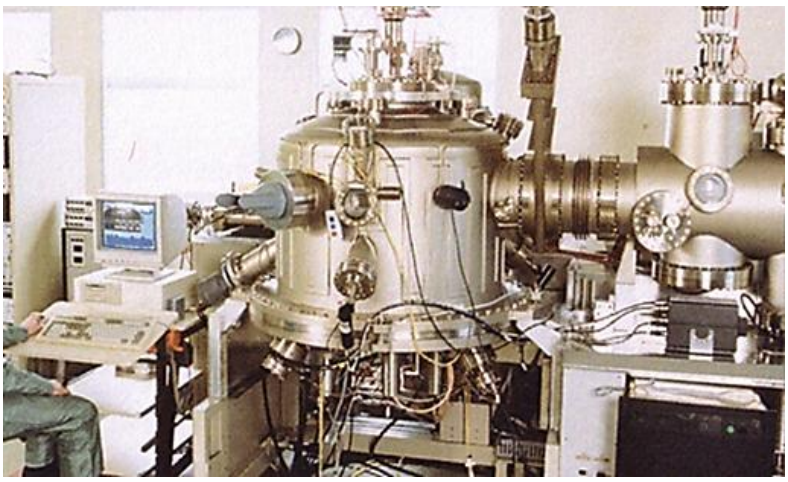

Figure 3.1: MBE-V90S-ANT at Nanosilicon group, Department of Physics, University of Warwick

The molecular beam epitaxy deposition process is simple: the material, solid source that needs to be deposited is heated in UHV and produces atoms or clusters of atoms to form a molecular beam. Then, they migrate in an UHV environment to interact with the atoms of a hot substrate surface. This interaction depends on the type of adatoms (the atoms of the beam that adsorbed by the sample surface), the substrate, and the temperature of the substrate. Once on the surface, the adatoms can diffuse and subsequently form thin layers on the substrate as

shown in Figure 3.2. The growth rate should be small (0.05 - 1 Å/s) and the vacuum pressure is very low as well about a few 10^{-12} Torr to achieve good quality film growth.

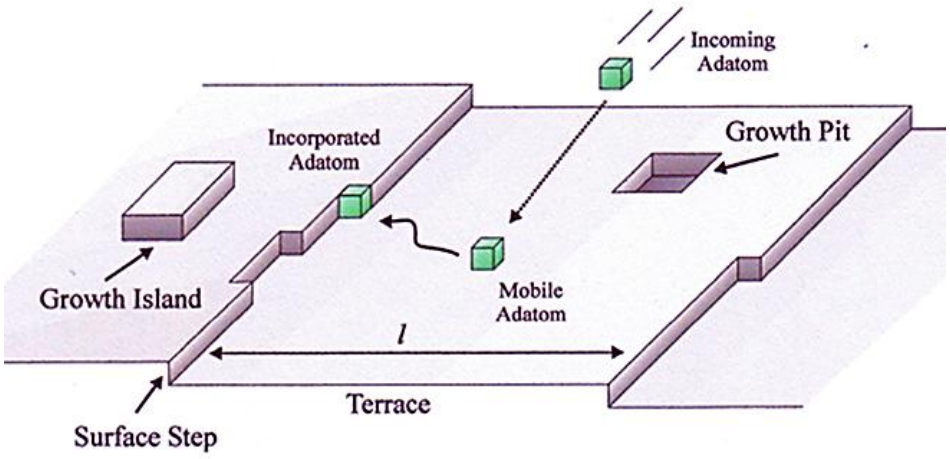

Figure 3.2: The diffusion of adatoms on the hot substrate surface to form the layer.

[From Ref. 103]

3.2.2 Chemical vapour deposition (CVD)

Chemical vapour deposition (CVD) is the process that deposits a solid material onto a heated substrate to form a film through decomposition or chemical reaction of vapour phase chemical reactants containing the right constituents. The process can be used to deposit many materials, such as silicon nitride, silicon dioxide, non-crystalline silicon and single crystal silicon. Chemical vapour deposition is the main process of film deposition for the semiconductor industry because CVD is high throughput, high purity, extremely reproducible from wafer to wafer and day to day, and low cost. CVD is commonly used in optoelectronics[104] such as light emitting diodes (LEDs)[105], optical coatings, and coatings of wear resistant parts[106]. CVD is also used in the production of microelectromechanical structures (MEMS)[107]. A schematic diagram of a cold-wall rotating disk CVD system is presented in Figure 3.3. An example of a silicon wafer using the CVD technique as shown in Figure 3.4.

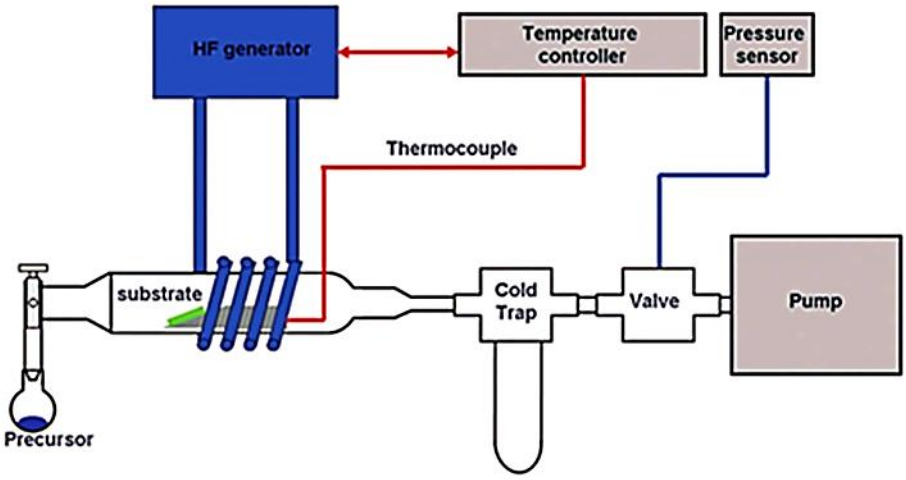

Figure 3.3: Schematic of a typical cold wall CVD reactor [From Ref. 108]

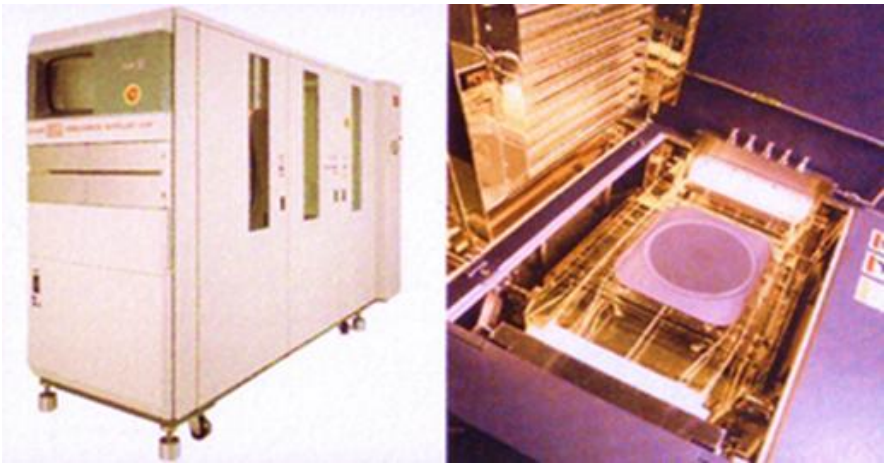

Figure 3.4: LP-CVD-ASM Epsilon 2000E at Nanosilicon group, Department of Physics, University of Warwick

In the typical CVD process, as shown in Figure 3.5, a precursor gas flows into the chamber, containing one or more heated objects to be coated. Then, chemical reactions occur on and near the hot surface, which leads to deposition of a thin film on the surface. The chemical by-products and unreacted precursor gas are removed from the chamber by the main process pump (that also causes the in-flow of the precursors) and expelled through an abatement system that removes undesirable compounds from the exhaust to the environment. There are four basic types of CVD reactor: atmospheric pressure CVD (APCVD), low pressure CVD (LPCVD) about 0.2 – 20 Torr, metal organic CVD (MOCVD) and plasma enhanced CVD (PECVD).

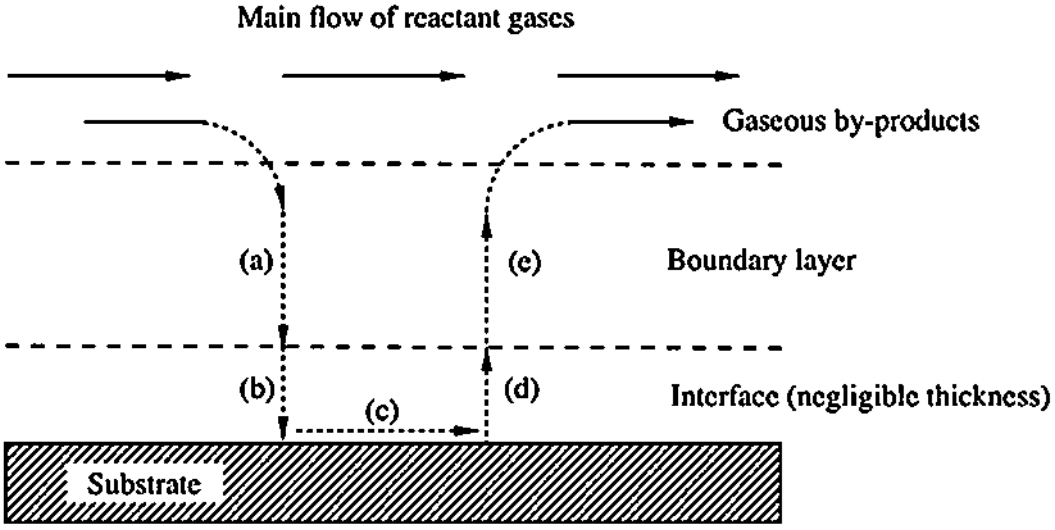

Figure 3.5: Sequence of events during CVD: (a) diffusion of reactants through boundary layer, (b) adsorption of reactants on substrate, (c) chemical reaction takes place, (d) desorption of adsorbed species, and (e) diffusion out of by-products through boundary layer [From Ref. 109]

All the material used in this study was grown by reduced pressure CVD (RP-CVD), which is a variant on LPCVD. This process has the advantageous of being compatible with industrial processing, which would be an advantage if the structures considered here were to be commercialised since the RP-CVD process could be directly ported from the Warwick research reactor into a silicon process facility.

3.3 Material characterization

Material characterization covers the techniques used to probe or examine the internal structure and properties of a material. To analyse and examine all materials, the use of a wide range of advanced techniques is required. For this work, it is especially useful to be able to examine the microstructure of the material, including the distribution of elements and their interactions within the specimen. The techniques used include Optical Microscope, Scanning Electron Microscope (SEM), Transmission Electron Microscope (TEM), Field Ion Microscope (FIM), Scanning Tunnelling Microscope (STM), Atomic Force Microscope (AFM), and X-ray diffraction topography (XRT).

3.3.1 Electron microscope (EM)

An electron microscope (EM) is a type of microscope that produces a magnified image of extremely small objects by using an electron beam rather than visible light. As electrons have a much shorter wavelength than light, by about 100,000 times, the electron beam can resolve much finer structural details of the specimen. The EM resolution can be better than 50 pm and up to 10,000,000x of magnification. The electrons are first accelerated by voltages of up to 100 keV (or higher in some transmission electron microscopes) and the electron beam formed is controlled and focused on the specimen by electrostatic and electromagnetic lenses. After interacting with the specimen being observed, the refracted or reflected beams are converted into an image by the detector and associated image reconstruction software.

Electron microscopy is used to investigate a wide range of biological and inorganic specimens that are ultra-small structure. The well-known types of electron microscope are scanning electron microscope (SEM), transmission electron microscope (TEM) and scanning transmission microscope (STEM).

3.3.1.1 The scanning electron microscope (SEM)

The scanning electron microscope (SEM) as shown in Figure 3.6 is a type of electron microscope (EM) that is the most widely used of all electron microscopes. SEMs can create an image of much higher magnification and resolution than light microscope, as shown in Figure 3.7. SEM examines a specimen by scanning an electron beam across its surface in a raster pattern. The electrons interact with atoms in the specimen. The interaction produces the various signals that can be detected by the detector, which can be based either simply on the current of electrons received or be energy dispersive. The signal includes the information of the sample's surface topography, external morphology (texture) and composition such as chemical composition, and crystalline structure and orientation of materials. The accelerated electrons created in an SEM have significant amounts of kinetic energy. When the accelerated electrons interact with specimen, the incident electrons are decelerated and produce a variety of signals. One of these signals is secondary electrons which are emitted from the specimen surface. SEM image can be produced from secondary electrons signals.

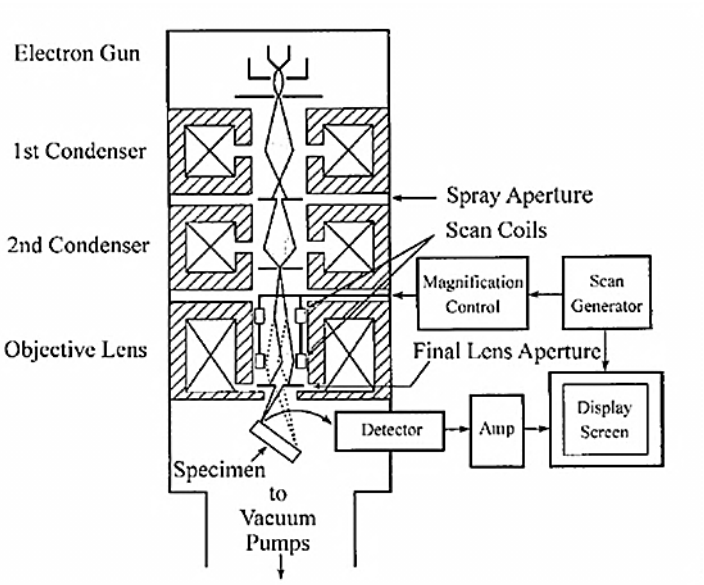

Figure 3.6**:** The structure of a scanning electron microscope (SEM) [From Ref. 110]

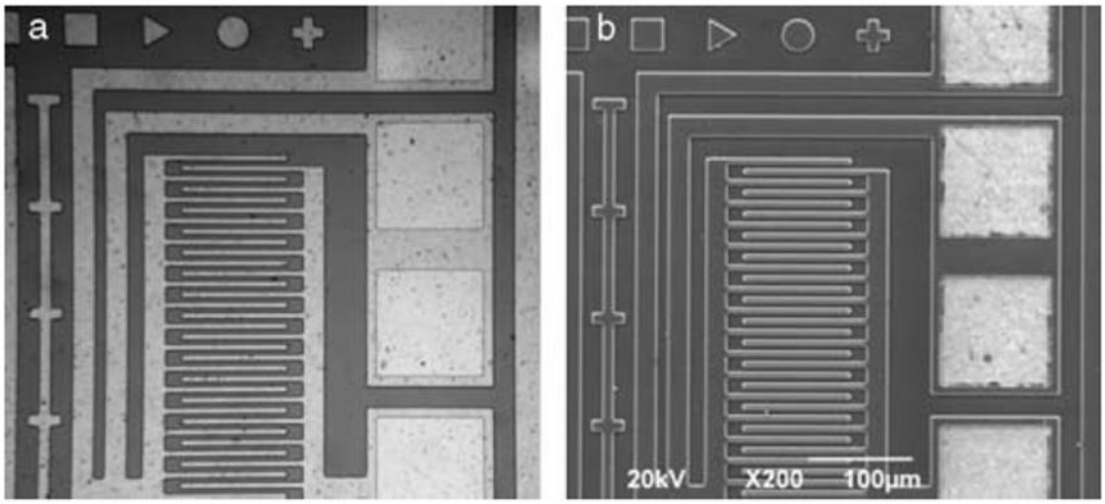

Figure 3.7: Comparison of light microscope with scanning electron microscope at the same magnification a) light microscope image b) SEM image [From Ref. 111]

Materials to be examined by SEM should comply with the conditions below:

1. The specimens should fit in the specimen chamber.
2. The specimens must be clean, because dirt could interfere with electron beams.
3. The specimens are completely dry, because SEM works in vacuum.
4. The specimens must be electronically conductive, so that it does not charge up and thereby deflect the electron beam. Non-conducting samples can be coated with gold or platinum.

In this thesis, specimens were examined using an accelerating voltage of 5 kV and a Zeiss Supra InLens secondary electron detector as shown in Figure 3.8. Since the specimen is Si and Ge it is not necessary to coat with a conductive layer. The full size of specimen is about 7x7 mm^2. Then specimen was cleaved in the direction perpendicular with the mesa line (more details in Chapter 4) to investigate the side wall profile as shown in Figure 3.9. After that, the specimen was mounted on the slotted head as shown in Figure 3.10. Then the slotted head with specimen was mounted on the holder such that the cross section of the specimen was tilted at 90^o with respect to the side wall being examined, as shown in Figure 3.11. Figure 3.12 shows the top view of Figure 3.11 that is the similar view pointed from Inlenses of SEM.

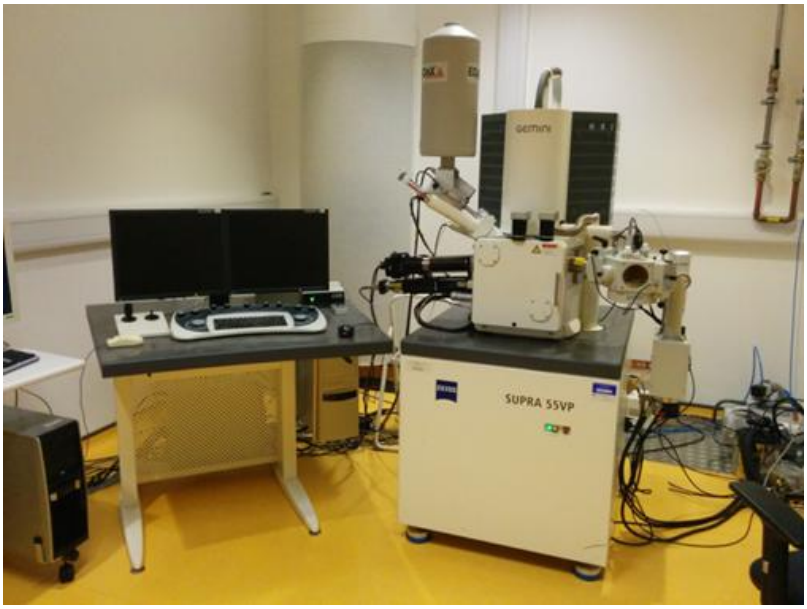

Figure 3.8: The SEM, Zeiss Supra InLens secondary electron detector at Department of Physics, University of Warwick

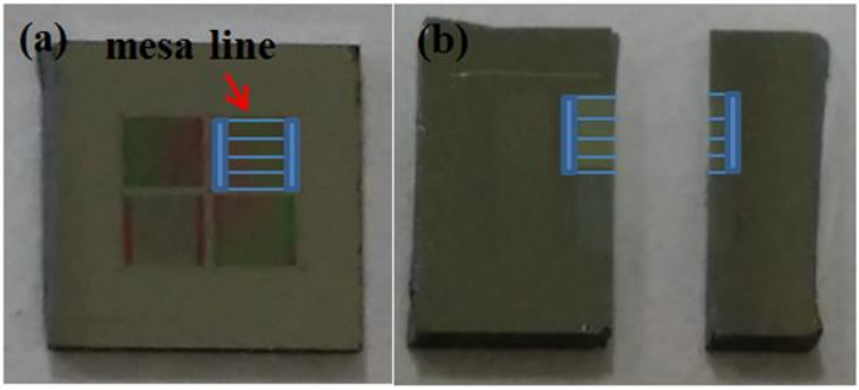

Figure 3.9: The Specimen (a) Full size specimen (b) Cleaved specimen

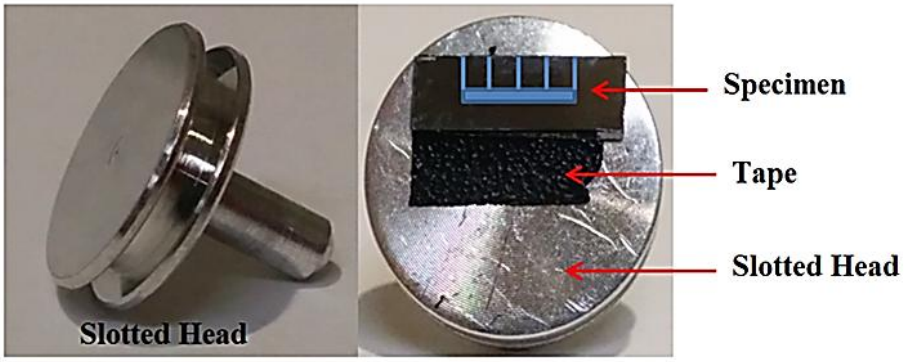

Figure 3.10: The slotted head for mounting specimen

Figure 3.11: The SEM holder

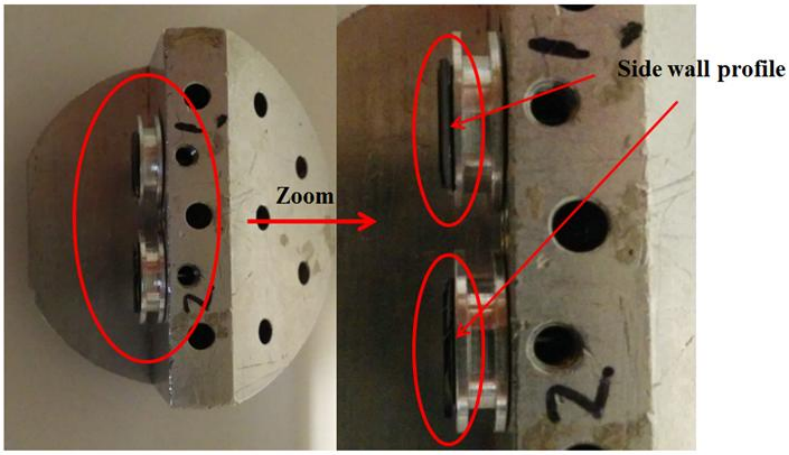

Figure 3.12: The top view look like seen by InLens of SEM

3.4 Device fabrication

The original aim of this work was to make electronic cooling structures which required fabrication of devices. However, as will be seen in Chapter 4, a significant amount of research was first needed into the actual fabrication process, especially in terms of etching Ge. Once the fabrication process had been optimised it also became possible to create a number of different suspended structures that will be discussed in Chapter 5. Here a brief overview of the fabrication process will be presented.

3.4.1 Photolithography

Photolithography is a process used to pattern shapes on thin films or the bulk of a substrate. The geometric pattern from a photomask is transferred to a photosensitive material, photoresist, on the substrate using UV light. Photolithography is mainly applied in microfabrication, IC production. Coarser version are also used in printed electronic board, nameplates etc.

The basic procedure is presented in Figure 3.13. First, Figure 3.13 (a), the substrate is cleaned with wet chemical treatment e.g. RCA clean and then was heated to drive off any moisture. After that the substrate is covered with photosensitive material or photoresist by using spin coating. The spin speed should be at 1200 rpm to 4800 rpm for 30 s. to 60 s. to produce a uniform thin layer of photoresist between 0.5 and 2.5 μm[112]. The photoresist coated substrate is then baked (60°-100°C) again to drive off excess photoresist solvent and improve adhesion, so-called soft baking or prebaking[112]. After baking, Figure 3.13 (b), the photoresist coated substrate is exposed to UV light (400 nm to about 150 nm). A XeCl laser, 308 nm or a KrF laser 248 nm can achieve the excellent quality images[113]. The UV causes a chemical change in the photoresist so that some parts of photoresist can be removed from substrate by using developer solution. There are two types of photoresist: positive and negative, Figure

3.13 (c). Positive photoresist is the most common type. The parts of positive photoresist that have been exposed to the UV light can be washed away by developer solution. Conversely, negative photoresist becomes polymerized and unstable when exposed to UV light. After SiO_2 sample etching process, Figure 3.13 (d), the final step is photoresist removal, Figure 3.13 (e). When photoresist is unwanted, it must be removed from the substrate via resist stripper. The alternative process is etching (e.g. plasma etching using oxygen gas).

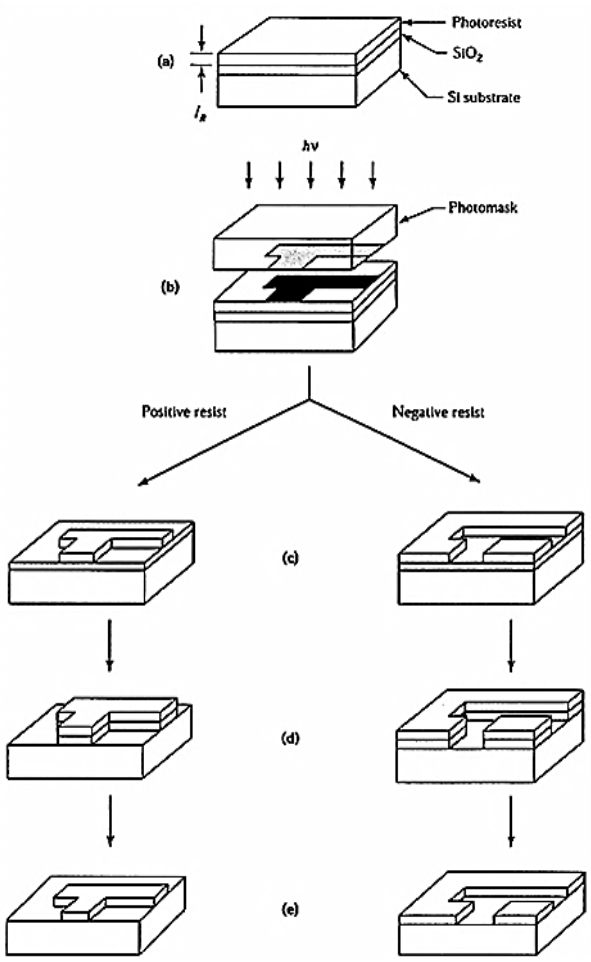

Figure 3.13: The basics process of photolithography: (a) Photoresist deposition (b) Photoresist exposure (c) Development (d) SiO_2 sample etching process (e) Photoresist removment [From Ref. 114]

3.4.2 Etching

In order to fabricate a functional microelectromechanical systems (MEMS) structure on a substrate, it is necessary to etch unwanted material that has been deposited and/or the substrate itself. In general, there are two classes of etching processes: wet etching and dry etching.

Wet etching is a process in which liquid chemicals or etchants are utilized to remove materials from the wafer. When the wafer is etched, the portion of the material that is covered by a mask is protected. For example, the sample may be composed of substrate B (Si) covered by A (SiO_2) as shown in Figure 3.14. When the samples are exposed to a HF etchant, the HF can etch the area of material A by photoresist until it reaches material B. Finally, when the photoresist is removed, it completes the channel structure. More details about wet etching can be found in chapter 5.

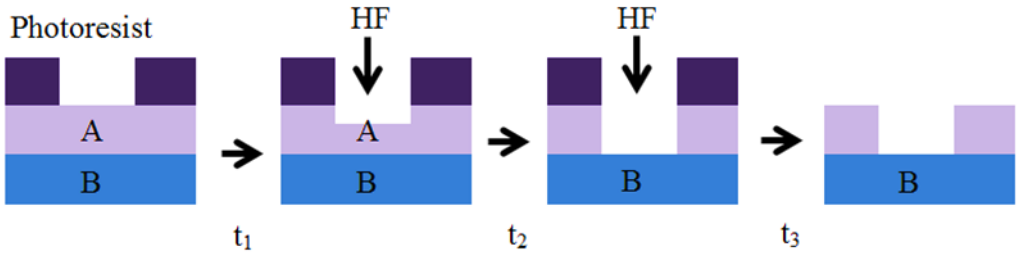

Figure 3.14: Wet etching process

Dry etching uses gas-phase reactions (normally in a plasma) that form highly reactive species. These species impinge on the surface to react with it and/ or erode it. Figure 3.15 shows the various processes that can occur in the plasma directly above the surface to be etched.

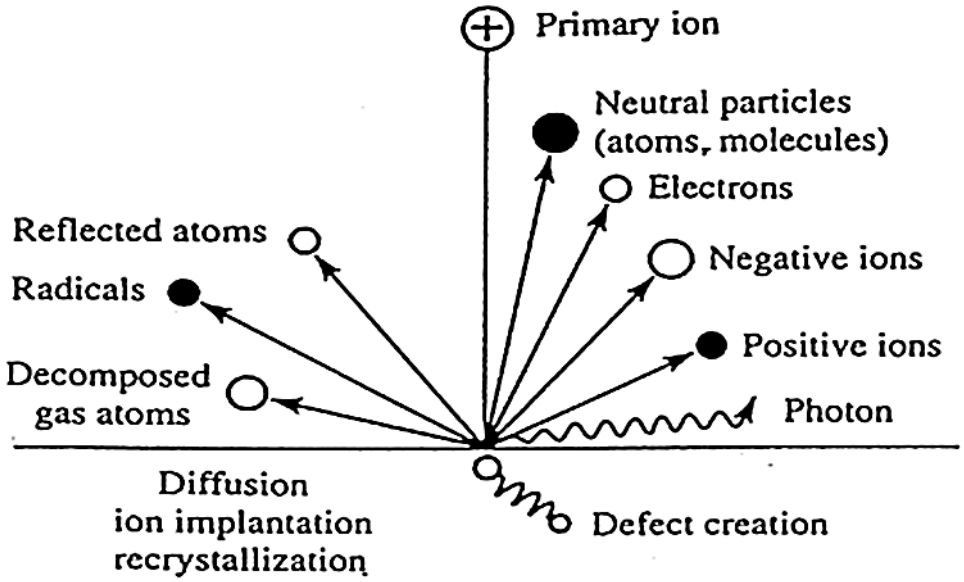

Figure 3.15: Plasma interaction with the surface [From Ref. 115]

The incident ion may be reflected or neutralized. The surface may eject an electron or positive and negative ions or atom (sputtering) or an atom may be implanted in the surface. Unfortunately, the incident ion may cause a defect. These processes can result in structural rearrangement of the material, causing the surface to be reactive to other gas molecules that exist in the plasma. More details about dry etching can be found in chapter 4.

Dry etching has a number of advantages. The etch direction is not dependent on the crystal orientation as is the case in wet etching of single crystals like silicon, germanium or gallium-arsenide. The dry etching is cleaner and compatible with vacuum- processing technologies in comparison with wet etching. The disadvantages of dry etching are its high cost, implementation difficulty, and the possibility of damaging the specimen with highly energetic ions. By contrast, wet etching is low cost and easy to implement. Unfortunately, wet etching has a number of disadvantages. For Very Large Scale Integration integrated circuits, the aspect ratio of wet etching is not acceptable[116]. Since wet etching is a chemical process, the

disposal of partly used reagent can cause environmental problems. Moreover, the etch depth is difficult to control *in situ*.

3.4.3 Etch rate

In designing a microfabrication process, it is important that the etch rate of each material is known. If we know the etch rate of all materials that will be exposed to the etch, such as masking films and underlying layers, it will help to achieve good selectivity (high ratio of etch rate of the target material to etch rate of the other materials).

In this thesis, we use a "step height" technique in order to measure the etch rate. The samples are produced in an array of mesas. The mesa pattern and the process flow are shown in Figure 3.16. The mesa array of photoresist shown in Figure 3.16 a) was fabricated using photolithography. Then, the mesa array substrate was etched by using plasma dry etching, i.e. reactive ion etching (RIE) using SF_6-O_2 gas mixtures (20% of O_2 – 80% of SF_6). More detail can be found in Chapter 4. After etching, both the substrate material and photoresist were etched. The height that was measured in this step is equal to $h_2 + h_3$. As the final step, the array of photoresist was washed away and the height of substrate material (h_3) can be measured. The height of photoresist was measured using an Ambios XP-100 step profilometer as shown in Figure 3.17. In doing this, we can calculate the etch rate of substrate and photoresist (nm/second). Results are presented in section 4.3.

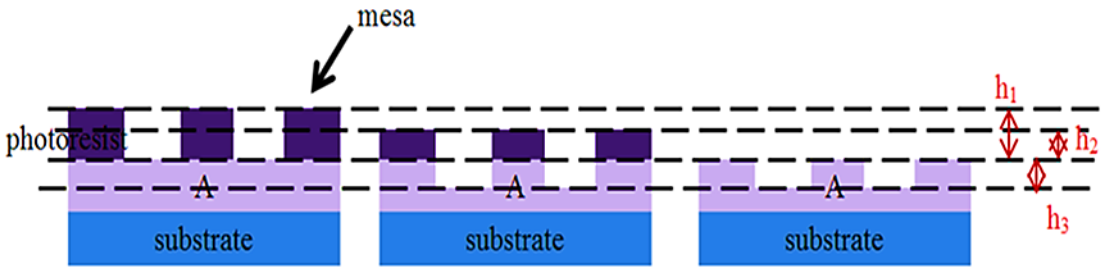

(a) (b) (c)

Figure 3.16: a) Patterned mesa array using photolithography

b) Plasma dry etching with SF_6-O_2 c) Removal of photoresist

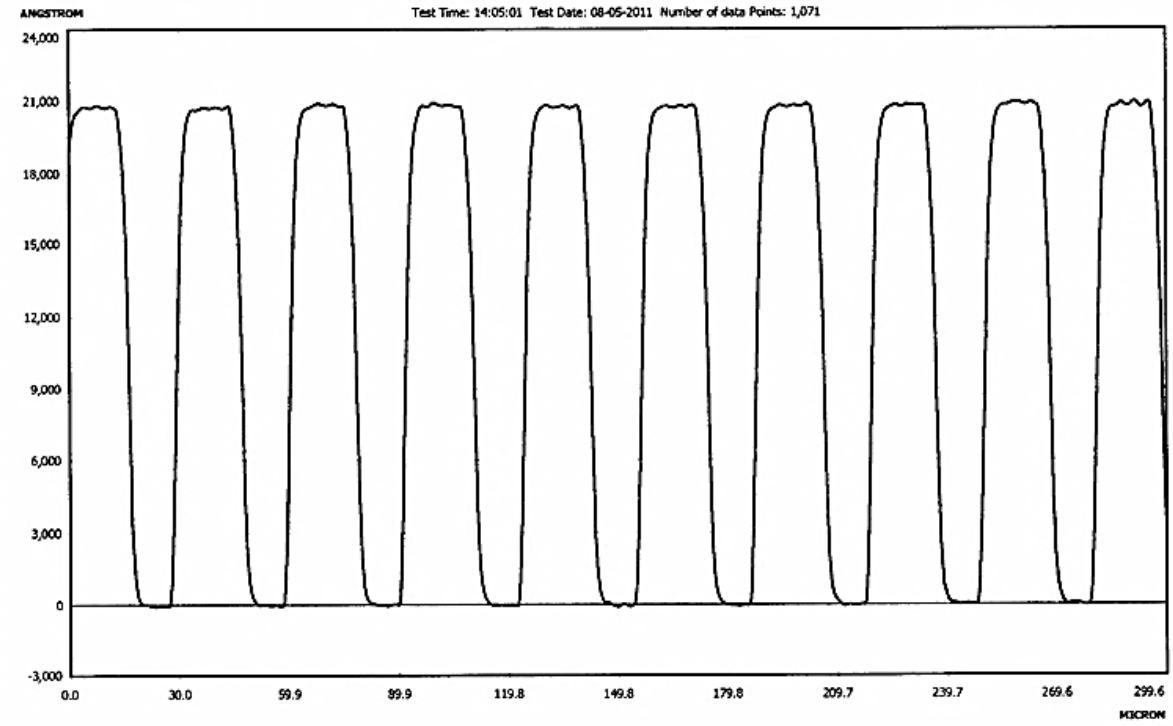

(a)

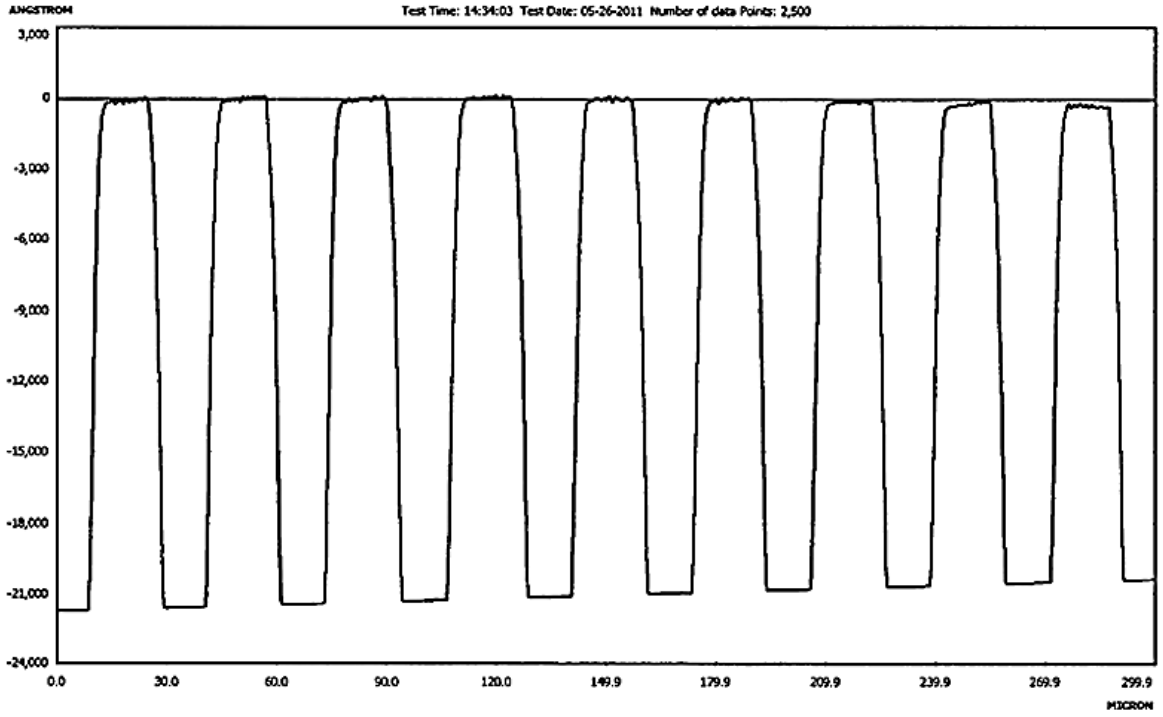
ANGSTROM
Test Time: 14:34:03 Test Date: 05-26-2011 Number of data Points: 2,500
3,000
0
-3,000
-6,000
-9,000
-12,000
-15,000
-18,000
-21,000
-24,000
0.0
30.0
60.0
90.0
120.0
149.9
179.9
209.9
239.9
269.9
299.9
MICRON

(b)

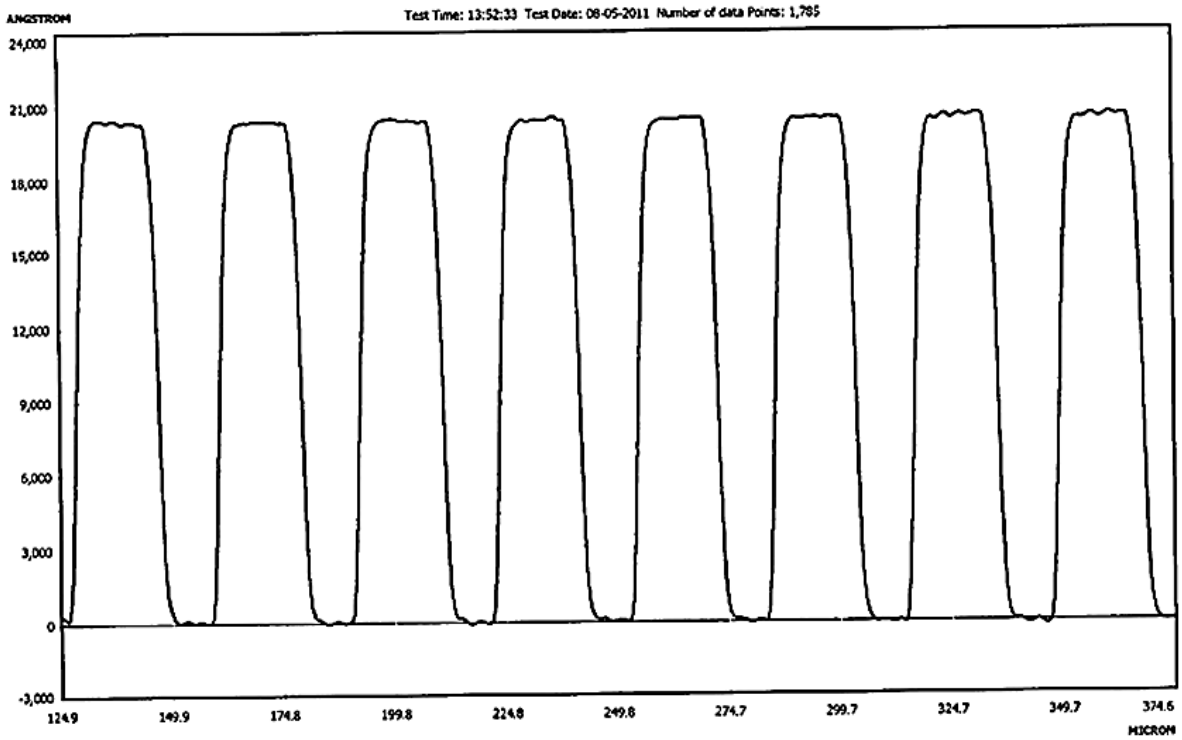
ANGSTROM
Test Time: 13:52:33 Test Date: 08-05-2011 Number of data Points: 1,785
24,000
21,000
18,000
15,000
12,000
9,000
6,000
3,000
0
-3,000
124.9
149.9
174.8
199.8
224.8
249.8
274.7
299.7
324.7
349.7
374.6
MICRON

(c)

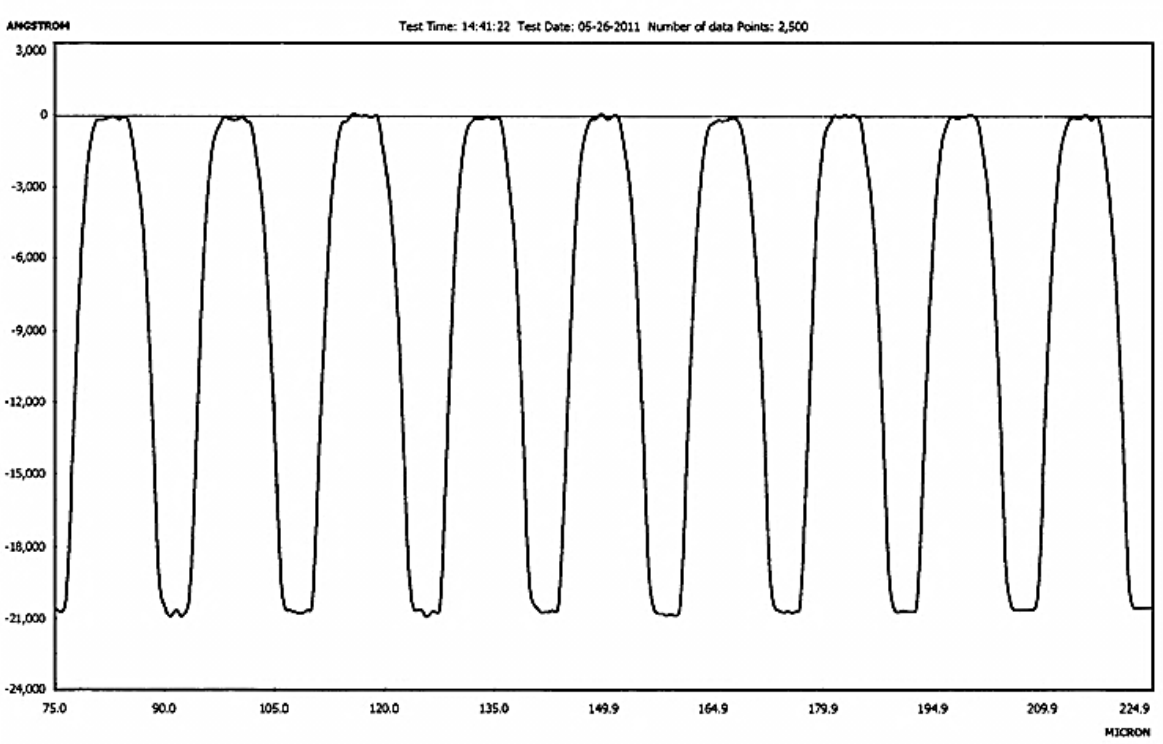
ANGSTROM
Test Time: 14:41:22 Test Date: 05-26-2011 Number of data Points: 2,500
3,000
0
-3,000
-6,000
-9,000
-12,000
-15,000
-18,000
-21,000
-24,000
75.0
90.0
105.0
120.0
135.0
149.9
164.9
179.9
194.9
209.9
224.9
MICRON

(d)

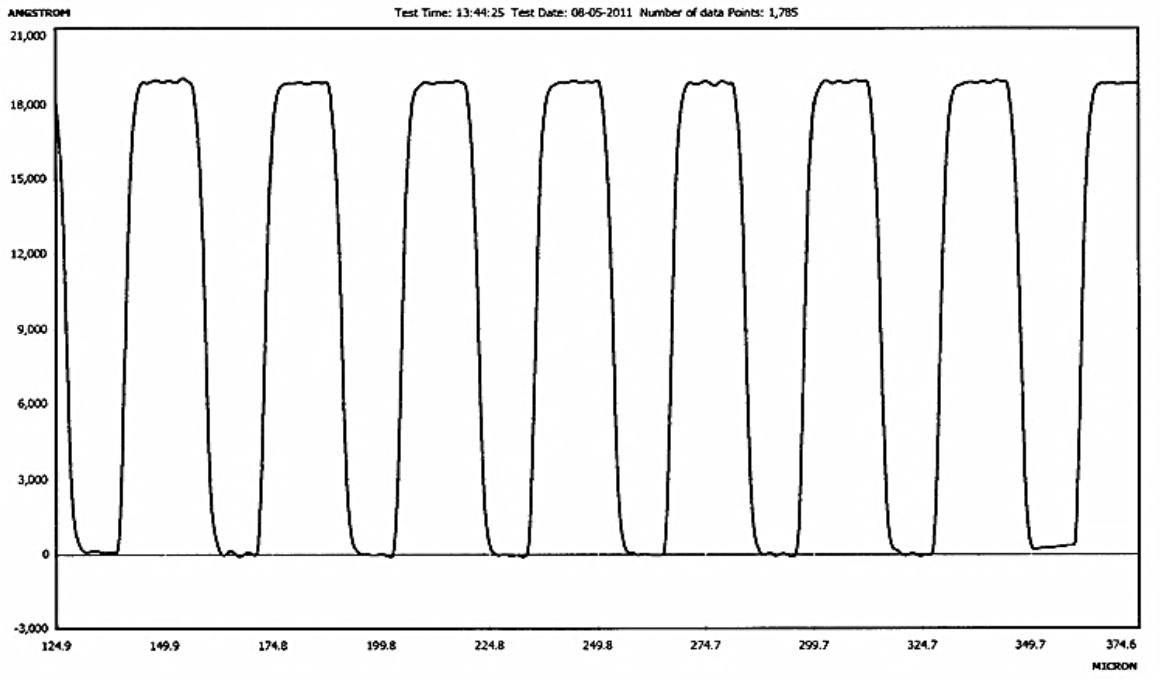
ANGSTROM
Test Time: 13:44:25 Test Date: 08-05-2011 Number of data Points: 1,785
21,000
18,000
15,000
12,000
9,000
6,000
3,000
0
-3,000
124.9
149.9
174.8
199.8
224.8
249.8
274.7
299.7
324.7
349.7
374.6
MICRON

(e)

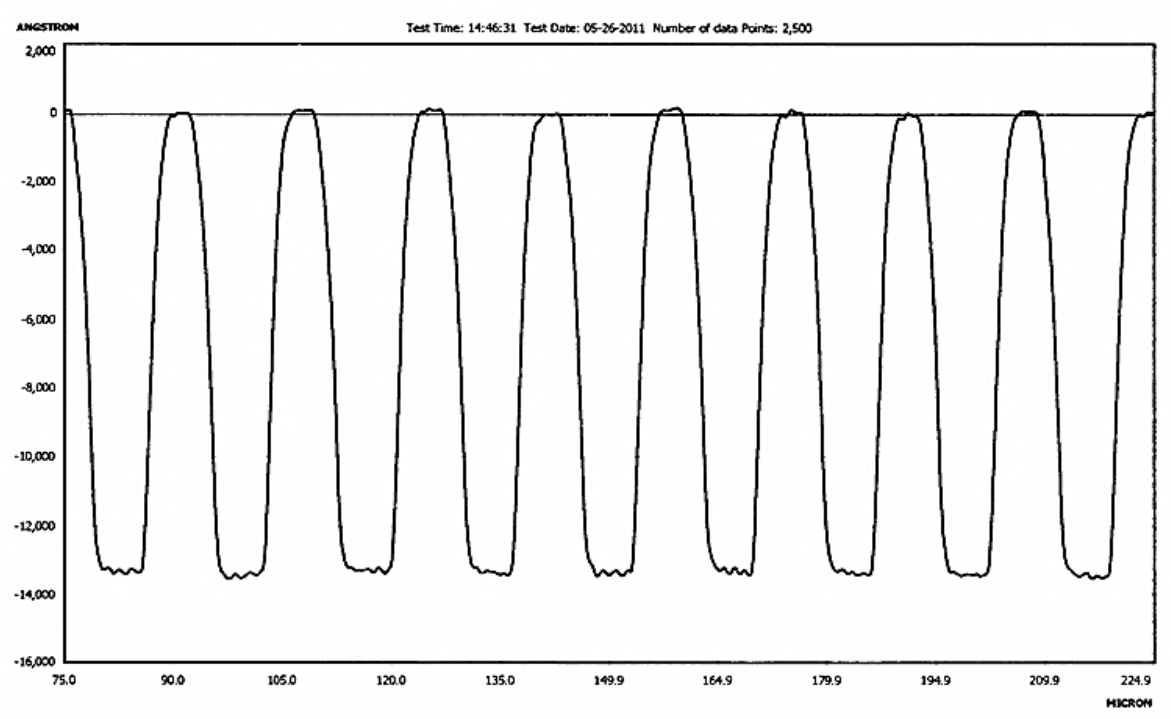

Figure 3.17: The step height of array of mesas that was measured by Ambios XP-100 step profilometer for calculation of the etching rate, etched by SF_6-O_2 gas mixture (30 sccm) :

(a) 5% O_2 (b) 20% O_2 (c) 35% O_2 (d) 50% O_2 (e) 70% O_2 (f) 90% O_2 of 30 sccm

3.5 Electrical characterisation

3.5.1 Hall measurement

The Hall effect is the production of a potential difference (the Hall voltage) on opposite sides of an electrical conductor, which is transverse to an electric current in the conductor and a magnetic field perpendicular to the current. The physical cause of Hall effect is the Lorentz force. This force is composed of both an electric force and a magnetic force. Then, the Lorentz force is equal to $-q(E + vXB)$ where q (1.602x10^{-19} C) is the elementary charge, E is the electric field, v is the particle velocity, and B is the magnetic field. The Hall effect is presented in Figure 3.18. The electric field E_x and current density j_x are applied in the x-direction. The Hall field E_H is generated by the Lorentz force. Classically, for a single type of charge carrier, the Hall coefficient is $R_H = 1/ne$, which enables the carrier density in the

material to be measured. The sign of the Hall coefficient can be used to determine whether the carriers are *n*-type (electrons) or *p*-type (holes).

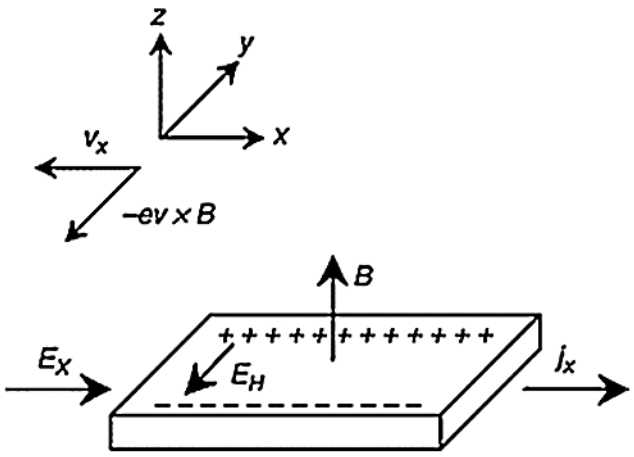

Figure 3.18: The Hall effect in a bar of conducting material [From Ref. 117]

A resistivity measurement aims to measure the sheet resistance R_S of a material. However, a simple measurement of voltage divided by current through a material will also include the resistance of the contact regions and connecting leads as well as the actual resistance that is required. To avoid this, four point measurements are used, with the voltage detected from additional contacts through which essentially no current flows and so no voltage is dropped. For an arbitrary geometry with contacts on the edge, Van der Pauw demonstrated that R_S can be measured via two characteristic resistances R_A and R_B that are related to the sheet resistance R_S through the van der Pauw equation

$$\exp(-\pi R_A/R_S) + \exp(-\pi R_B/R_S) = 1 \quad . \tag{3.1}$$

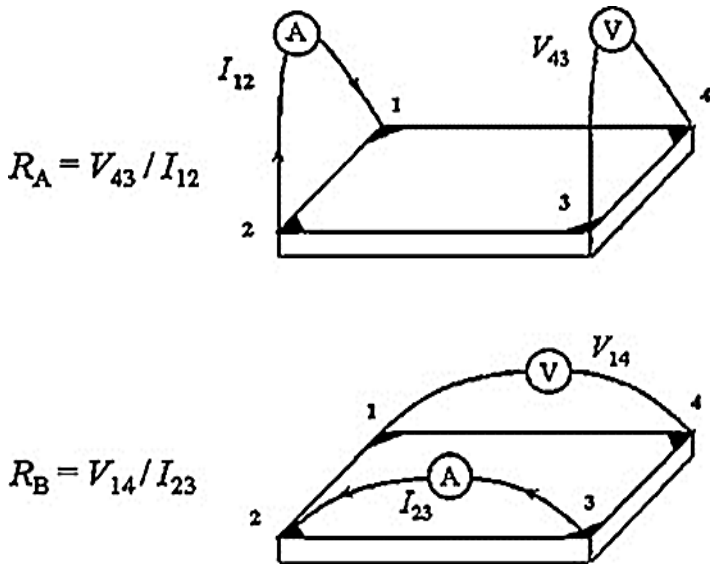

Figure 3.19: Arrangement for resistivity measurement [From Ref. 118]

To obtain the two characteristic resistances R_A and R_B, the measurement is set up as shown in Figure 3.19. The four leads are connected to four ohmic contacts on the sample. These are labelled 1, 2, 3, and 4 counter clockwise. In order to minimize thermoelectric effects, it is important to use the same batch of wire for all four leads. In the same way, all four ohmic contacts should consist of the same material. Then a dc current I (I_{12}) applies into contact 1 and out of contact 2 and measures the voltage V_{43} from contact 4 to contact 3. Next, the current I (I_{23}) applied into contact 2 and out of contact 3 while measuring the voltage V_{14} from contact 1 to contact 4. R_A and R_B are calculated by means of the following expressions:

$$R_A = V_{43}/I_{12} \quad \text{and} \quad R_B = V_{14}/I_{23}$$

3.5.2 Mobility measurement

To determine the carrier mobility (μ), the first step is to measure the Hall voltage (V_H) by forcing both a magnetic field (B) perpendicular to the sample and current (I) through the sample causing the transverse current as shown in Figure 3.15. The Hall voltage can be measured across the device ($V_H = V_{24}$) and current I is I_{13}. Therefore, the Hall mobility can be calculated by using this formula:

$$\mu = {|V_H d|}/{BI\rho} \quad , \tag{3.2}$$

where d is sample thickness and ρ is resistivity

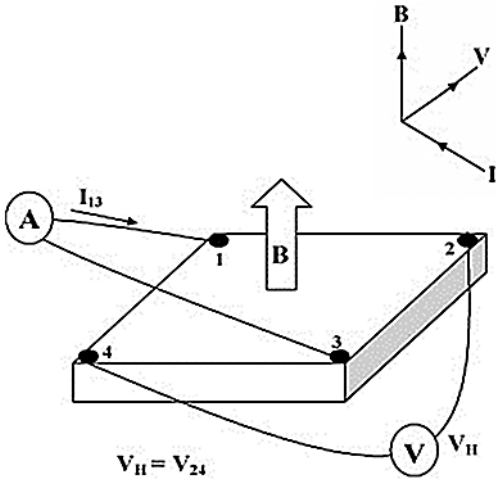

Figure 3.20: Arrangement for Hall voltage measurement [From Ref. 119]

In Chapter 5, the Hall measurement is used to investigate the resistivity and mobility of bulk and suspended Ge. The van der Pauw Greek cross is the platform of the bulk Ge and suspended Ge for the Hall measurement. Resistivity measurements are measured at room temperature down to 15 K by using current in the order of 0.1 – 0.2 μA. Mobility measurements measured in a field of 600 mT at temperature between 15 K and room temperature (300 K).

4 The Dry Etching Process in SF_6-O_2 Radio-Frequency Plasma

4.1 Introduction

In this chapter reactive ion etching (RIE) of single crystal Ge is investigated, in particular at low working pressures where the physical etching is more prevalent. Experiments were also performed to determine whether phosphorus doping affects Ge etching. In addition, the research also investigates how the $\%O_2$ in the SF_6-O_2 gas mixture influences the side wall orientation and profile for room temperature SF_6-O_2 dry etching. Si is used as the control material.

Dry etching for micro and nanofabrication has been widely investigated and is used extensively in CMOS processes where arbitrary shapes and complex design is required. SiGe heterostructures are increasingly used in advanced complementary metal–oxide–semiconductor (CMOS)[120], bipolar junction transistor (BJTs)[121] and have gained recent interest as optoelectronic devices[122]. For such devices, dry etching techniques enable selective removal of Si, Ge or SiGe alloy layer through masking techniques which gives superior dimensional control and process flexibility, relative to wet etching processes[123]. Anisotropy of the dry etch process can be achieved and is useful for mesa definition[124]. Anisotropic dry etching is used in device isolation[125], in modern DRAM capacitor[126] and in power device fabrication[127].

Reactive ion etching (RIE) is most commonly used during semiconductor device fabrication as it allows both physical and plasma etching simultaneously. Physical etching is caused by sputtering effects due to energetic positive ions with energies below 500 eV[128]. Plasma etching involves a chemical reaction using a gas glow discharge to dissociate and ionize radicals, which react chemically with the material surface to form volatile products.

Because physical etching can result in structural rearrangement of the surface, it may affect the chemical reactions. With SF_6 gas, energetic ions are generated that remove material by physical sputtering, and fluorine radicals that etch material by chemical reaction. Adding O_2 in SF_6 influences primarily the chemical reaction processes, allowing control of the etch rate and sidewall profile.

The started point of using SF_6-O_2 plasma etching was presented by d'Agostino and Flamm[129]. They suggest that the SF_6-O_2 gas mixture is an alternative to replace the CF_4-O_2 gas mixture currently used for Si and SiO_2 dry etching, as the SF_6-O_2 gas mixture shows a rapid etch rate and also obtained a high selectivity in favour of silicon. Compared to a CF_4-O_2 gas mixture, the key to the rapid etch rate of the SF_6-O_2 gas mixture is the greater concentration of F radicals.

Syau *et al.*[130] used reactive ion etching (RIE) to investigate the etching process of SF_6-O_2 plasma via etching Si and SiO_2. Their main interest was in anisotropic etching of deep trenches. The best condition that they found for achieving the perfect anisotropy (90º) was a 25% of O_2 in SF_6-O_2 gas mixture, 80 mTorr and at the substrate temperature of 15ºC. By comparison in my results, the perfect anisotropic was achieved using 20% of O_2 in SF_6-O_2 gas mixture, but differences in other parameters also need to be considered.

Other factors of reactive ion etching were investigated by Zou[131]. They examined the anisotropy of Si via reactive ion etching, with a SF_6-O_2 gas mixture. The author considered the effect of O_2 content and pressure on the etching process. Moreover, the author explained that the system pressure strongly influenced the etch rate.

Legtenberg *et al.*[132] made comparable studies on Si using SF_6-O_2-CHF_3 gas mixtures. Normally, dry etching of Si using SF_6-O_2 gas mixtures produces a rough etch surface, but these authors found that adding CHF_3 gas to the SF_6-O_2 gas mixtures can smooth the etch surface.

The Ge etching process was examined by Shim *et al.*[133]. They investigated the characteristics of Ge dry etching by using an SF_6 plasma. For pure SF_6, the side wall profile is isotropic. The etch rate and the etch profile were presented as a function of the SF_6 flow rate, power and working pressure. The results showed that the etch rate is proportional to SF_6 flow rate and power. In contrast, the etch rate was inversely proportional to the working pressure.

Important work by Campo *et al.*[134], of particular relevance to this study, examined the etching process of Ge alongside that of Si. The effect of O_2 content ($\%O_2$) in the SF_6-O_2 gas mixtures on dry etching of Si and Ge was investigated. They presented their model for the etching process that Fluorine atoms are the active etchant to explain their results. The etch rate of both Si and Ge had a similar behaviour, but the Si etch rate was greater than the Ge etch rate until the O_2 content reached above 50% in the SF_6-O_2 gas mixture. The etch rate results were supported by using mass spectroscopy and optical emission spectrometry measurements via the fluorine consumption, fluorine concentration, and oxygen concentration. In addition, the evolution of SiF_3^+ and GeF_3^+ agreed with the etch rate. Moreover, surface analysis monitored by XPS measurement also indicated the formation of surface layers of SiO_xF_y and GeO_xF_y.

Another technique for dry etching process is reactive ion beam etching (RIBE). Korzec *et al.*[135] examined the dry etching of SF_6-O_2 gas mixture via reactive ion beam etching (RIBE) for Si and SiO_2. Their characteristic Si etch rate was the same as for the results presented in this thesis. Moreover, they found that the etch anisotropy can be enhanced when the etching process is made at lower pressure and with a higher oxygen fraction in the SF_6-O_2 gas mixture, which also supports my results.

Recent work in 2013 by Liu *et al.*[136] considered SF_6-O_2 plasma etching on silicon at low temperature (1K), cryogenic plasma etching. When the temperature was decreased, the

etching indicated more anisotropy. To obtain good anisotropic etching, a low percentage of O_2 is required at low temperatures. For optimal results, many parameters involved in the etching process need to be considered such as temperature, gas composition ratio, forward bias power, ICP power and pressure. These factors are almost the same factors that are considered for RIE except temperature. RIE might be more convenient than cryogenic plasma etching because RIE can be perfectly anisotropic without having to worry about temperature.

4.2 Wafer growth and trench etching procedure

In this experiment, Ge and Ge:P layers were grown onto 100 mm diameter, low-doped (1-10 Ω-cm) Si(001) substrates. Growth was performed by reduced pressure chemical vapour deposition (RP-CVD) in an ASM Epsilon 2000 reactor using germane (GeH_4) as a precursor gas, where the specific growth properties and material properties of these layers have been previously reported[100]. Two different phosphorous doping concentrations of the final Ge layer were investigated: $1x10^{18}$ cm^{-3} (herein referred to as "lightly doped", Ge:P[L]) and a $3x10^{19}$ cm^{-3} (referred to as "heavily doped", Ge:P[H] respectively. The schematics of samples are presented in Figure 4.1.

The investigation was performed on small (7x7 mm^2) pieces of the grown wafers where photolithography was performed using a 1.8µm S1813 photoresist, a Karl Suss MJB4 mask aligner and MF-319 developer to create mesas of photoresist of width 8µm, 8µm spacing, and 2 mm long, aligned along the <1 1 0> direction. Samples were cleaned by deionized water and then dried with nitrogen.

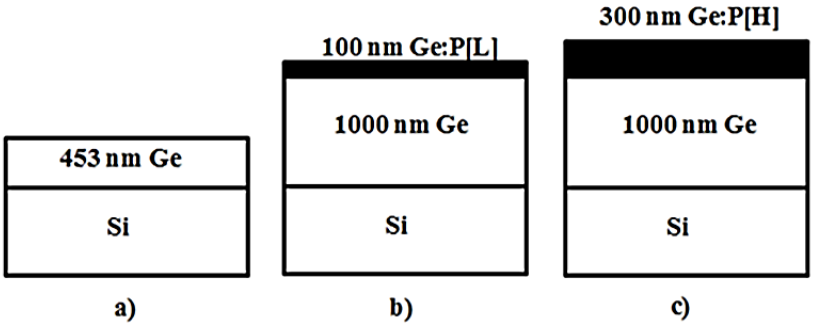

Figure 4.1: The schematics of samples : a) Ge (undoped layer) b) Ge:P[L] ($1x10^{18}$ cm^{-3}) c) Ge:P[H] ($3x10^{19}$ cm^{-3})

The apparatus for dry etching used in this work was a Corial 200 IL reactive ion etcher operating at a frequency of 13.6 MHz and using gas sources of SF_6(99.999%), O_2(99.9995%) and He(99.999%) as a temperature controlled gas to a handle wafer, upon which the sample was placed. All fabrication equipment used was housed and operated in a class 100 clean room. The RIE process parameters were: working pressure of 20 mTorr, RF power 100 W and total gas flow of 30 sccm. A cooling system was used to keep the handle wafer at a constant temperature of 20°C throughout the etch process.

Surface steps were measured using an Ambios XP-100 step-profilometer. After RIE the mesa height was measured post-resist removal, an example of which is shown in Figure 4.2. The mesa step without resist measured the vertical amount of material removed and in conjunction with the etch time this determining the etch rate. To investigate the results of anisotropy, samples were then cleaved along <1 1 0> directions across the mesas, so that their cross-sections could be examined by scanning electron microscopy (SEM) using an accelerating voltage of 5 kV.

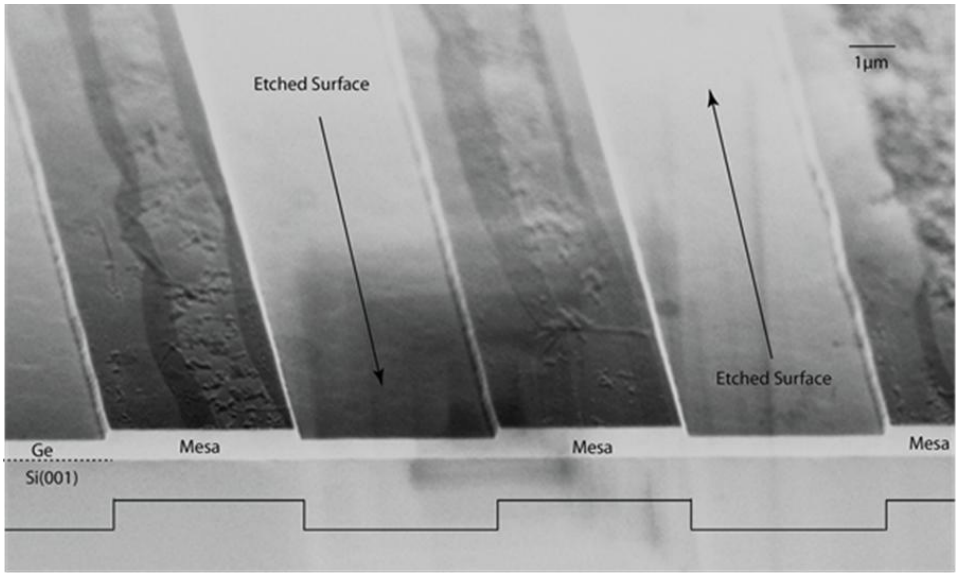

Figure 4.2: The Ge mesa pattern using RIE, removed photoresist (PR), still have residual PR on top of mesa

4.3 Etch rate

Figure 4.3 shows the measured etch rates versus O_2 content (%O_2) - the measurement data are presented in appendix A. A sharp rise in etch rate for all samples is observed when O_2 is introduced into SF_6 up to 5% O_2, followed by a fall as O_2 dilution is increased beyond this value. Specifically, the Si etch rate etch rate decreases linearly as %O_2 increases from 5% to 50%, and then has a slow linear reduction up to 90%. Ge and Ge:P etch rates rapidly decline as %O_2 increases to 20%, above which the etch rate levels off and remains roughly constant up to 70%O_2, approaching zero at 90%. The effect of doping level upon the etch rate is more significant at lower O_2% where the etch rate of the lighter doped Ge:P[L] is higher than the intrinsic Ge (i-Ge), which are both higher than that of heavily doped Ge:P[H]. Where O_2 > 20%, the etch rate of all types of Ge samples are similar and does not show any differences. Overall the O_2 content has a larger influence on etch rate compared to doping level when O_2 content is more than 20%, whereas doping effects are more prevalent with O_2 content below 20%.

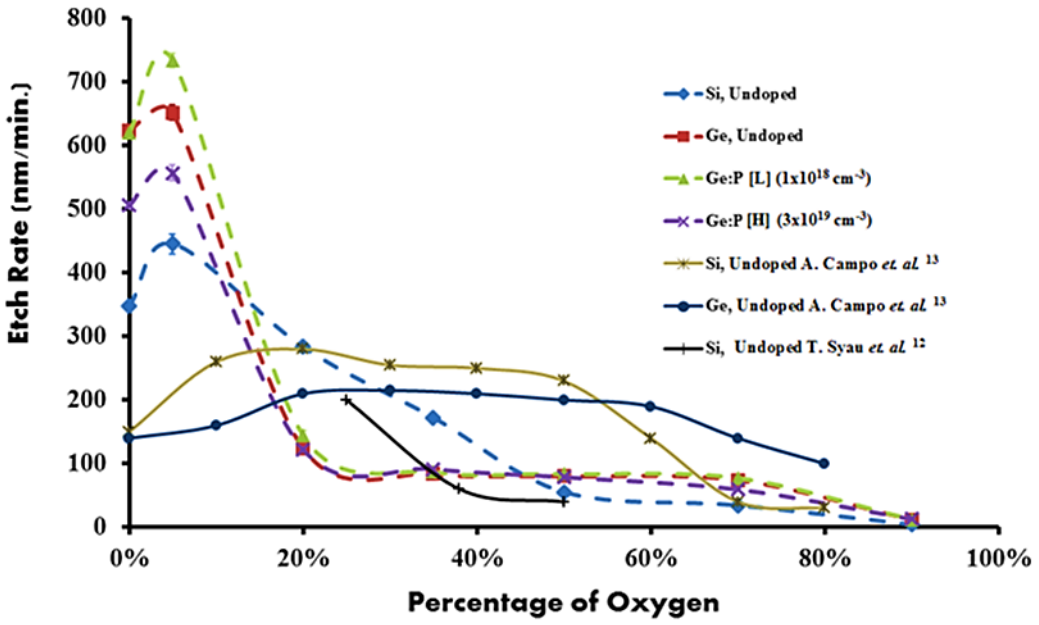

Figure 4.3: RIE etch rates of Si and Ge as a function of percentage of O_2 in the SF_6-O_2

Lee and Chen[137] concluded that doping level does not affect physical etching, but can influence plasma etching. We can assume that the etching mechanism of Ge:P[L] can be explained by a charge transfer mechanism[138]. For an n-type semiconductor, an electron from the conduction band tunnels through the potential barrier at the surface and reaches the chemisorbed F atom. The F atom is thus negatively charged to form a surface dipole involving the ionized donor atoms (P) in Ge, giving a higher etch rate[139]. We suggest that the lower etch rates as seen in the more highly doped Ge could be a result of the suppression of the tunnelling process, due to the potential fluctuations of the band edges (band tailing), which occurs at higher n-doping concentrations.

For Si, our results are comparable with Syau *et al.* who used the same total pressure, albeit over a limited O_2% range and a higher RF power of 200W. The Si etch rate of Syau *et al.* shows lower than our experiment. As a result of the increasing power causes the fraction light ions in plasma increase. It means that the physical sputtering is decreased[135]. In contrast

to our findings, Campo *et al.* found that etch rate maxima when introducing O_2 into an SF_6 mixture occurs at 20% O_2. At 20% O_2, our Si etch rate is 3 times faster than Ge, verging on the criteria of reasonable selective etching which is not seen in Campo *et al.*'s work. However, we both find a similar trend in the silicon etch rate, which drops significantly beyond 50% O_2, allowing the etch to be selective to Ge beyond that. However, comparison with Campo *et al.* is complicated because our etching parameters are different in at least two important respects: the total gas pressure used for our work is 1/5 of that used by Campo *et al.* and our power is twice as large, both of which impact the dynamics of the etching process. This suggests that the mechanism that occurs at that point (≤ 20% O_2) is mostly chemical (plasma etching) as opposed to physical etching.

When a few percent of O_2 is added to SF_6 (up to 5%), the concentration of the etchant species (F radicals, F*) increases causing an increase in the etch rates of Si for low $\%O_2$, because the O_2 in the plasma reduces SF_x/F recombination rates[134]. The maximum etch rate attained in this work occurs at the lowest O_2 examined at $\%O_2$ = 5% whereas Campo *et al.* find a maximum etch rate at $\%O_2$ = 20%, where we observe etch rates 2 to 3 times larger due to the larger power used in our work. Above 5% of O_2, etch rates decrease because O atoms increasingly compete with F* for occupancy of active sites on the surface, we observe a faster decline in etch rates with lower overall values compared to Campo *et al*. due to our lower working pressure. In the range of 5% - 20% of O_2, etch rates of all Ge samples dramatically decline, whereas Si etch rates decrease at a lower gradient. This effect can be explained by the superficial layers of SiO_xF_y and GeO_xF_y that form on the surfaces impeding chemical etching[140], with the Ge-O bond (3.66eV) breaking more readily than the Si-O bond (4.82eV)[14]. Below 5% O_2, we postulate that the concentrations of SiO_xF_y and GeO_xF_y are not high enough to affect the etch rates.

4.4 Sidewall profile

Definitions for the etch sidewall profile and the associated measured angle[130] are shown in Figure 4.4. The angle of sidewall profile was represented by the angle $A\hat{B}C$. With this definition, isotropic etching is at $A\hat{B}C$ below 90º, perfect anisotropy etching is at $A\hat{B}C$ equal to 90º and partially anisotropic is at $A\hat{B}C$ more than 90º. The measurement data are presented in Appendix B. The samples are patterned in the <110> directions and are cleaved using standard cleaving techniques perpendicular to the mesa direction. The etched mesas are analyzed by SEM and anisotropic etching is evident for all samples, where images of the sidewalls are shown in Figure 4.5 – 4.8 and are presented graphically in Figure 4.9. When the Si and Ge sidewall angles are compared, it is observed that there is no significant difference. The perfect anisotropic mesa where θ=90° is achieved with $\%O_2$ = 20% by approximately. The value of $\%O_2$ = 20 is the critical concentration beyond which the angle changes from acute to obtuse. These observations are consistent with a transition between plasma-to-sputter-dominated etching, the isotropic profile being caused by plasma etching and anisotropic profile through physical etchting[140].

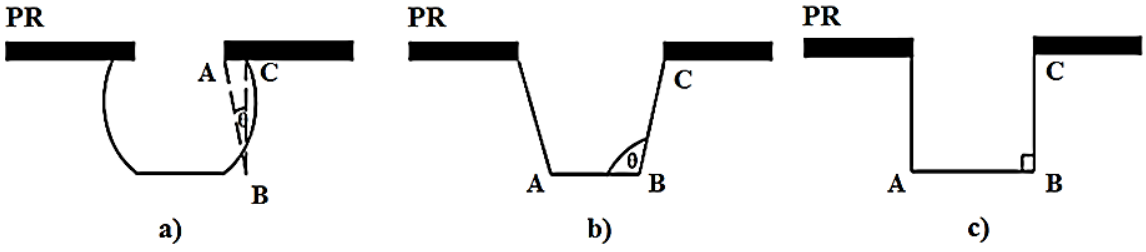

Figure 4.4: Mesa profiles produced by anisotropic and isotropic etching (PR = photoresist) :

a) Isotropic b) Partially Anisotropic c) Perfect Anisotropy

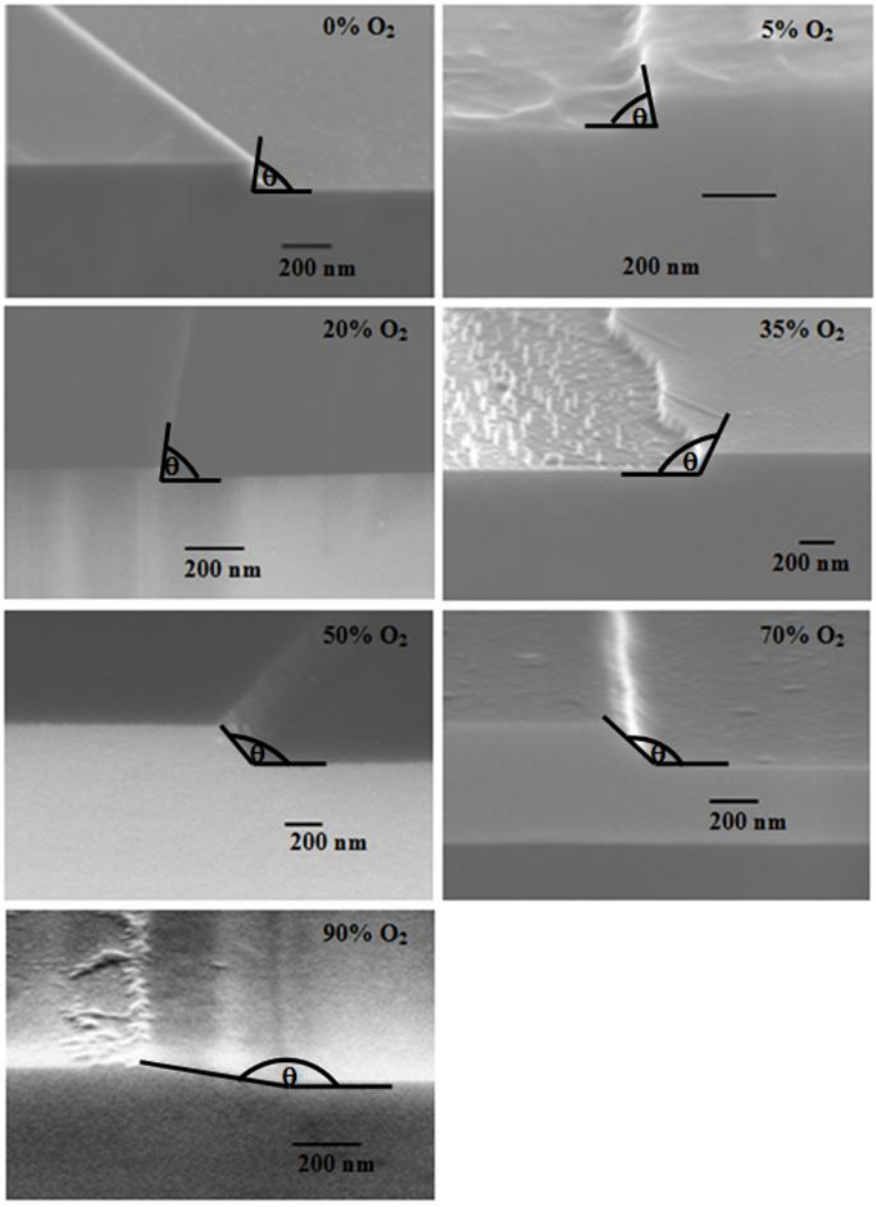

Figure 4.5: SEM images of the surface morphology of Si mesa after dry etching with SF_6-O_2 of various O_2 percentages

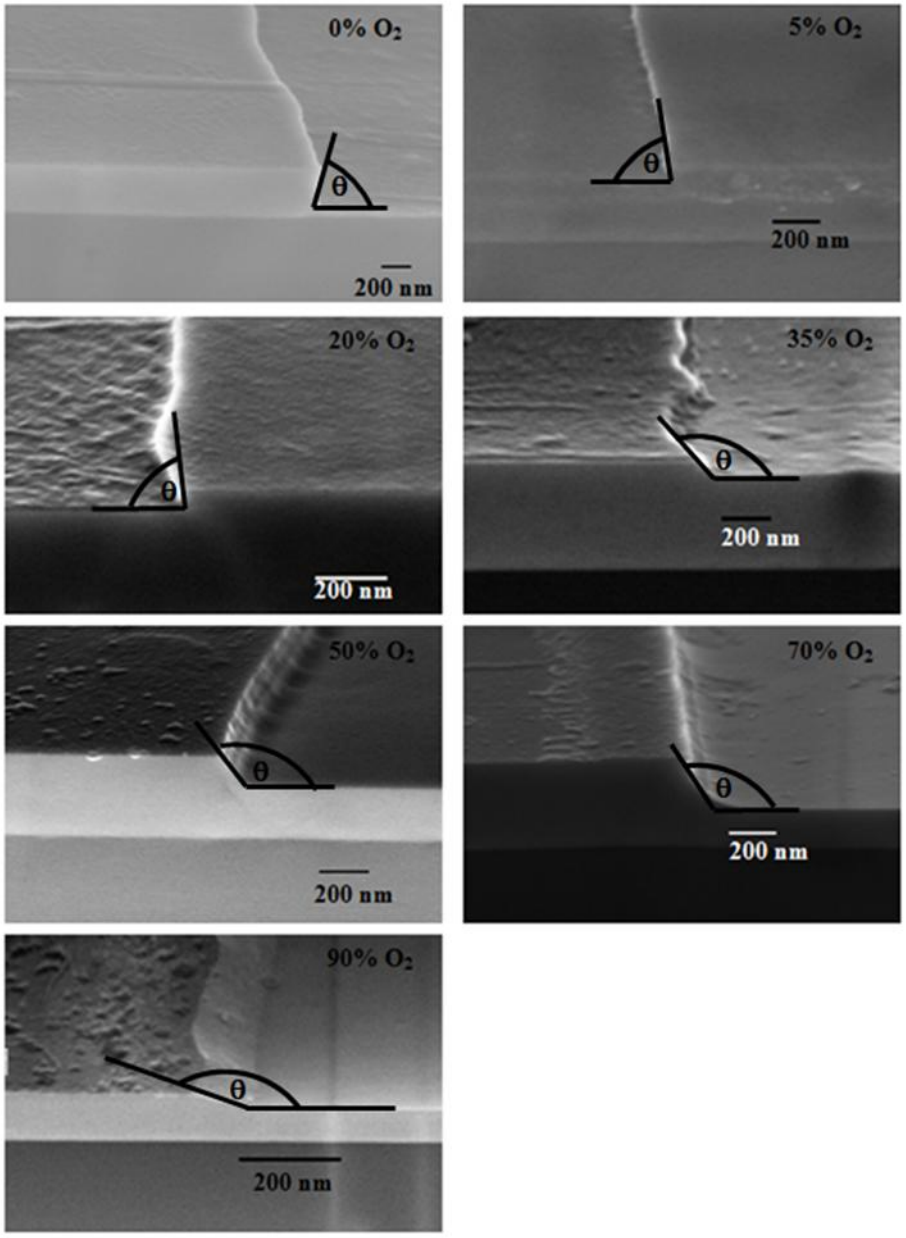

Figure 4.6: SEM images of the surface morphology of Germanium (intrinsic) mesa after dry etching with SF_6-O_2 of various O_2 percentages

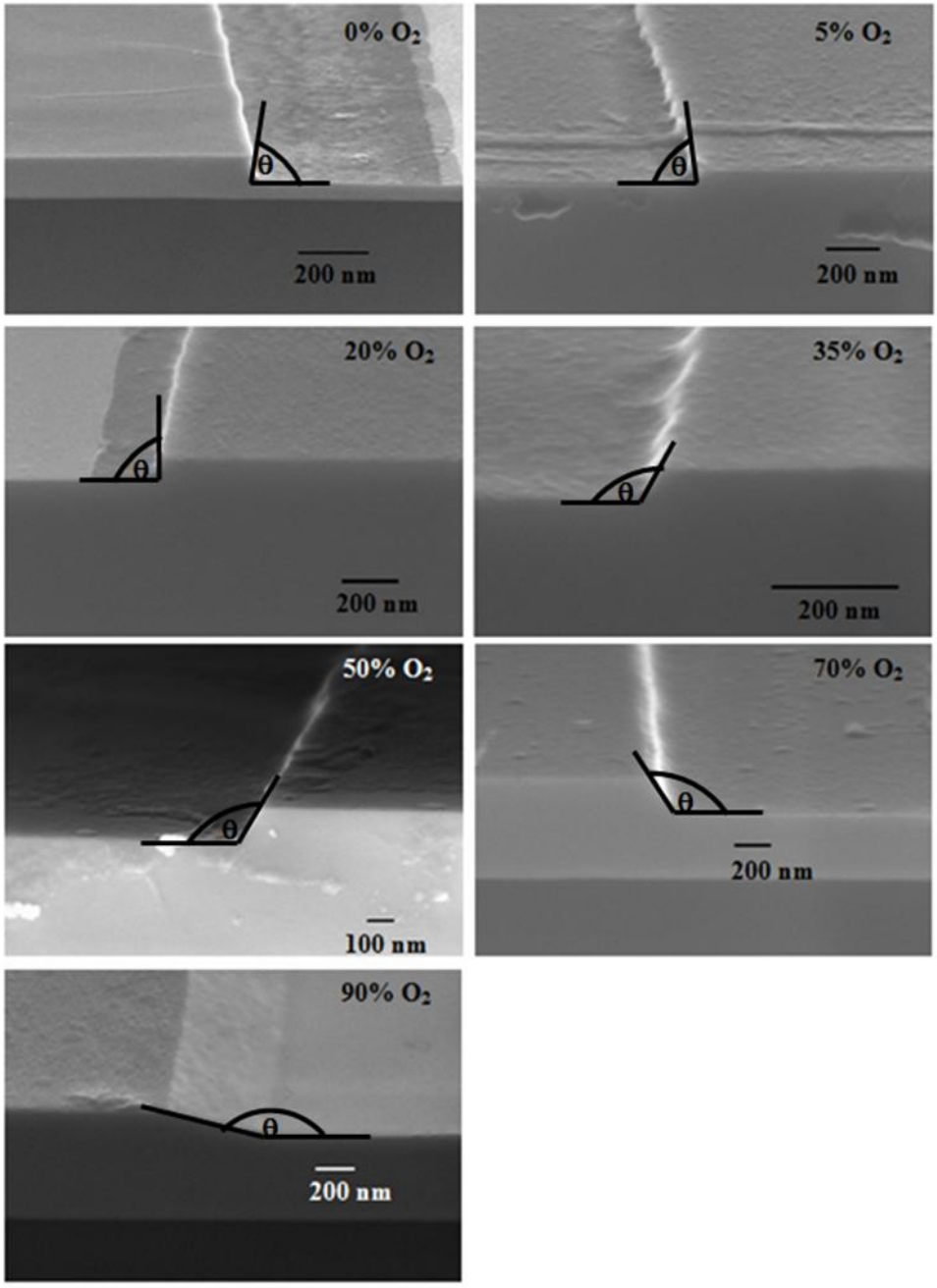

Figure 4.7: SEM images of the surface morphology of lightly doped germanium ($1x10^{18}$ cm^{-3}) mesa after dry etching with SF_6-O_2 of various O_2 percentages

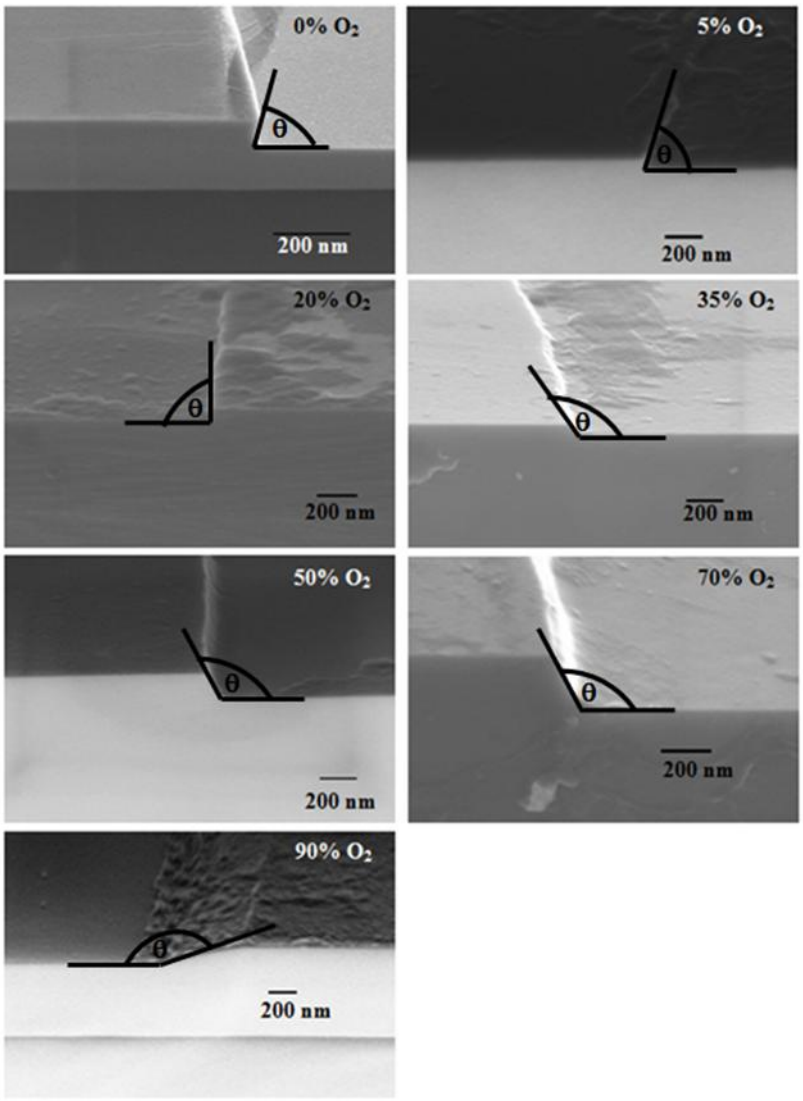

Figure 4.8: SEM images of the surface morphology of heavily doped germanium ($3x10^{19}$ cm^{-3}) mesa after dry etching with SF_6-O_2 of various O_2 percentages

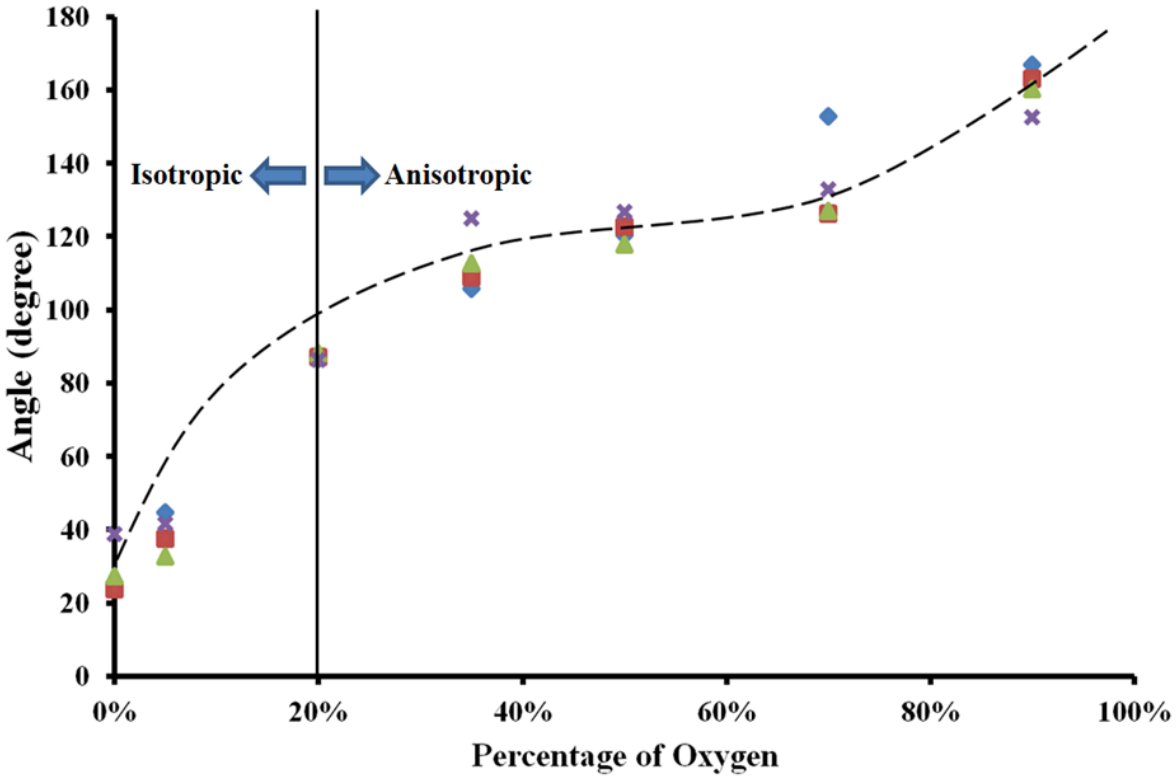

Figure 4.9: The anisotropic angle as a function of percentage of oxygen, dash line is eye guide line

With O_2 content < 20% the results show evidence of isotropic etching with $\theta \leq 90°$. It is known that if materials are etched by using pure SF_6 the resulting sidewall is perfectly isotropic[105]. With increasing O_2%, plasma etching is suppressed and physical etching becomes more prominent, ultimately yielding a maximum sidewall angle of 166° to the surface. Since the threshold for reduction of etch rate and the critical concentration for etching angle coincides at a $\%O_2$ of 20%, we propose that the mechanism is due to sidewall oxide formation at higher $\%O_2$ and re-deposition of SiO_xF_y and GeO_xF_y etched products, which have been reported to help in promoting an anisotropic etch profile[140]. When the O_2 concentration is below 20% the oxides are not so prevalent. F* created in the plasma are absorbed in the etched surface and move until they reach a lowest potential energy sites at

bottom of the mesa, causing lateral etching of the mesa. When the O_2 content is above 20% O^+ ions are increasingly absorbed in the etched surface. This creates SiO_2 or GeO_2 on the sidewall, effectively impeding chemical etching. Then physical sputtering tends to be dominant and some of sputtering products redeposit on the sidewall, creating a partial anisotropic profile. This process is depicted in Figure 4.7.

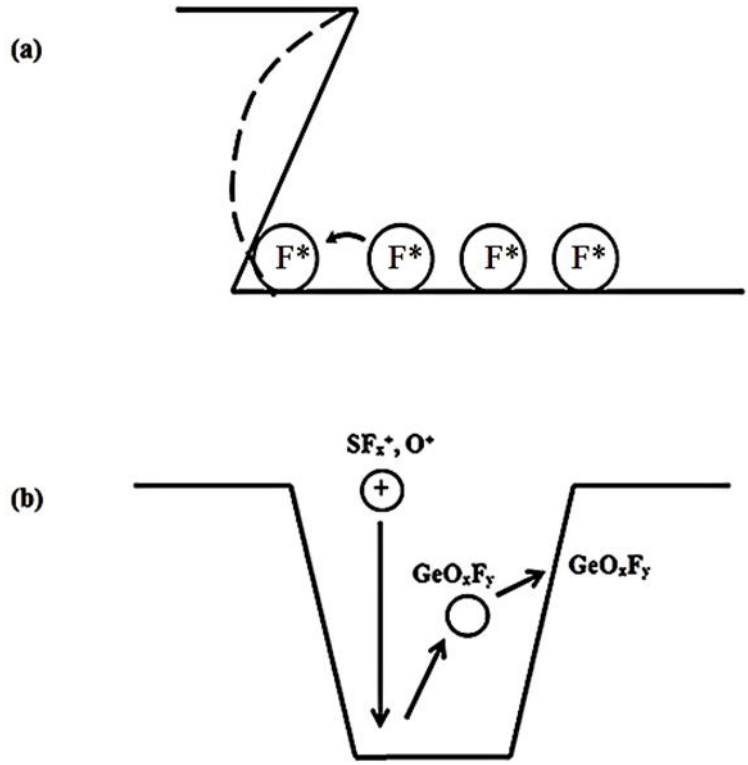

Figure 4.10: The proposed etch mechanism, (a) the F* find the site of least potential energy, the step and therefore etch slightly laterally. (b) GeO_xF_y is sputtered from the bottom surface and redeposited onto the sidewall

4.5 Conclusion

Reactive ion etching (RIE) of Si, Ge and Ge:P has been studied, using a SF_6-O_2 gas mixture. The experiments found that the O_2 content in the total gas (SF_6-O_2) flow effected in the etch rate and sidewall profile. Furthermore, RIE is the combination of chemical and physical etching mechanism. Then the characteristics of sidewall profile were influenced by chemical and physical etching as shown in Figure 4.5 to Figure 4.8.

The etch rate rises sharply as small amounts of O_2 (up to 5%) are added to a pure SF_6 etch and then decreases when O_2 content is increased. The etch rate of Ge and Ge:P is significantly increased over Si for O_2 content in the ranges 0% to 12% and > 46%, indicating that well controlled selective etching is achievable simply by varying O_2 flow rates. Perfectly perpendicular sidewalls are also clearly evident close to 20% O_2 content, again allowing excellent etching control. In summary, adding O_2 to SF_6 for RIE applications enables significant advantageous and well controllable variations in the process. In addition, the previous work shows that the etch rate is proportional to the doping level. However, this research found that the etch rate was reduced if the doping level was increased.

The O_2 content also influences the sidewall profile. At low O_2 content (< 20%), the sidewall profile is isotropic, which is because the chemical etching mechanism is the dominant process as a result of the more etchant (F*) due to the anti-recombination by oxygen atom. When O_2 content is equal to 20%, the sidewall profile can form the perfect anisotropic. At high O_2 content (> 20%), the physical etching mechanism is the prevailing process. Then, the sidewall profile is anisotropic. The high oxygen atom concentration causes the increasing of physical etching via sputtering process.

5 Creation of Suspended Ge Structure

5.1 Introduction

Nowadays, many researchers are putting in a huge effort to develop a range of micromechanical system (MEMS) as the technology for devices and structures at the nano scale. One of the methods to improve MEMS is to use suspended structures. The suspended structures can be fabricated to have thermal and electrical properties that are different from their substrate. The advantages of suspended structures can be found in such devices as comb device[142,143], micromirrors[142], resonant chemical sensor[143] and high-Q solenoids[144].

An enormous literature exists on the MEMS development of suspended structures from a variety of materials. As the research in this thesis is motivated by the desire to create effective electronic cooling platforms, we start by considering a Si_3N_4 membrane for mounting transition edge sensor (TES) presented by the Aalto group[11]. This Si_3N_4 membrane was isolated from the thermal bath by four thin bridges. The temperature of the platform was reduced from 200 mK to 100 mK. Subsequently, NIST[145] fabricated Si_3N_4 membranes for X-ray detectors that can be cooled from 300 mK to 190 mK. Due to the fragility of the Si_3N_4 membranes, a porous Si membrane was proposed. It has been implanted on a bulk Si platform in Si thermal sensors[146]. The porous Si is fabricated from bulk crystalline Si by electrochemical dissolution. However, for a given strength, a porous Si membrane is thicker than a crystalline membrane, i.e. the porous Si membrane has more thermal mass than a crystalline membrane. Otherwise, crystalline membranes can be used for the same mechanical strength as the porous Si membrane. Then the crystalline membrane can take over. The fabrication and properties of a Ge crystalline membrane is considered in this thesis.

By fabricating a Ge membrane it is also possible to make structures with improved electrical properties. This chapter describes one such application. One disadvantage of using

epitaxial Ge on Si(001) for electronic and thermoelectric devices is the electrical leakage because of dislocations. It means that the structure can conduct. The conductivity of the membrane can lead to a short circuit when a device is mounted on the membrane, either to ground or between devices. Proposed models for the origin of dislocation produced conductivity in membranes are :

1. The core of a dislocation is very conducting and acts like a wire in material[147].

2. The dislocation modifies the band structure by creating extended states in the semiconductor bandgap at which the minority carriers can be trapped[148].

An investigation was performed using a suspended structure of Ge to solve the problem due to dislocations. For a suspended structure, the surface-to-surface conduction can be prevented because the misfit interface was removed as shown in Figure 6.1. In this work, the investigated suspended structures are membrane, spiderweb and van der Pauw cross on Ge.

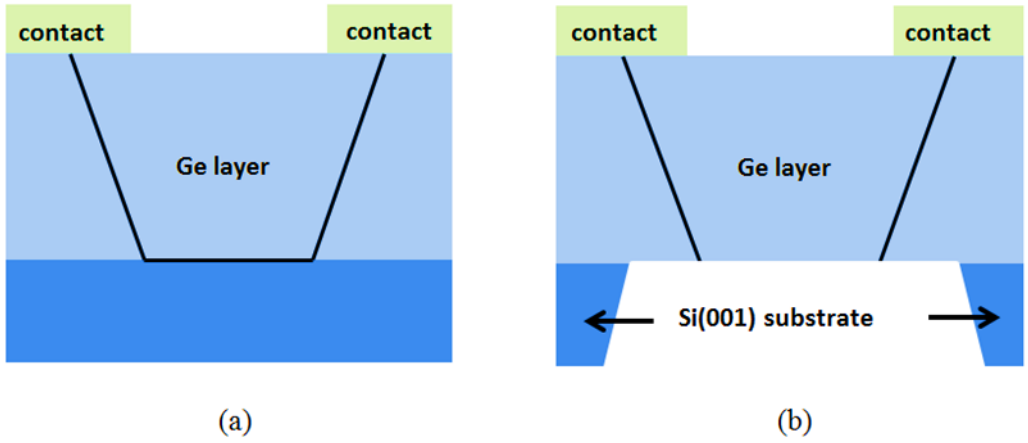

Figure 5.1: (a) dislocation(black line) acts like a wire to connect contacts, leading to electrical leakage (b) suspended structure can remove part of dislocation, and remove the leakage path

5.2 Sample fabrication

The techniques described previously in Chapter 3 were employed to fabricate suspended structures, i.e. photolithography, dry etching and wet etching. The type of dry etching that was used in this experiment is reactive ion etching, RIE (Chapter 4).

5.2.1 Photolithography

The mesa patterns were produced by photolithography. In order to fabricate a mesa pattern an optimal time to expose the sample is required. Figure 5.2 shows optical images of the smallest mesa pattern with 2 μm features obtained by exposing the sample for different times. As shown in Figure 5.2 (a), the 2 μm mesas patterned on the wafer can be obtained properly with 3s of exposure time. On the other hand, if the exposing time was less or more than 3 s, 2 μm mesas cannot be successfully fabricated on the wafer sample, as seen in Figure 6.2 (b) showing an optical image of pattern obtained by 4 s of exposing time. It can be concluded that the pattern with the smallest 2 μm mesa can be only obtained by exposing sample with an optimal time of 3 s.

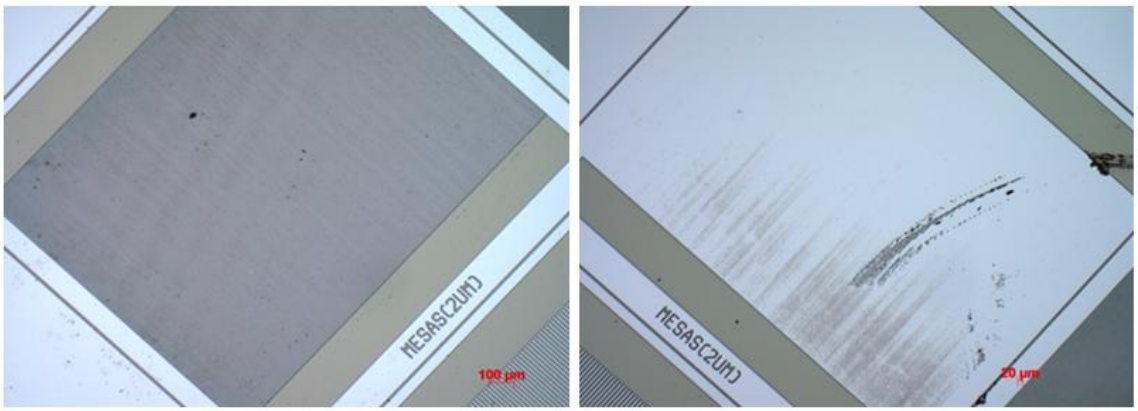

a) b)

Figure 5.2: The smallest 2μm mesa pattern

a) 3 seconds of the expose time b) 4 seconds of the expose time

5.2.2 Wet etching

TMAH (tetramethylammonium hydroxide) has been widely used for wet etching of Si because it is nontoxic, good anisotropic etching characteristic, smooth surface. Furthermore, TMAH is easily to control and etch rate is constant over a long etch time. In this research, TMAH(25wt%, 80°C)[149] was used to make the suspended structures. The observation of TMAH etching found that the etch rate is 0.5 μm/min. The test of backside fabrication is shown in Figure 5.3. From Figure 5.3, it was found that the surface of the top-side is smooth. The membranes were found to be under a slight tensile strain.

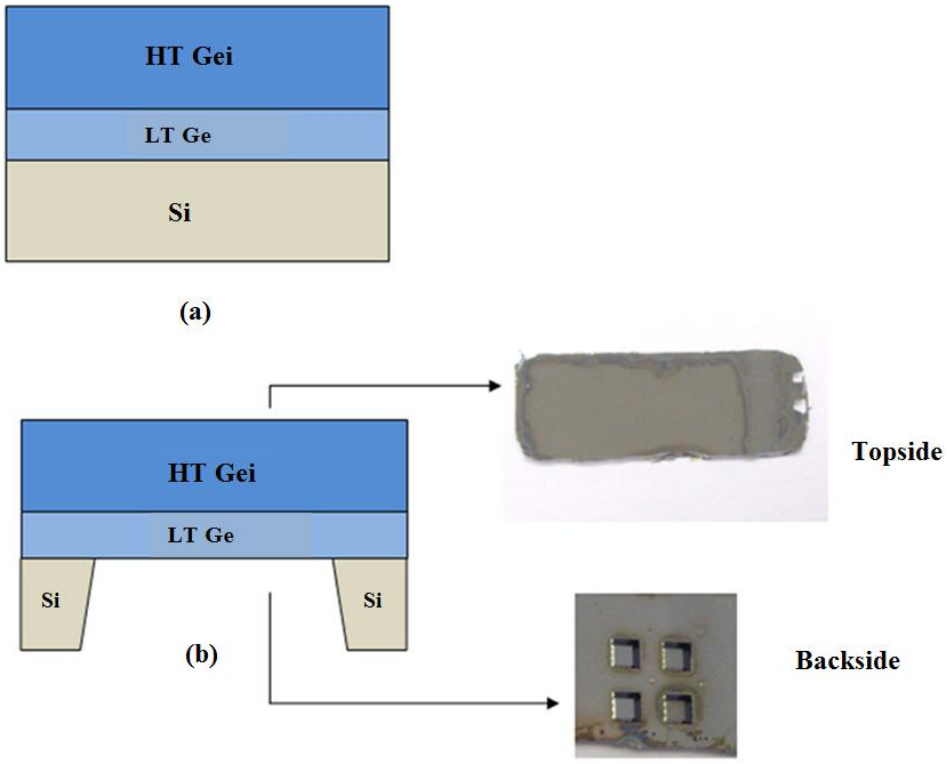

Figure 5.3: a) Ge on Si wafer b) topside and back side of Ge membrane

Fabrication procedures were performed as follows:

1. Photolithography

- A primer and a S1818 photoresist were spun over a sample by using Spin Coater.
- Mask Aligner operated at 300 W was employed to expose a sample with optimal time.
- Exposed sample was developed with MF 319 about 1 min.
- Finally, sample was cleaned by deionised water and then was dried with nitrogen.

2. Dry etching

- The samples(mesa pattern) were fabricated by photolithography
- The samples were loaded in the Corial 200 IL
- Corial 200 IL was operated at 20 mTorr, total gas flow 30 sccm, rf power 20 W using a mix of SF_6 and O_2
- The etching time was varied, dependent upon the type of sample and etch rate
- The thickness of sample was measured by step-profilometer (Ambios XP-100) before and after etching process
- The cross-section of samples was examined by SEM

3. Wet etching

- A solution of 25 wt% tetramethylammonium hydroxide (TMAH) was heated up to 85°C then etching time was varied dependent upon the type of sample and etch rate
- An entire sample was horizontally immersed into TMAH solution with different time, dependent upon the type of wafer and etch rate.
- Then, sample was cleaned with deionised water and isopropanol (IPA).
- Finally, sample was left to dry under vacuum at room temperature.

5.3 Results and discussion

Details will be presented of a range of structures that have been fabricated, starting with a long narrow bridge or micro-wire.

5.3.1 Suspended micro wire

The Figure 5.4 shows a suspended micro wire structure (2, 4, 8 and 16 μm width) that was fabricated by using the technique described in section 5.2. Figure 5.4 (a) shows the initial wafer that consists of a two-temperature Ge bilayer grown epitaxially on top of a low-resistivity (10-25 Ω cm), 300μm thick 4″ Si(001) by reduced-pressure chemical vapour deposition (RP-CVD). This bilayer is comprised of a 100 nm thick low temperature Ge layer (LG) and a 900 nm thick high temperature Ge layer (HG) on top of LG. Figure 6.4 (b) shows that the micro wire can be held suspended by the tension that remains in the Ge layer from the growth process: The Ge layer was fully relaxed at the growth temperature (of 600ºC), but it acquires tension on cooling down to room temperature because the thermal expansion coefficient is greater than for silicon, which constitutes the much thicker substrate[150]. Otherwise, if the Ge bridge is not under tension, the micro wire will fall down as shown in Figure 5.4 (c).

The etch rate of TMAH depends on the crystal plane[151] and is slowest on {111}. Consequently, material can remain underneath the bridge after etching by TMAH. To solve this problem, it was found that the samples should be rotated by 45° as shown in Figure 5.5 so that the micro wires were along the (100) direction, instead of the (110) direction. It means that the (111) could not be etched directly underneath the micro wire during TMAH etching and fast etching will occur in all directions. The completed and uncompleted suspended micro wire present in Figure 5.6.

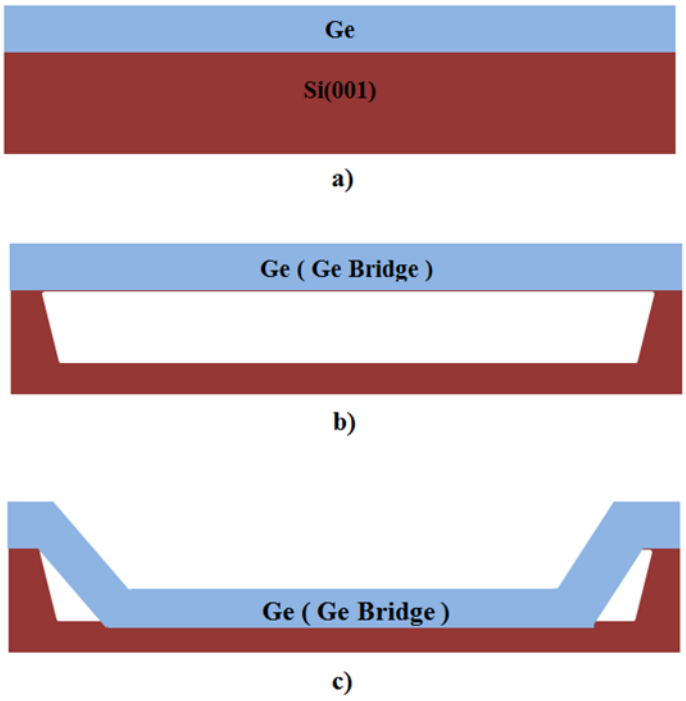

Figure 5.4: (a) The initial structures (b) The suspended micro wire (c) micro wire attached to the substrate surface due to a lack of tension

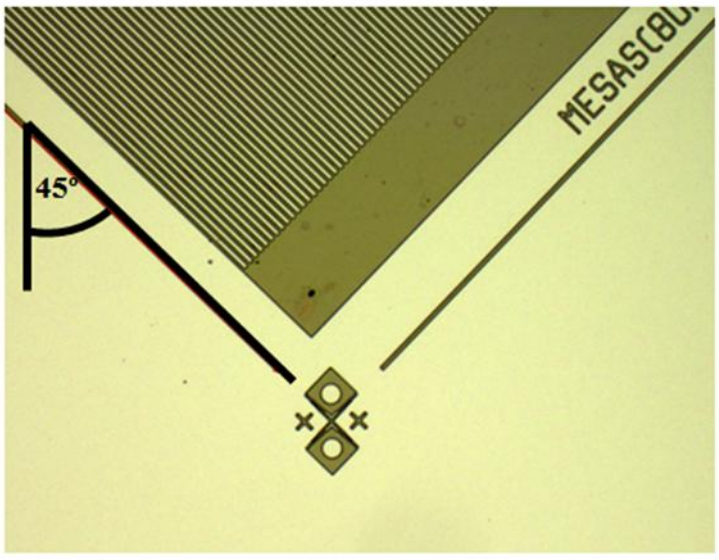

Figure 5.5: The micro wire pattern is tiled by 45º to lie along the (100) direction

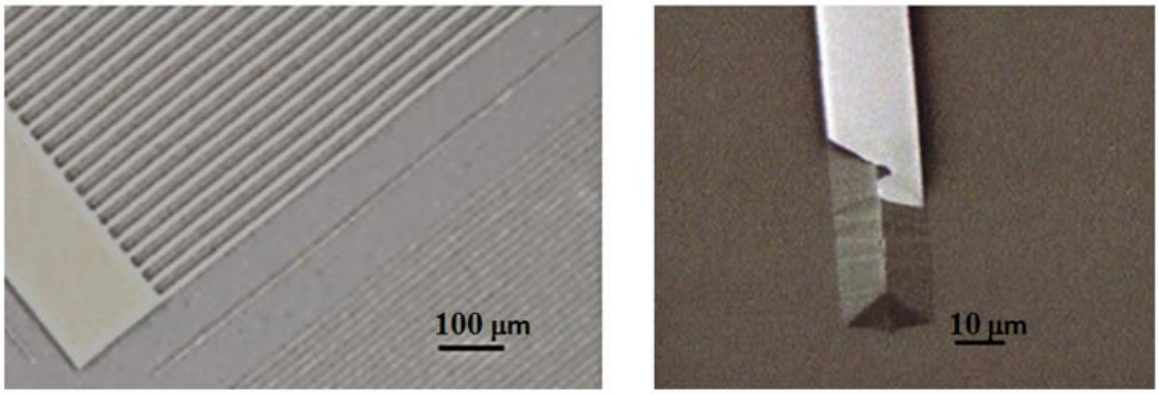

Figure 5.6: (a) The completed micro wire (b) uncompleted micro wire that presents the underneath slowest etching plane

The etch rate of TMAH depends on the crystal plane[151] and is slowest on {111}. Consequently, material can remain underneath the bridge after etching by TMAH. To solve this problem, it was found that the samples should be rotated by 45° as shown in Figure 5.5 so that the micro wires were along the (100) direction, instead of the (110) direction. It means that the (111) could not be etched directly underneath the micro wire during TMAH etching and fast etching will occur in all directions. The completed and uncompleted suspended micro wire are shown in Figure 5.6.

5.3.2 The suspended spiderweb

The suspended spiderweb is the ideal platform for bolometers. The spiderweb bolometer has several advantages. It reduces the bolometer's heat capacity, reduces the cosmic-ray cross-section[152]. The spiderweb bolometer also minimizes its microphonic response (the tendency to convert vibrations from equipment movement into electronic noise)[153]. Moreover, the spiderweb structure is much less sensitive to ionizing radiation that conventional bolometers[153]. The bolometer can have higher sensitivity and lower noise power due to lower thermal conductivity[154]. The suspended spider web (1μm Ge layer thickness, 5 μm wide legs, 800 μm x 800 μm overall dimensions) can be fabricated, Figure 5.7 using the

same technique as in section 5.2. To achieve the spiderweb, the thickness and the dimension of the sections of the spiderweb should be considered. If the tensile force is not enough, the spiderweb cannot hold and will become stuck on the substrate surface.

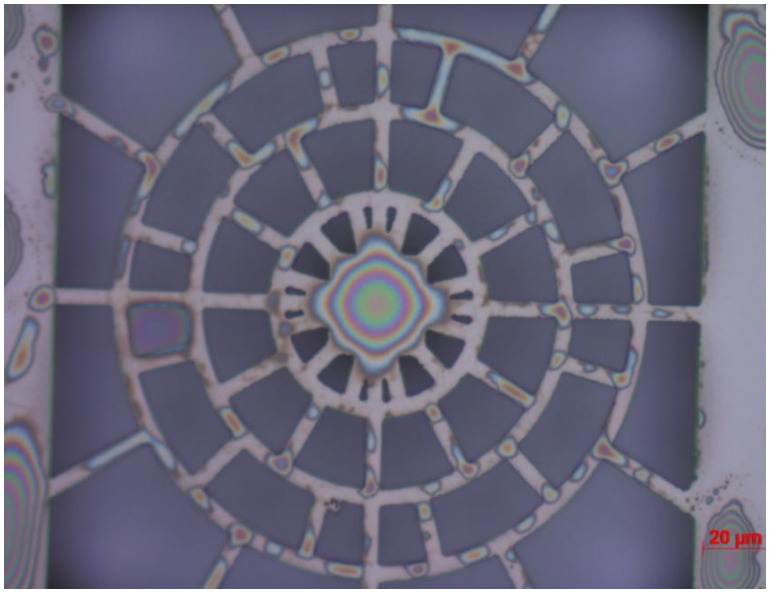

Figure 5.7: The suspended spider web platform is etched by SF_6-O_2 (80%-20%) and TMAH (25wt%, 80°C)

In fabricating these spiderweb structures the issue of the anisotropic etch rate of TMAH presented the same problem as with the micro wire. After etching by TMAH, two bridges remained under the structure, Figure 5.8, because the suspended spider web was patterned along the <110> direction of the Si wafer and the etching rate of TMAH is slowest in {111}. To solve this problem, the experiments found that the design should be rotated by 41º, a slightly different angle from the suspended bridge because of the need to avoid all the arms in the spiderweb design from aligning with the {111} facet of the Si wafer. Another problem found was that the legs of the spiderweb broke due to liquid being trapped when the sample

was removed from the various liquids (such as TMAH, deionised water and isopropanol) during the fabrication process, as shown in Figure 5.9.

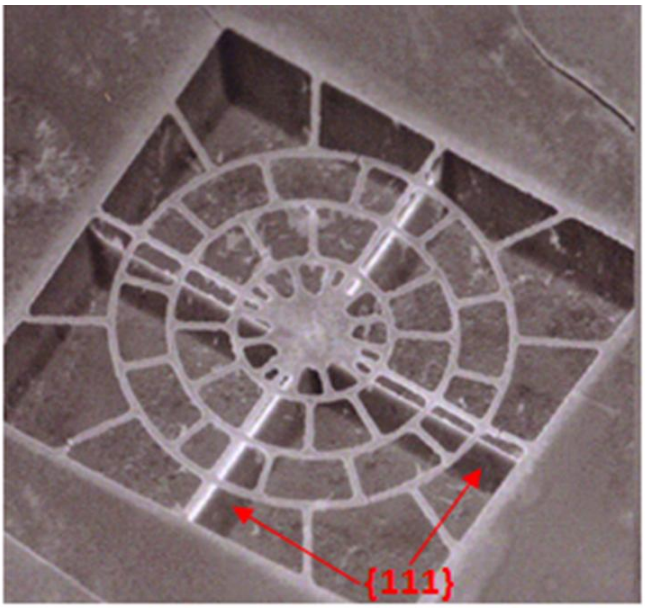

Figure 5.8: The two underneath bridges in {111}

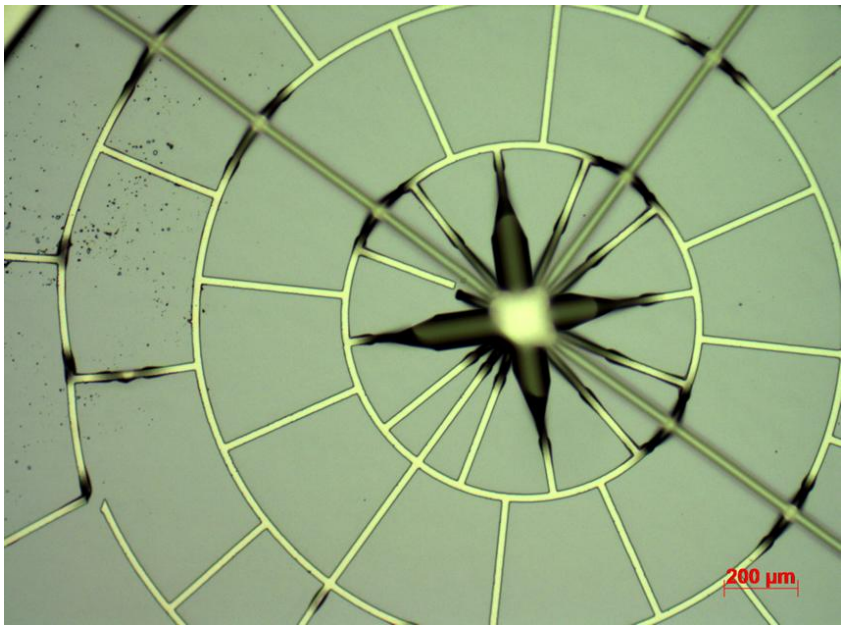

Figure 5.9: Some legs of spiderweb are broken due to liquid trap

5.3.3 The van der Pauw Greek-cross

The van der Pauw Greek-cross structure provides a potential means to investigate the effect of the dislocation network on conductivity in a Ge-on-Si structure, as shown in Figure 5.10, because the sheet resistance is measured in the centre of the cross and not along the entire structure that this benefit is important when the samples are possibly electrically conducting[78]. The van der Pauw Greek-cross structures are fabricated using the same suspended membrane method. Moreover this pattern can use to measure the thermal conductivity[155].

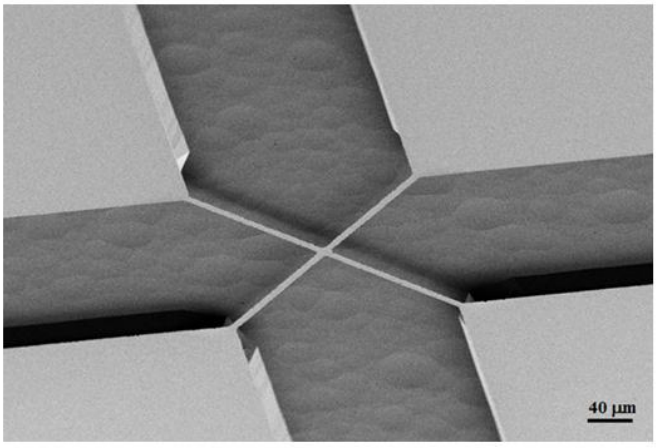

(a)

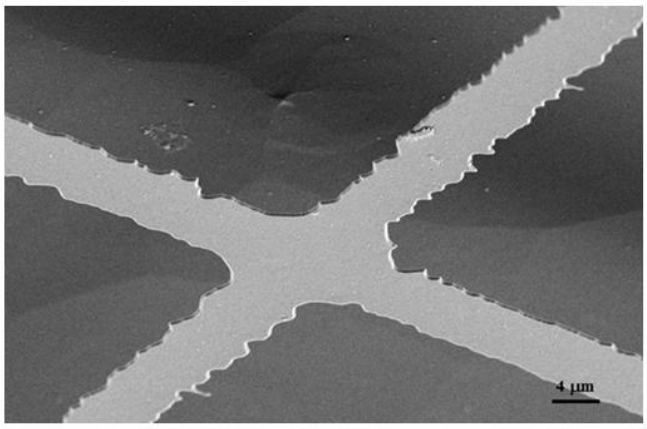

(b)

Figure 5.10: (a) The van der Pauw Greek-cross structure (b) The centre of cross structure

5.3.4 Suspended membrane

Micromachining and nanolithography can provide fascinating devices for cryogenics regime on the micro and nano scale. Advanced applications in, refrigeration, calorimetry and thermometry are using nanostructures that have reduced thermal mass[156]. Many authors point out the need for efficient thermal isolation of a membrane used to mount a bolometer and in microrefrigeration[157]. Nowadays, it is possible to fabricate fully suspended, three-dimensional integrated devices that can be used as bolometers[158]. M. M. Leivo, and J. P. Pekola[156] showed that a suspended membrane cut into the suspended bridge structure can reduce thermal conductance. This research presents the fabrication of the suspended bridged structure and the suspended cross bridge structure by using the fabrication technique outlined in section 5.2

5.3.4.1 Bridged structure

The suspended bridged structure that was fabricated is shown in Figure 5.11. The bridged structure, Figure 5.11 (a), was produced and showed that the 20μm wide legs can be suspended over lengths of 200μm. The device can be deposited within the rectangular window of the structure that provides a suspended region of $200 \times 200\ \mu m^2$.

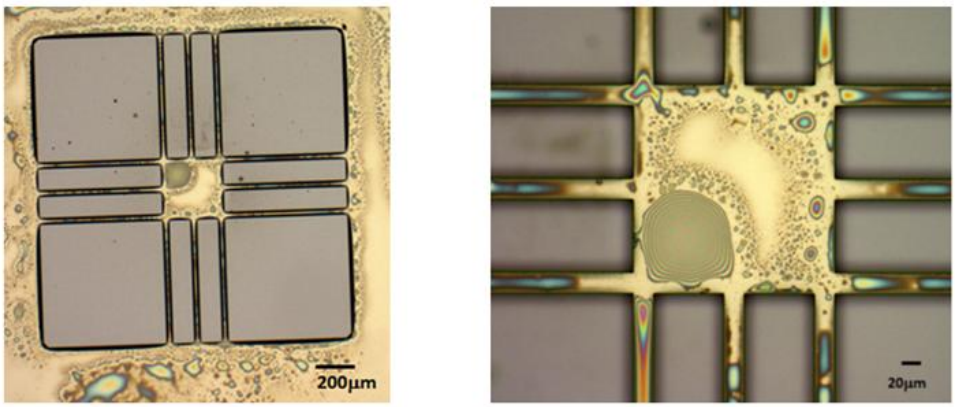

Figure 5.11: (a) The bridged structure, 20μm wide legs (b) Centre of the bridged structure

5.3.4.2 Suspended cross bridge structure

A cross-bridge suspended structure also was fabricated by using the technique (section 5.2) as shown in Figure 5.12. The width of the legs varied from 5μm, 10μm, 20μm to 50μm. The results show that only 5μm wide legs do not have underlying Si pillars that form due to the slow-etching (111) planes meeting. The Si pillar is shown schematically in Figure 5.13.

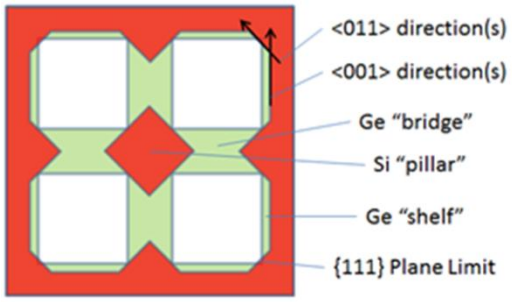

(a)

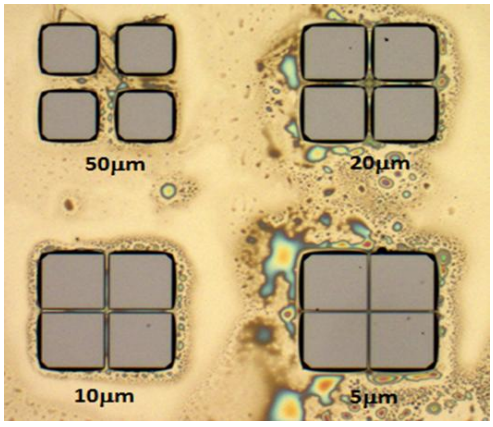

(b)

Figure 5.12: (a) Suspended cross bridge structure diagram (b) The optical images of suspended cross bridge structure

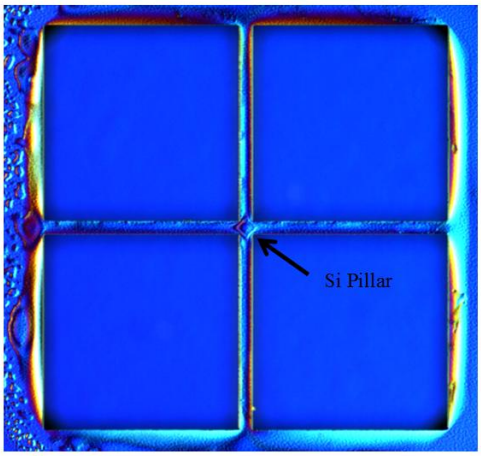

Figure 5.13: The Si pillar

5.3.5 Nanotube

The nanotube has proved a useful structure for fluid transportation and capillarity on the nanometre scale, as well as offering the opportunity to generate the new applications and investigate new physical phenomenon with nanotechnology. Almost any material of thin solid films can form a nanotube and at any position that films can release from their substrate[159].

O. G. Schmidt and K. Eberl[159] presented two methods for making solid-state nanotubes, as shown in Figure 5.14. The first is a so-called general method, (method I). The substrate surface was covered by an etchant-sensitive material. The thin film used to generate the nanotube was then deposited on top of the etchant-sensitive material. After selective etching of the etchant-sensitive material, the thin film was wrapped up and folded back to form a nanotube. The second is a specialized method (method II). A bilayer was deposited on an etchant sensitive material. The bilayer consists of two different materials (materials 1 and 2), where material 1 has a larger lattice constant than material 2. Material 1 is the first layer deposited on an etchant sensitive material followed by material 2. When the bilayer is released from an etchant sensitive material, the bilayer bends upwards to form a nanotube. O.

G. Schmidt and K. Eberl fabricated silicon–germanium nanotubes by using both methods, the elasticity of this material can help in forming the nanotube. The general method can form nanotube as shown in Figure 5.14 c) and d). The Si-Ge nanotube has formed by specialized method as shown in Figure 5.14 e).

In this thesis, nanotubes were produced suspended on a frame by using technique in section 5.2 that correspond with method I. To fabricate a nanotube, a sheet would be integrated on a wire. The wire width varied from 2μm to 10μm, and was 250μm in length while the sheet width varied from 20μm to 50μm, and was 200μm in length as shown in Figure 5.15. The results show that it did not completely undercut sheet size above 30μm because of a Si pillar. Moreover, the 40μm sheet size starts to bend beneath its own weight but it did not completely form nanotube as shown in Figure 5.16. It can be suggest that the sheet should be bigger than 50μm in width.

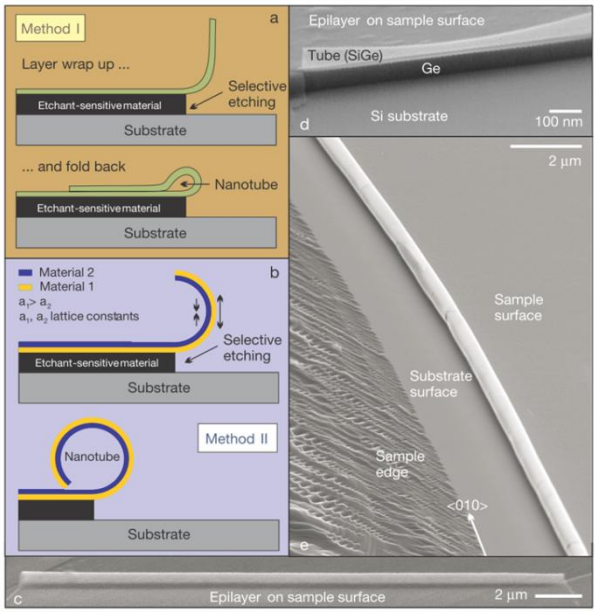

Figure 5.14: Nanotube formation (a) method I (b) method II (c) 12 μm long nanotube from method I (d) 50 nm diameter nanotube from method I (e) 12 μm long nanotube from method II [From Ref. 159]

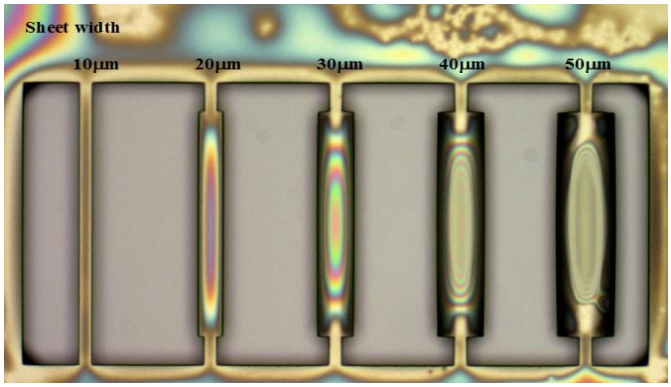

Figure 5.15: The optical image of nanotube and wire

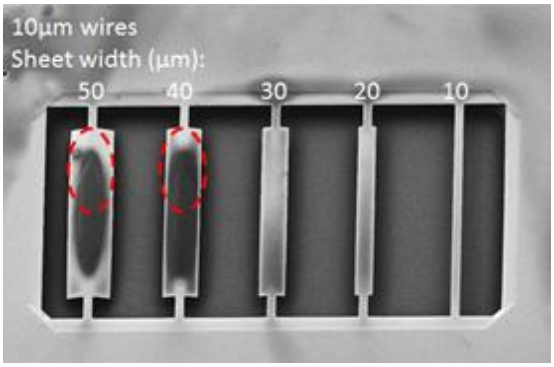

Figure 5.16: The SEM image of nanotube and wire, the larger sheets start to bend beneath their own weight (40µm and 50µm)

5.4 Electrical conductivity measurement

In this section, we investigate the electrical properties of bulk and suspended Ge via using the van der Pauw Greek-cross structure. A pair of van der Pauw Greek-cross structure were fabricated by using the same fabrication method (section 5.2), one is a suspended structure, as shown in Figure 5.9, and other remains as bulk material without undercutting the pattern, as show in Fig. 5.17.

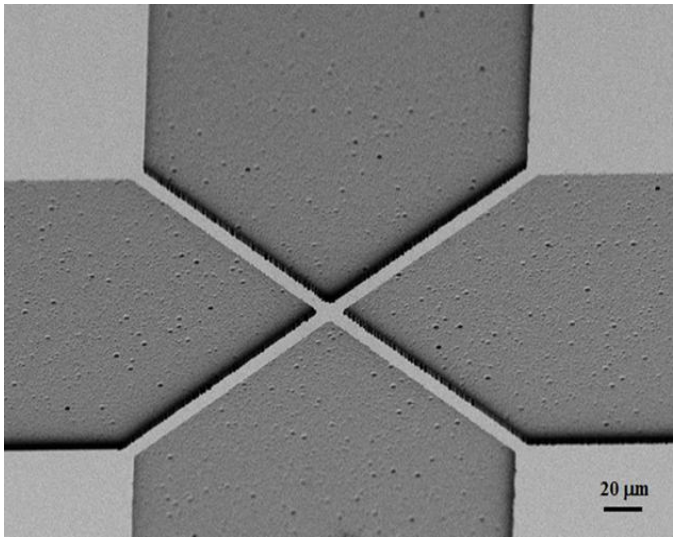

(a)

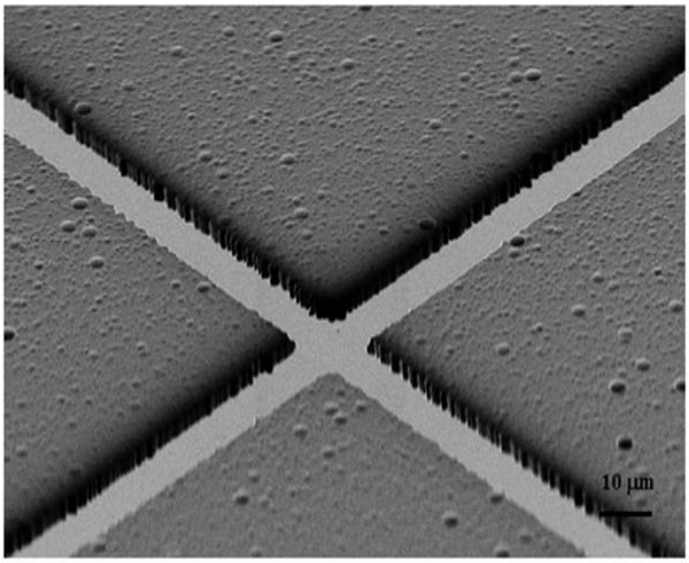

(b)

Figure 5.17: (a) The van der Pauw Greek-cross bulk structure (b) The centre of cross bulk structure

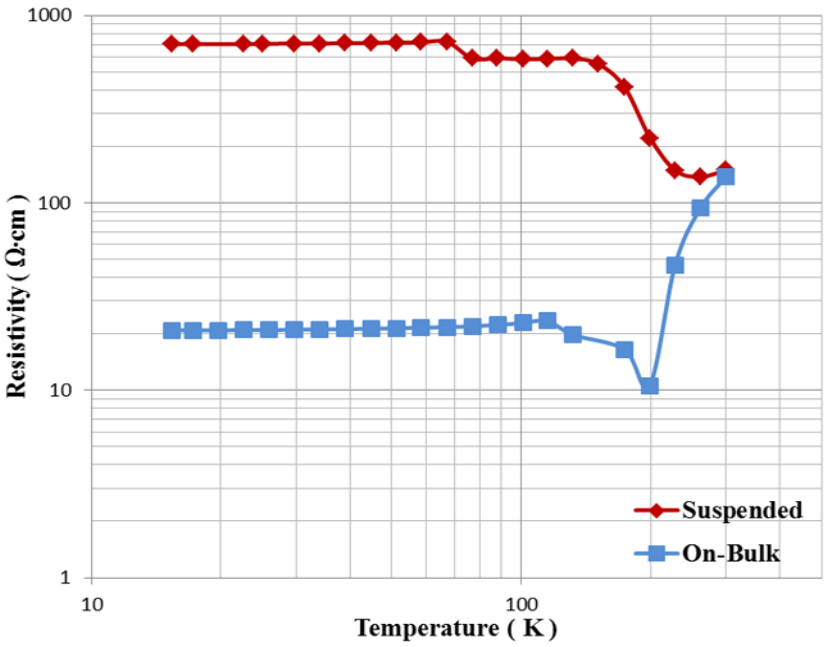

(a)

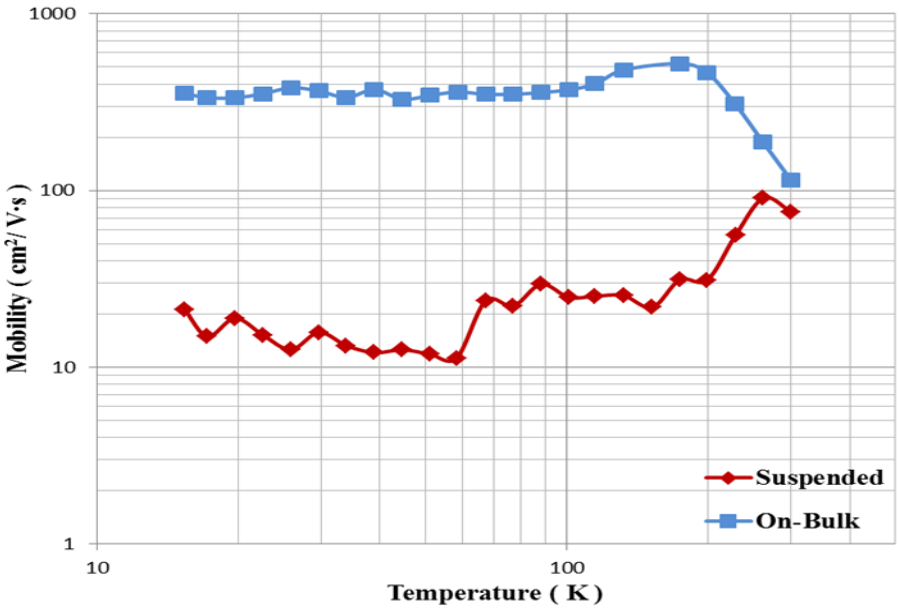

(b)

Figure 5.18: (a) the electrical resistivity of suspended and bulk van der Pauw Greek-cross structure (b) the mobility of intrinsic carriers in suspended and bulk van der Pauw Greek-cross structure

The electrical resistivity of the suspended and bulk van der Pauw Greek-cross structures is presented in Figure 5.18 (a). The effect of suspension is noticed as a resistivity shift of the two curves. The results show that the resistivity of the suspended structure sample is much higher than for the bulk sample, by about two orders of magnitude. At low temperatures, the carrier concentrations will decrease. As a result, the donor and acceptor impurity atoms do not ionize because the thermal energy of semiconductor is insufficient, known as the carrier freeze-out[160]. Therefore, it begin to freeze-out in suspended structure and the resistivity is increasing when the temperature down to 100 K. In the other hand, the resistivity of bulk structure starts to decrease. As a result of the additional conduction through the dislocation network due to carrier hopping between dislocation-localized states[161,162] the resistivity is further reduced in the bulk sample, whereas this does not happen in the suspended sample where the dislocations have been removed. Below 100K, the resistivity of both samples is seemingly temperature independent. It can be suggested that the additional conduction at low temperature in the bulk sample occurs because of the dislocations. This suggestion agrees with Osi'yan *et al.*[163].

The mobility of the suspended and bulk van der Pauw Greek-cross structures is presented in Figure 5.18 (b). The Hall measurement was made in a field of 600 mT. The mobility of the both structures differs dramatically. The mobility of the bulk sample is higher than for the suspended samples by about two orders of magnitude because of both free carriers and the leakage paths through the dislocations. By contrast when the dislocations are removed, in the suspended sample, then the mobility of the suspended samples is very low compared with the bulk samples.

The dislocation effects on suspended sample by the increased resistivity because of low dislocation network to conduct as well as lowered mobility that expect to be low because of

scattering from impurities and dislocation. At low temperature, it is possible to conclude that the dislocation is the main transport mechanism.

5.5 Conclusion

Suspended Ge structures have been fabricated: micro wires, spiderweb, the van der Pauw Greek-cross and nanotubes, by using the technique presented in section 5.2. The micro wires could be reduced in size to fabricate suspended Ge nanowires devices[147]. Because the TMAH etch rate depends on the crystal plane, the slowest etch rate of {111} can cause a pillar to remain underneath the suspended micro wires. However, this problem can be solved by rotating the samples by about 45°to avoid the {111} planes.

The suspended spiderweb can be fabricated for bolometers. The sample should be rotated by 41° to avoid the {111} for all the legs in the particular design used. In future designs a consideration of the alignment of all parts of the web with these planes would need to be included in initially laying out the structure. The thickness and the dimension of the spiderweb elements should also be considered in relation to the tensile forces experienced during and after fabrication. If the tensile force is not enough, the spiderweb cannot hold and remains stuck on the substrate surface. In addition, the spiderweb can be broken by the surface tension of liquid traped whilst the sample was removed from the various liquids such as TMAH, deionised water and isopropanol.

The nanotubes were produced suspended on a sheet that integrated on a wire. The results show that it did not completely underetch above 30μm sheet size because of Si pillars. However, 40μm sheet size starts to bend beneath to form nanotube but it did not completely form.

The van der Pauw Greek-cross structure can reveal the electrical properties of thin expitaxial layer such as resistivity and mobility via Hall measurement. The dislocation is the

important factor that affects the resistivity and mobility of suspended structure at low temperature. Low dislocation induced high resistivity because of low conduction network from dislocation and low mobility because more scattering from impurities and dislocation compared with bulk structure.

6 Electron-Phonon Interaction in P-doped Ge (Ge:P)

6.1 Introduction

The heat transport process in materials at low temperature (< 1K) is very interesting. Knowledge of this phenomenon can improve the various low temperature applications such as the hot/cold electron bolometer[68], microcoolers[47] and is also significant for fundamental physics studies. One essential concept of heat transport is the electron-phonon (e-ph) interaction, discussed in Section 2.3. The e-ph coupling constant directly influences the effectiveness of the hot/cold electron bolometer and microcoolers. Below 1 K, the e-ph interaction is very weak, therefore electrons can be easily overheated (or cooled) with respect to phonons at such low temperatures by a small power introduced into the electronic part of the system.

Thermal energy transfer between phonons and electrons decreases quite dramatically as the temperature decreases and is characterized by the e-ph coupling constant. For example, if the electrons are cooled, this can lead to large temperature differences between the electron and phonon systems. Within this work it is assumed that a characteristic temperature can be applied to each of the electron and phonon systems, i.e. that the electrons (or phonons) have a thermal distribution of energies. This assumption is reasonable because the electron-electron scattering rate, which leads to thermalisation of the electronic system, is much faster than relaxation by electron-phonon scattering. Moreover, the phonon system is assumed to be in good thermal contact with a large thermal bath, which maintains the phonon temperature at the bath temperature; however, under strong electron heating/cooling even the weak e-ph coupling will lead to some local heating/cooling of the phonon system, so it is important to measure this temperature as close to the active electronic devices as possible.

The e-ph coupling constant depends significantly on several factors such as the material, the level of disorder, and hence the electron mean free path and the type of scattering potential. At low temperatures, the e-ph relaxation rate has a form $\tau_{e-ph}^{-1} = \alpha T^{n-2}$ where α is a parameter that depends on the material[70]. The corresponding net power transferred from hot electrons to phonons is (previously given as Eqn 2.26)

$$P = \Sigma\Omega\left(T_e^n - T_{ph}^n\right) \tag{6.1}$$

where T_e and T_p are the electron and phonon temperatures respectively, $\Sigma = {}^{\alpha\gamma}/_{n}$ is the e-ph coupling constant[70] describing the strength of e-ph coupling and is a material dependent parameter, Ω is the volume and *n* is the exponent determined by the disorder that depends on the product of the thermal phonon wavevector (*q*) and electron mean free path (*l*).

For ordered (pure) metals in the clean limit defined as $ql >> 1$, where $q = k_B T_{ph}/\hbar u$ is the wavevector of dominant thermal phonons, electrons can scatter either from longitudinal phonons only, or from both longitudinal and transverse phonons, depending on the temperature and the material[47] and *u* is the velocity of sound in the material. For disordered metals in the dirty limit when $ql << 1$, electrons scatter strongly from impurities, defects and boundaries. In this case, the situation is more complicated to model because of the interference processes between pure electron-phonon and electron-impurity scattering events. The exponent *n* in the power law again depends on material and temperature. More detail was presented in the introduction (Chapter 1), and background theory (Chapter 2).

This Chapter is concerned with the study of the electron-phonon interaction in P-doped Ge(Ge:P) at low temperatures. The heat flow between electrons and phonons was observed, as a function of temperature, with the help of the superconductor-semiconductor-superconductor (S-Sm-S) double tunnel junctions used as thermometers. The exponent *n* and

the e-ph coupling constant were determined. The e-ph thermal conductance was also investigated.

6.2 Experiment

6.2.1 Experimental outline

The samples used in this experiment were germanium doped with phosphorus at $4x10^{19}$ cm^{-3} (Ge:P). The sample thickness and volume were 250 nm, and 344 μm^3 respectively. The samples were fabricated by using the lithography and SF_6-O_2 plasma etching described in the Chapter 4. A schematic diagram of the sample is shown in Figure 6.1. The measurement was performed in a Heliox AC-V at a set of fixed bath temperatures between 312 mK and 600 mK. The heat flow from the electron system to the phonon system was determined when the bar was heated using a slowly swept voltage bias (V) while the corresponding current (I) was measured as shown in Figure 6.2. The power input can be determined as $P = IV$ and the response of the system can be recorded by measuring the electron temperature.

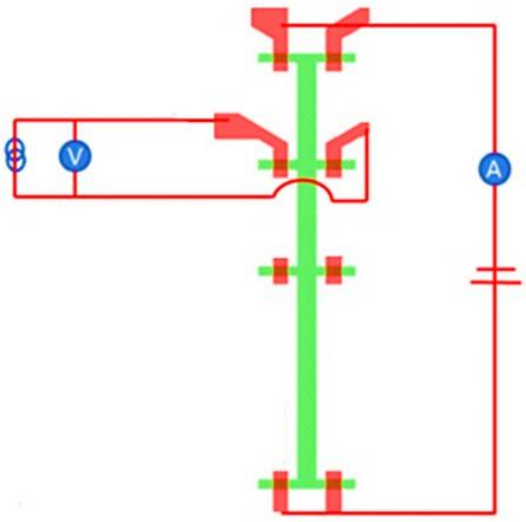

Figure 6.1: Sample Geometry

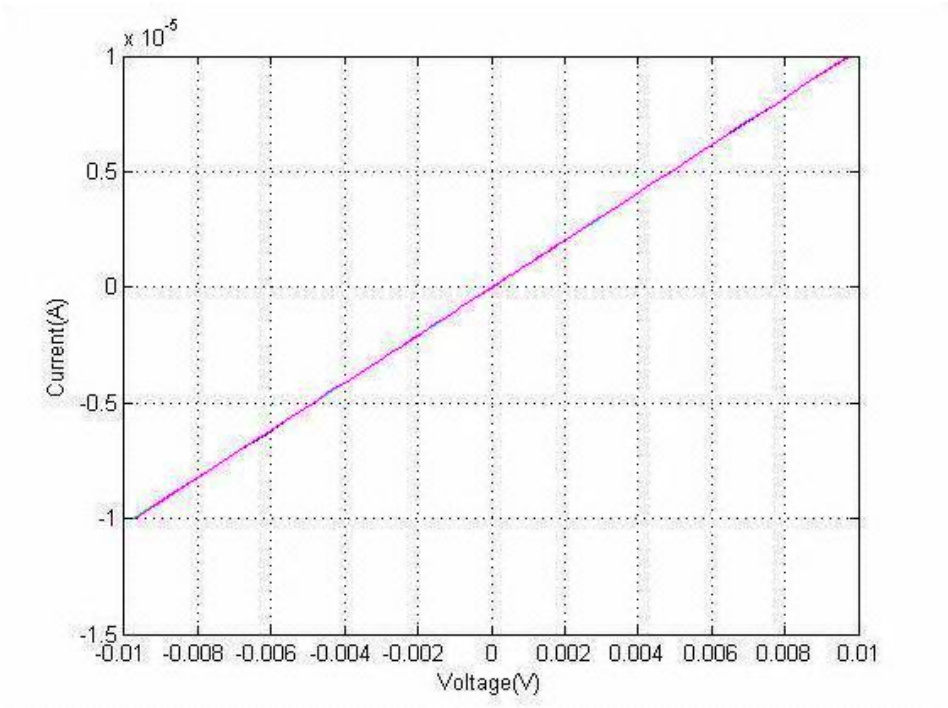

Figure 6.2: The corresponding current *I* as a function of sample biased voltage

6.2.2 Measurement of electron temperature

In the experiment, the electron temperature was measured by using a S-Sm-S tunnel junction thermometer. The current-voltage characteristics (I-V) of the S-Sm-S thermometer were measured at different bath temperatures between 312 mK to 600 mK and the results shown in Figure 6.3 reveal a strong temperature dependence. By using a constant 10 nA bias current the horizontal line in Figure 6.3 shows how the junction voltage variation can be read as a measure of electron temperature. Figure 6.4 is the correspondence between the voltage across the S-Sm-S thermometer and the temperature, i. e. the temperature calibration curve.

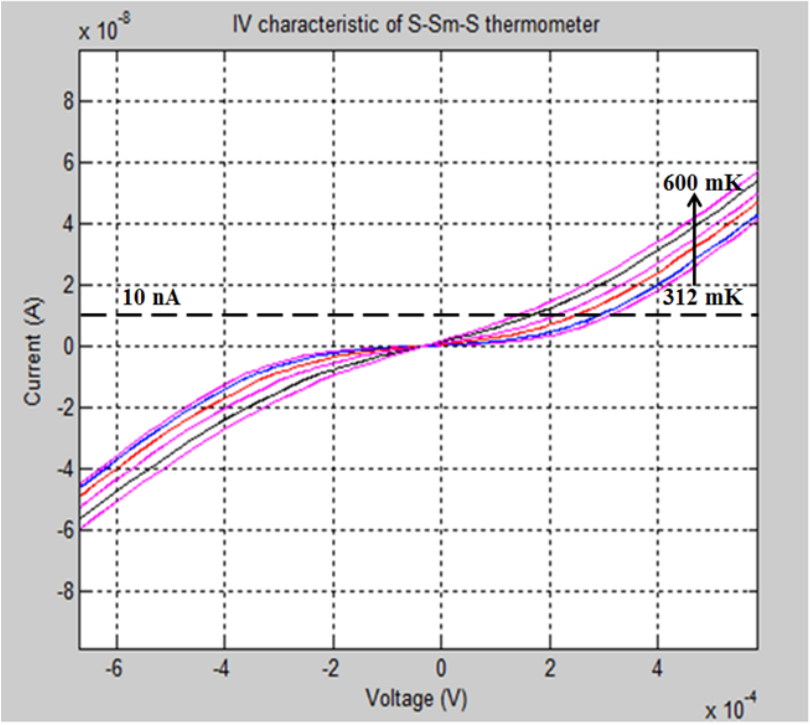

Figure 6.3: The I-V characteristics of a S-Sm-S thermometer for bath temperatures between 312 mK and 600 mK. The horizontal dashed line allows the junction voltage at different temperatures to be read off when biased by a constant 10 nA current.

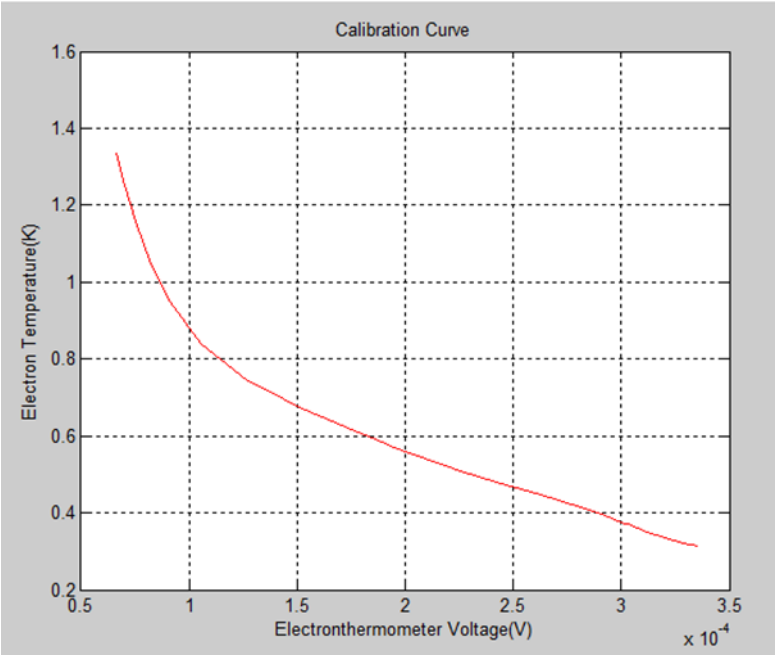

Figure 6.4: S-Sm-S thermometer calibration curve, biased by a constant current (10 nA)

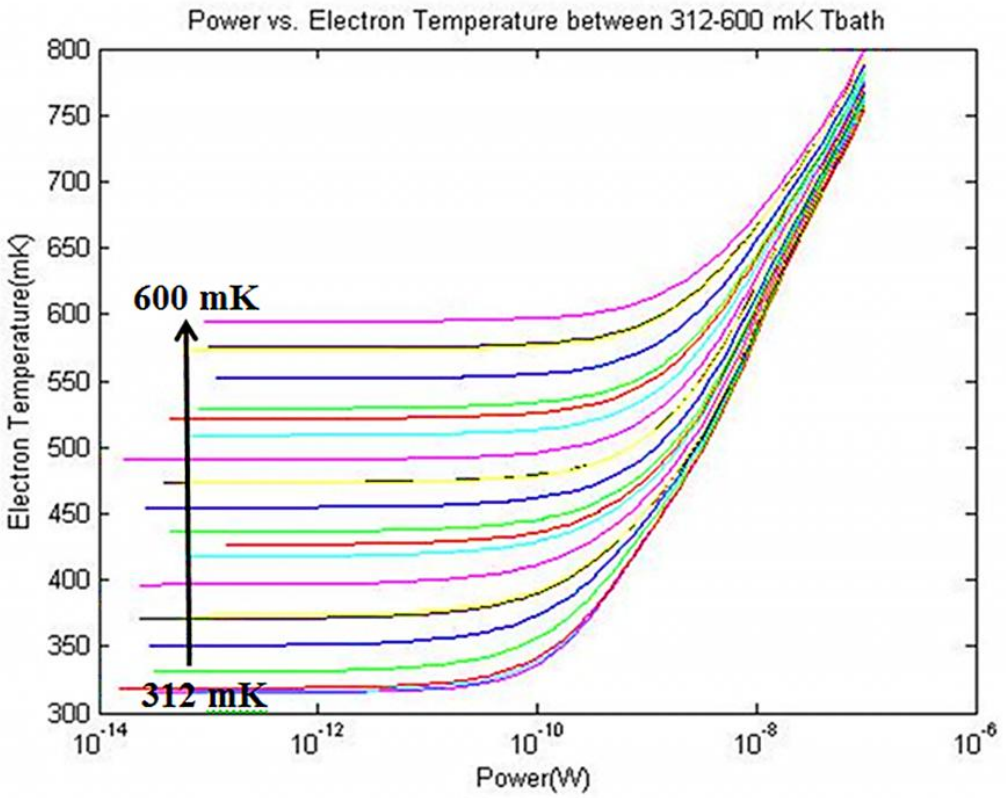

Figure 6.5: The electron temperature as a function of power for T_{bath} from 312 mK to 600mK

The electron temperature measured in this way is shown in Figure 6.5 as a function of power input ($P=IV$), for a range of bath temperatures. It can be seen that at low input power the electron temperature follows the bath temperature. In this region the power extracted by electron-phonon coupling is greater than the electrical power input. At higher input power electron-phonon coupling is not able to extract sufficient heat and so the electron temperature increases, eventually reaching a high temperature that becomes independent of the original bath temperature.

The following relationship for the electron temperature, derived from equation 6.1, is instructive

$$T_e = \left(\frac{P}{\Sigma\Omega} + T_{ph}^n\right)^{1/n} \tag{6.2}$$

It indicates that at a small bias voltage, when P approaches to zero, the bias voltage does not provide enough energy to increase the electron temperature significantly higher than the phonon temperature. Then the electron temperature $T_e \sim T_{ph} = T_{bath}$. In the other limit, when the electrons were heated by a large bias voltage, the electron temperature only relies on the power, $T_e \propto P^{1/n}$ (regardless of the phonon temperature). These two regimes are clearly indicated in Figure 6.6 for the lowest bath temperature of 312 mK.

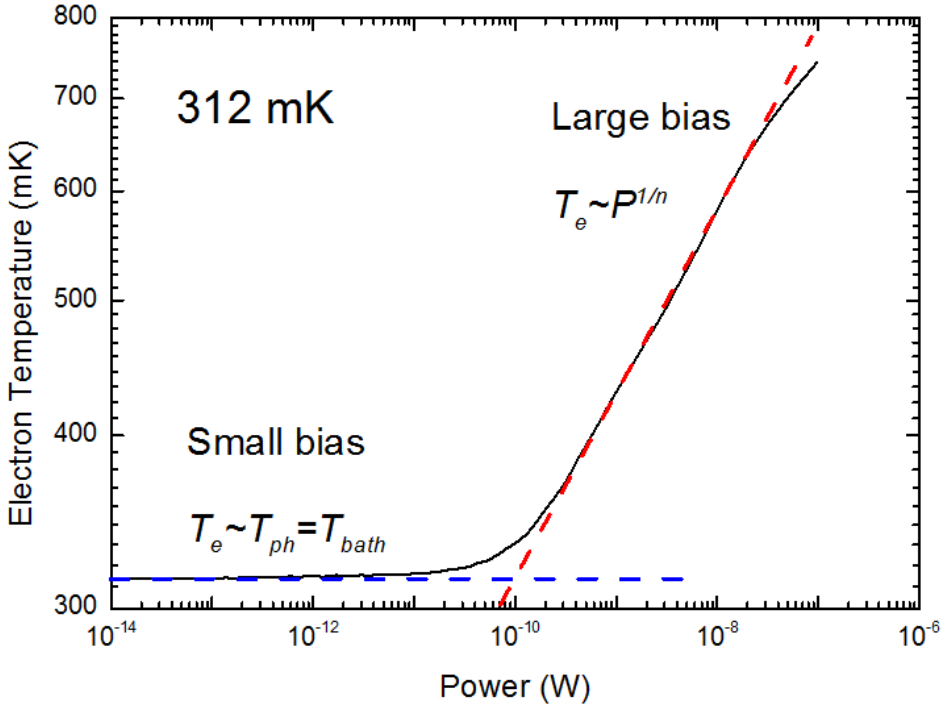

Figure 6.6: The electron temperature as a function of power for T_{bath} = 312 mK, with dashed lines showing regions where input power is either less than (blue) or greater than (red) the power extracted by e-ph coupling.

6.2.3 Measurement of electron-phonon coupling

If it is assumed that $T_{ph} = T_{bath}$, then *n* and $\sum$ can be estimated for electrons in Ge. From the slope of the large bias region of Figure 6.6 (red dashed line) an estimate can be made of *n* = 7.3±0.3.

Then, using the sample volume of 344 μm^3, the heating power density can be plotted against $\left(T_e^n - T_{ph}^n\right)$ for various *n* in Figure 6.7 with the cryostat held at T_{bath} of 312 mK. According to the theoretical behaviour the power density should follow a power law (Eq. 6.1) with *n* = 7 (or *m* = 5 since *m*=*n*-2). In Figure 6.7, the experimental data is plotted for *n* = 6(blue), 7(green) & 8(red) on a log-log plot. There are also a set of dashed lines with unit gradient that the data should follow if a power law is obeyed for a given *n*. At low power density the input power is less than can be extracted by electron-phonon coupling so the power law behaviour does not apply. Focussing on the data at higher bias where the electron temperature is limited by electron-phonon coupling, it can be seen that the best agreement with these straight lines comes from the green data with *n* = 7. The red data for *n* = 8 has a lower than unity slope and the blue data with *n* = 6 has a greater than unity slope, so neither of these produce good power law fits to the data. From this type of analysis it is not really possible to determine the power law to much greater accuracy than the nearest integer. At the highest power input one might choose a value somewhat larger than 7 (7.3 was found from Figure 6.6) but in a slightly lower power region a value of *n* below 7 could be justified. Nevertheless, the behaviour seems to follow a reasonable power law over three orders of magnitude. Hence, it can be concluded that the electron-phonon relaxation rate has a form $\tau_{e-ph}^{-1} \propto T^5$. From a linear fit to the *n* = 7 curve of Figure 6.7 the e-ph coupling constant can then be found as $\Sigma = 1.31 \times 10^9$ W/m^{3}K^7.

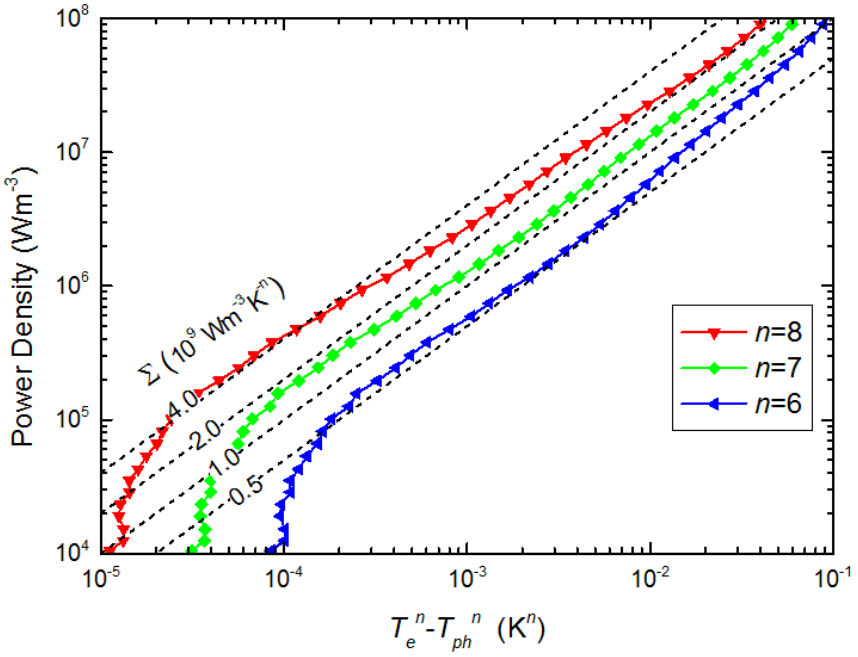

Figure 6.7: The power density removed by electron phonon coupling as a function of the excess temperature expressed as $\left(T_e^n - T_{ph}^n\right)$ for T_{ph}=T_{bath} = 312 mK, for different values of the exponent *n*. Dashed lines have unit gradient on this log-log plot and allow the e-ph coupling constant to be found via Equation 6.1. It can be seen that the experimental data best follow a line of unit gradient for the green points with *n*=7.

Similar heating data is available (see Figure 6.5) for different bath temperatures up to 600 mK and the power law region of these are shown in Figure 6.8. Again the e-ph coupling constant can be extracted from these curves, using Equation 6.1. This is plotted in Figure 6.9 where it appears to be decreasing as the temperature increases. Also shown is an extrapolation of the data to zero temperature where apparently $\Sigma = 2.2\text{x}10^9$ Wm^{-3}K^{-7}. However, inspection of the original data in Figure 6.5 shows that as the bath temperature is increased it takes a greater input power to reach the large bias region, where the power law

behaviour is expected, so this apparent temperature dependence of Σ may be due to not reaching the correct regime for its extraction at the higher bath temperatures.

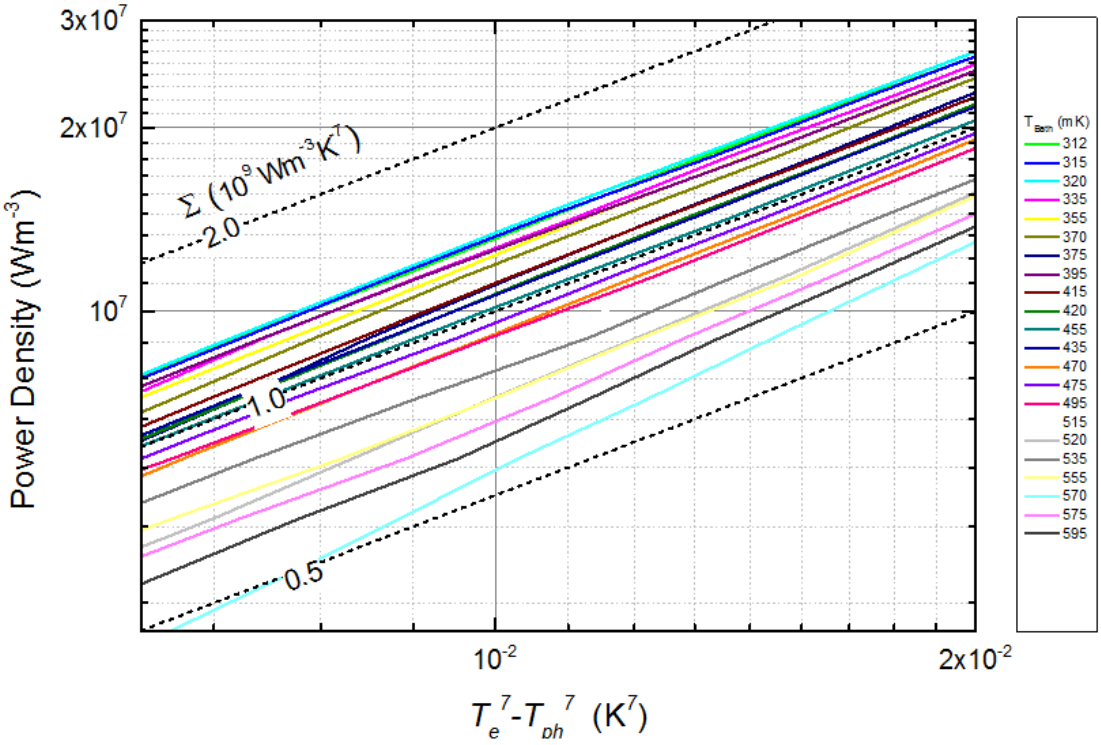

Figure 6.8: As Figure 6.7 for a range of different bath temperatures and with *n*=7 only.

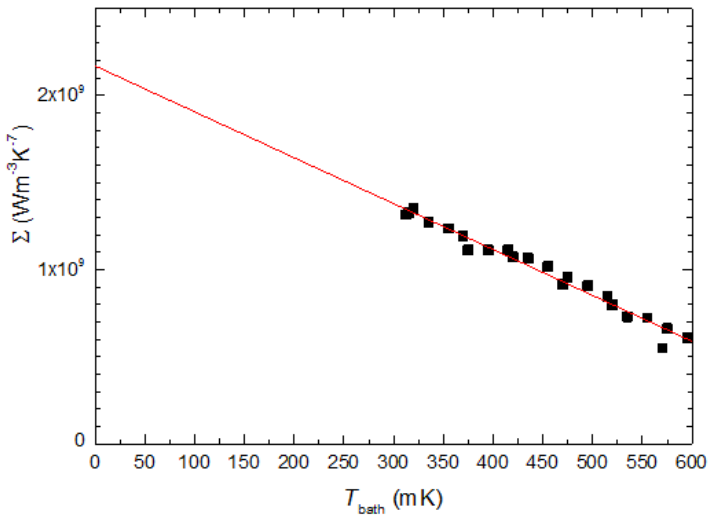

Figure 6.9: Electron-phonon coupling constant extracted from Figure 6.8 for a range of bath temperatures. The line is a linear extrapolation through the data.

Another result that can be extracted from Equation 6.1 is the e-ph thermal conductance: G_{e-ph}. This parameter is often used to measure the cooling strength.

$$G_{e-ph} \equiv {\partial P}/{\partial T_e} = n\Sigma\Omega T_e^{n-1} \tag{6.3}$$

For measurements with T_{bath} between 312 mK and 600 mK the e-ph thermal conductance is plotted in Figure 6.10 by using the lowest heating power data point. The results indicate that the e-ph thermal conductance has a strong electron temperature dependence, $G_{e-ph} \propto T_e^{n-1}$ and confirms that heat flow between electron and phonon system that we studied is proportional to T^7.

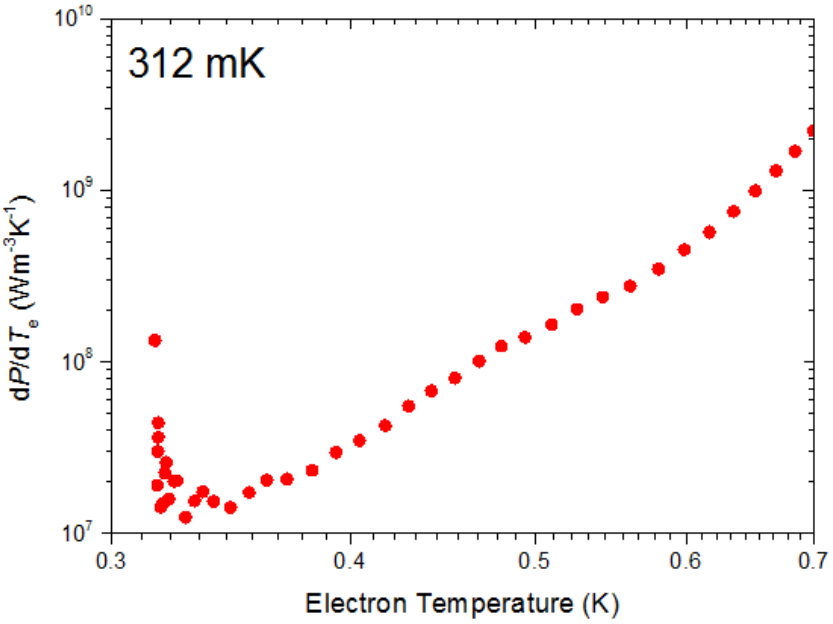

Figure 6.10: The electron-phonon thermal conductance as a function of electron temperature at 312 mK T_{bath}

For hot electron bolometer, the performance of the bolometer is limited by thermal fluctuations. The efficacy of bolometer can be presented in terms of its noise equivalent power (*NEP*). *NEP* is the sensitivity of a photodetector or detector system and given by[74]

$$NEP = \sqrt{4k_B T^2 G} \tag{6.4}$$

Where is k_B Boltzmann's constant, T is temperature and G is the total thermal conductivity that can approximate that $G \approx G_{e-ph}$[74,164]. From equation (6.3) , *NEP* is then

$$NEP = \sqrt{4k_B n \Sigma \Omega T^{n+1}} \tag{6.5}$$

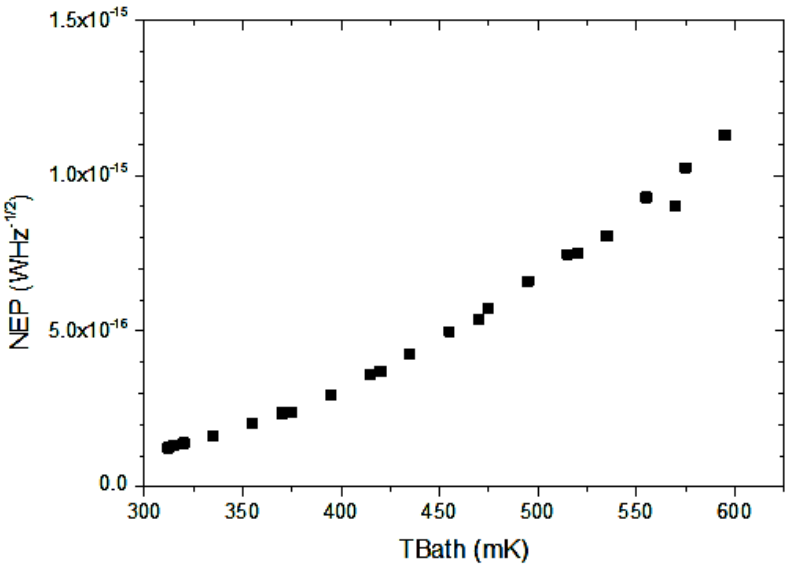

Figure 6.11: Noise equivalent power as a function of temperature.

Clearly the *NEP* is minimised for the lowest temperature and when T_{bath} at 312 mK is the NEP is just $1.2 \times 10^{-16} WHz^{-1/2}$.

6.3 Discussion

The theory case of disordered metal, the heat flow rate of the electron- phonon interaction has different power law temperature dependence. The exponent is determined by the level of disorder and the property of the impurity in materials. In the clean limit, the electron-phonon relaxation rate has a T^2 dependence whereas in the dirty limit the rate depends on the temperature as T^4 with impurity scattering completely dominating over phonon scattering in this case[165]. The work of Sergeev and Mitin[71] suggested that if the impurity potential of elastic scatterers includes heavy defects that do not vibrate with the phonons, the temperature dependence can be different. Then, the doped semiconductor can obey the theory as well because the dopant atoms (elastic scatterers) are coupling with the host lattice[66].

In this thesis, thermal properties of germanium doped with phosphorus ($4x10^{19}$ cm^{-3}) were investigated. At T_{bath} of 312 mK , the results indicate that heat flow from hot electrons to phonons corresponds with equation (6.1) when n =7, indicating that the electron-phonon relaxation rate is proportional to T^5. The exponent is different from the theory[165] that was expected, but corresponds with the assumption of Prunnila *et al.*[66] . It could possibly be explained by the combination of strong disorder and surface modes[41]. In addition, Taskinen *et al.*[166] reported that the electron-phonon relaxation rate of disorder materials, in that case a thin Al-Mn film, also appeared to be proportional to T^5.

Comparing with doped Si, Kivinen *et al.*[167] investigated the heat flow between the electron gas and the phonon system in a similarly heavily doped silicon ($3.5x10^{19}$ cm^{-3}) at 300 mK. They found that the power law is a T^6 dependence (T^4 dependence of the electron-phonon relaxation rate) that corresponded with theory. However, it is found here that the heat flow between the electron gas and the phonon system of Ge:P has a higher power temperature dependence than doped Si due to the different band structure.

The e-ph coupling was investigated. Low e-ph coupling is beneficial for the operation of low temperature detector[48] and solid state electron coolers[168]. Then, e-ph coupling constant (Σ) should be low as possible. In this thesis found that the e-ph coupling constant is 1.31×10^9 W/m^{3}K^7 (T^7 power law) for the germanium doped with phosphorus (4×10^{19} cm^{-3}) at T_{bath} of 312 mK.

For low temperature applications (< 1 K), the bolometer requires the low thermal conductance for high performances[164]. Therefore the e-ph thermal conductance was investigated. The e-ph thermal conductance is strongly electron temperature dependence as shown in equation (6.3). From equation (6.3), the e-ph thermal conductance can be decreased if the e-ph coupling constant is low as much as possible. In addition, *NEP* was investigated and found that the efficiency of bolometer can increase when e-ph coupling constant was decreased and higher efficiency when works at lower temperature. The research found that the highest efficiency presented when work at lowest bath temperature 312 mK, and e-ph coupling constant is minimum as well.

7 Conclusions and Further Work

7.1 Conclusion

As it may be desirable to replace Si by Ge for a number of applications, the basic properties of Ge must be understood. This research is concerned with the characteristics of Ge after micro-fabrication and with its thermal properties at low temperature. For micro-fabrication, this research investigated the use of a dry etching process to fabricate low thermal conductance Ge platforms for mK tunnelling coolers. The most prominent of the advanced dry etching technique is reactive ion etching (RIE), which normally uses a SF_6-O_2 gas mixture. Up to now, most authors have put their effort into developing the etching process of Si, rather than Ge. Therefore, reactive ion etching of Ge and doped Ge has been studied using the SF_6-O_2 gas mixture and with Si as a control material. Regarding the thermal properties of Ge at low temperature, the heat flow from electrons to phonons and the electron-phonon coupling have been the main topics of interest. Finally, in the search for a low thermal conductance platform, the microfabrication of suspended structures has been investigated. Summaries of this research and previous work are shown below:

7.1.1 The dry etching process of Ge in a SF_6-O_2 radio-frequency plasma

Currently, many authors are concentrating their efforts to discover the benefit of Ge that will replace Si in micro-fabrication. Since the advanced structures in modern micro-fabrication are complicated, knowledge of the dry etching process is very important because it helps to provide improved dimension reduction, deep etching and moreover improve precise control of line width and vertical profile. For a deep understanding of the micro-fabrication process, the dry etching process of Ge should itself be thoroughly understood.

In this thesis, the study has investigated reactive ion etching (RIE) of single crystal Ge at low working pressures. Reactive ion etching involves two etching process: physical etching

and plasma etching, which is chemical etching. At low pressure, the etching process is more influenced by physical etching than plasma etching. The gas for etching is the mixture of SF_6 (sulphur hexafluoride gas) and O_2 (oxygen gas). The two types of etching gas affect the side wall profile in different ways. The SF_6 gas induces the side wall profile to be an isotropic, whereas the O_2 encourages the side wall profile to be an anisotropic. The relative proportion of gases depends on the side wall profile that is required for the particular project purpose. Moreover, the proportion of gas mixture influences the etching rate. This research has monitored the behaviour of the etching rate and the side wall profile when the portion of gas mixture is changed by varying the amount of O_2 in gas mixture from 0% to 90%.

The study concerns two specific aspects of the etching process. The first is the etching rate and the second is the side wall profile after etching. The materials that were used in this study were a layer of intrinsic Ge and two doped Ge layers with different levels of phosphorous doping. One was lightly doped Ge ($1x10^{18}$ cm^{-3}) and the other was heavily doped Ge ($3x10^{19}$ cm^{-3}). All the Ge layers were deposited on Si (001) substrate by using reduced pressure chemical vapour deposition (RP-CVD). A Si (001) substrate was used as a control sample.

The characteristic etch rate obviously changes when the content of O_2 in the gas mixture is modified. For all types of Ge, the same trend of etch rate was observed when the O_2 content is changed. However, the etch rate of lightly doped Ge is higher than for both the intrinsic Ge and the heavily doped Ge. For up to 5% of oxygen gas, all types of Ge show that the etching rates increase rapidly, but then dramatically decrease between 5% - 20%. However, when the O_2 content is increased from 20% to 70%, the etch rate remains approximately constant. Nevertheless, there is a gradual decrease above 70% O_2 content. For the control sample (Si), the etch rate is lower than for all types of Ge apart from in the range of 10% -

50%. The characteristic Si etching rate presents the same trend as Ge from 0% to 5% and above 70%. From 5% - 70%, the Si etching rate gradually decreases.

The O_2 fraction has a significant influence on the etch rate because the amount of oxygen atoms affects the chemical interaction in the plasma. At low content of oxygen gas in the mixture (up to 5%), the concentration of the etchant species (F radicals, F*) increases because the O atoms in the plasma reduce the SF_x/F recombination rates. Therefore the etching rate is rapidly increasing. At the lowest O_2 fraction examined, $\%O_2 = 5\%$, the maximum etch rate seen in this work occurs. Above 5% of O_2, O atoms increasingly compete with F* for occupancy of active sites on the surface then the etch rates trend to decrease. The etch rate of Si is less than for Ge because of the superficial layers of SiO_xFy and GeO_xFy which form on the surfaces and impede chemical etching (isotropic side wall profile): the Ge-O bond (3.66eV) is more readily broken than the Si-O bond (4.82eV) because of the difference in binding energy. Below 5%, we postulate that the concentrations of SiO_xF_y and GeO_xF_y are not high enough to affect the etch rates.

For doped Ge, it is assumed that the etching mechanism of Ge:P[L] can be explained by the charge transfer mechanism[102]. For an n-type semiconductor, an electron from the conduction band tunnels through the potential barrier at the surface and reaches the chemisorbed F atom. The F atom is thus negatively charged to form a surface dipole involving the ionized donor atoms (P) in Ge, giving a higher etch rate[103]. It is suggested that the lower etch rates seen in the more highly doped Ge could be a result of the suppression of the tunnelling process, due to the potential fluctuations of the band edges (band tailing), which occurs at higher n-doping concentrations.

The side wall profile of the etched mesas was analysed by SEM. The side wall profiles of Si and all types of Ge change in the same way as the O_2 content in gas mixture is varied. When the Si and Ge side wall angles are compared for the same concentration of oxygen, it is

observed that there is no significant difference. At low O_2 content (up to 20%), the results show that the side wall profile is isotropic because F radicals are the dominant species (chemical etching dominates). The cause of isotropic can assume that the F radicals created in the plasma are absorbed in the etched surface and move until they reach a lowest potential energy sites at bottom of the mesa, causing lateral etching of the mesa. At $\%O_2$ = 20%, a perfect anisotropic mesa where θ=90° is achieved. In other words, $\%O_2$ = 20% is the transition point between chemical etching and physical etching or the transform from isotropic to perfect anisotropic. Above 20% of oxygen content, the side wall profile is partial anisotropic due to the re-deposition of SiO_xF_y and GeO_xF_y etched products.

7.1.2 Creation of suspended Ge structure

To increase the efficiency of a cooling device fabricated on a platform, heat leaks from the environment into the platform must be eliminated, or at least reduced as much as possible. A suspended structure can achieve this aim for thermal isolation. The crystalline membrane is the best material in this case compare with silicon nitride membrane (fragile) and amorphous materials (thick). The crystalline membrane is thinner and so less thermally massive, and has a smoother surface compared with amorphous materials. Moreover, a thinner crystalline membrane can be used for the same mechanical strength and also opens the possibility of fabricating the complete device on the platform. For higher efficiency, the platform should have a low thermal conductance to reduce the heat flow from the surroundings into the system. In this thesis, the fabrication of a low thermal conductivity platform has been investigated and Ge membranes are considered.

The main fabrication techniques of photolithography, dry and wet etching process, set out in more detail in chapter 3 and 5, were used to produce a range of suspended structures. These included micro-wires, spiderwebs, and bridged structures. During the fabrication the

issue of anisotropic etching by TMAH had to be addressed, as otherwise the low etch rate for {111} Si meant sections of the structures along these directions failed to be released. The problem was solved by rotating the designs such that no lines aligned with {111}. Another issue to avoid was trapping of liquid underneath suspended legs, which could lead to them breaking due to surface tension effects when the structures were removed from the liquid. Tension in the Ge layer that resulted from the epitaxial growth was key to creating suspended bridges and wires, of up to 200μm long, by preventing them from collapsing to the substrate.

By fabricating a suspended van der Pauw Greek-cross structure the effect of the misfit dislocation network at the Si-Ge interface on the electrical properties of the Ge epitaxial layer was investigated. Resistivity and mobility measurements between 15 K and 300 K showed that the resistivity of the suspended sample is much higher than in the bulk sample, because the suspended sample does not have electrical leak underneath through the misfit dislocations.

7.1.3 Electron-Phonon (EP) interaction in P-doped Ge (Ge:P)

An understanding of the electron-phonon interaction is important for many low temperature devices, such as bolometers, calorimeters and on-chip refrigerators. For bolometers, electron-phonon coupling affects the device sensitivity. A weak electron-phonon coupling can increase the sensitivity of the bolometer by isolating the electrons form their surroundings. For a cooler, a high electron-phonon coupling would be a benefit to enable more efficient lattice cooling.

This research has studied the electron-phonon interaction of germanium doped with phosphorus ($4x10^{19}$ cm^{-3}). From knowledge of the Ge etching process, developed in Chapter 4, patterned Ge samples can be fabricated. The measurements were performed in a Heliox AC-V at sub-Kelvin temperatures. A S-Sm-S structure used as the thermometer was first

calibrated by very slowly varying the bath temperature between 312 - 600 mK. Then, to measure the electron temperature, the S-Sm-S structure was biased by using a constant current of 10 nA. The phonon temperature was considered to be equal to the bath temperature. The heat flow from electrons to phonons was determined when the bar was heated, by using slowly swept voltage bias (V) and measuring the corresponding current (I). In this way the amount of electron-phonon coupling was determined.

At 312 mK bath temperature, the results indicate that heat transfer from hot electron to phonon corresponds to $P = \Sigma\Omega\left(T_e^n - T_{ph}^n\right)$ with n =7, and the electron-phonon coupling constant was found to be 1.31x10^9 W/m^{3}K^7 by using numerical analysis. The mean free path was calculated using the Drude formula, to be l = 0.7 nm and the thermal phonon wavevector q to be of order 10^6 m^{-1}. Therefore, our case is in the dirty limit, $ql << 1$ because of the impurities and defects. In the theoretical calculation of Sergeev *et al.*[72], our case corresponds to strong screening and is also in the impure limit. In this case, they present that the electron-phonon relaxation time depends on T^6/l. From our data analysis, the electron-phonon relaxation time depends on T^5 , which is different from the theory of Sergeev *et al.*[72] This corresponds to the heat flow between electrons and phonon that is proportional to T^7, which could possibly be explained by the combination of strong disorder and surface modes[41].

7.2 Further work

Some additional aspects to investigate from the work of this thesis include:

7.2.1 The dry etching process of Ge in SF_6-O_2 radio-frequency plasma

The addition work for this section should be characterization of the plasma during the etching process and surface analysis of the material produced. It could be achieved by using mass spectroscopy and optical emission spectroscopy. The plasma characterizations should be investigated in discharge products, the etch products, the residue produced, and the gas phase compositions. The fluorine concentration in the plasma, as a function of $\%O_2$ in the SF_6-O_2 gas mixture, and the main etch products, SiF_4 and GeF_4, should be investigated. In addition, surface analysis should be applied to investigate the composition of the superficial species on the surface: SiO_xF_y and GeO_xF_y. The results show that the perfect anisotropic etch can be achieved by using 20% O_2 content in the SF_6-O_2 gas mixture. Although this work has considered the mix of gases, there are many parameters involved in the etching process. The pressure, gas flow rate and RF power should be investigated as well. Another avenue to investigate would be to demonstrate deep etched samples by using 20% O_2 content in the SF_6-O_2 gas mixture.

7.2.2 Creation of suspended Ge structure

Various types of suspended structure were successfully fabricated. Moreover, the electrical properties of a suspended structure were measured by using the van der Pauw Greek-cross structure and Hall measurement technique. The next step should be measurement of thermal conductance. There are two methods that has been used to measure thermal conductivity of Ge membrane. The first method is thermal diffusivity by using thermal transient gradient (TTG) method. The second is the thermal mapping by using 2-laser Raman

thermometer. Moreover, the van der Pauw Greek-cross structure can also be used to measure the thermal conductivity.

7.2.3 Electron-Phonon (EP) interaction in P-doped Ge (Ge:P)

The phonon temperature is considered to equal the bath temperature in this research. For a deeper understanding, the real phonon temperature should be measured by using the S-Sm-S structure. Some authors report that doping level can affect the electron-phonon coupling, so the doping level in P-doped Ge should be investigated as well. Moreover, the influence of sample thickness should be considered, as this could affect the electron phonon interaction. Some authors[107] report that an increase of thickness leads to an increase of the mean free path. It means that increasing their thickness can push the samples closer to the clean limit.

Bibliography

1. R. C. Jaeger, IEEE International Conference on Computer Design: VLSI in Computers 1986.
2. S. Karajgikar, N. Lakhkar, D. Agonafer, and R. Schmidt, Thermal and Thermomechanical Phenomena in Electronic Systems, 2004. ITHERM '04. The Ninth Intersociety Conference
3. P. M. Solomon, Materials, Devices, and Systems, in Low-Temperature Electronics edited by R.K. Kirschman, IEEE Press, New York, 1985.
4. J. V. Radostitz, I. G. Nolt, P. Kittel, and R. J. Donnelly, Rev. Sci. Instrum. **49**, 86 (1978).
5. P. J. Shirron, E. R. Canavan, M. J. DiPirro, J. G. Tuttle, C. J. Yeager, Adv. Cryog. Eng **45**, 1629 (2000).
6. R. W. Keyes, E. P. Harris, and K. L. Konnerth, The Role of Low Temperature in the Operation of Logic Circuitry, in Low-Temperature Electronics edited by R.K. Kirschman, IEEE Press, New York, 1985.
7. M. Nahum, T. M. Eiles, and J. M. Martinis, Appl. Phys. Lett. **65**, 12 (1994).
8. J. P. Pekola, A. J. Manninen, M. M. Leivo, K. Arutyunov, J. K. Suoknuuti, T. I. Suppula, B. Collaudin, Physica. B **280,** 485 (2000).
9. J. Niemeyer, Physica. C **372**, 291 (2002).
10. A. M. Savin, M. Prunnila, P. P. Kivinen, J. P. Pekola, J. Ahopelto, and A. J. Manninen, Appl. Phys. Lett. **79**, 1471 (2001).
11. L. Colace, G. Masini, F. Galluzzi, G. Assanto, G. Capellini, L. Di Gaspare, E. Palange, and F. Evangelisti, Appl. Phys. Lett. **72**, 3175 (1998).
12. Y. D. Park, A. T. Hanbicki, S.C. Erwin, C. S. Hellberg, J. M. Sullivan, J. E. Mattson, T. F. Ambrose, A. Wilson, G. Spanos, B. T. Jonker, Science **295**, 651 (2002).
13. K. Wei, D. P. Machewirth, J. Wenzel, E. Snitzer, and G. H. Sigel, Jr., Optics Letters **19**, 904 (1994).

14. M. Bosi, G. Attolini, Prog. Cryst. Growth Charact. Mater. **56**, 146 (2010).

15. M. Bosi, C. Pelosi, Prog. Photovolt. Res. Appl. **15**, 51 (2001).

16. A. Luukanen, M. M. Leivo, J. K. Suoknuuti, A. J. Manninen, and J. P. Pekola, J. Low. Temp. Phys. **120**, 281 (2000).

17. K. C. Saraswat, High mobility channel materials for future CMOS, International Symposium on VLSI Technology, Systems and Applications (VLSI-TSA), pages 1–4, Hsinchu, Taiwan, 2007.

18. G. Masini, L. Colace, G. Assanto, H.-C. Luan, K. Wada, and L. C.Kimerling, Electron. Lett. **35**, 1467 (1999).

19. J. Neamen, *Semiconductor Physics And Devices*, McGraw-Hill, 1988.

20. F. J. Low, J. Opt. Soc. Am. **51**, 1300 (1961).

21. J. Clark, G. I. Hoffer, P. L. Richards, and N. –H. Yeh, J. Appl. Phys. **48**, 4865 (1977).

22. T. R. Lyle, Phil. Mag. **3**, 310 (1902).

23. S. Sedky, P. Fiorini, M. Caymax, A. Verbist, and C. Baert, Sens. Actuators. A **66**, 1 (1998).

24. J. Zmuidzinas, P.L. Richards, Proc. IEEE **92**, 1597 (2004).

25. D. P. Osterman, R. Patt, R. Hunt, J. B. Peterson, Appl. Phys. Lett. **71**, 2361 (1997).

26. P. D. Mauskopf, J. J. Bock, H. Del Castillo, W. E. Holzapfel, L.E.. Lange, Appl. Opt. **36**, 765 (1997).

27. J. M. Gildemeister, A. M. Lee, P. L. Richards, Appl. Phys. Lett. **74**, 868 (1999).

28. A. D. Turner, J. J. Bock, J. W. Beeman, J. Glenn, P. C. Hargrave, V. V. Hristov, H. T. Nguyen, F. Rahman, S. Sethuraman, A. L. Woodcraft, Appl. Opt. **40**, 4921 (2001).

29. N. Tralshawala, S. Aslam, R. P. Brekosky, T. C. Chen, E. F. Felociano, F. M. Finkbeiner, M. J. Li, D. B. Mott, C. K. Stahle, C. M. Stahle, Nucl. Instr. Meth. Phys. Res. A **444**, 188 (2000).

30. T. May, V. Zakosarenko, R. Boucher, E. Kreysa, H.-G. Meyer, Supercond. Sci. Technol. **16**, 1430 (2003).

31. A. Tsamis, C. Tsamis,G. Kokkoris, E. Gogolides, and A. G. Nassiopoulou, J. Micromech. Microeng. **13**, 323 (2003).

32. B. Y. Cao and Z. Y. Guo, J. Appl. Phys. **102**, 05353 (2007).

33. Charles Kittel, *Introduction to solid state physics*, 8th ed., John Wiley & Sons, 2005.

34. G. P. Srivastava, *Physics of phonon*, Taylor & Francis Group, New York, 1990.

35. W. Weber, Phys. Rev. B **15**, 4789 (1977).

36. T. M. Tritt, *Thermal conductivity theory*, properties and application, Springer, 2004.

37. P. G. Klemens, in Solid State Physics, edited by. F. Seitz and D. turnbull, Academic Press Inc., New York, 1979.

38. G. A, Slack, Phys. Rev. **126**, 427 (1962).

39. H. M. Rosenberg, Phys. Soc. A **67**, 837 (1954).

40. C. J. Glassbrenner, and G. A. Slack, Phys. Rev. **122**, 1451 (1961).

41. J. T. Karvonen, and I. J. Maasilta, Phys. Rev. Lett. **99**, 145503 (2007).

42. T. Kühn, D. V. Anghel, J. P. Pekola, M. Manninen, and Y. M Galperin, Phys. Rev. B **70**, 125425 (2004).

43. M. M. Leivo and J. P. Pekola, Appl. Phys. Lett. **72**, 1 (1998).

44. S. M. Sze and M. K. Lee, *Semiconductor Devices* , 3rd ed., John Wiley & Sons, Singapore, 2013.

45. M. Nahum, T.M. Eiles, J.M. Martinis, Appl. Phys. Lett. **65**, 3123 (1994).

46. A. Luukanen, M. M. Leivo, J. K. Suoknuuti, A. J. Manninen, and J. P. Pekola, J. Low Temp. Phys. **120**, 281 (2000).

47. M. Yu. Reizer, Phys. Rev. B **40**, 5411 (1989).

48. F. Giazotto, T.T. Heikkilä, A. Luukanen, A.M. Savin, J.P. Pekola, Rev. Mod. Phys. **78**, 250 (2006).

49. M. M. Leivo, J. P. Pekola, D. V. Averin, Appl. Phys. Lett. **68**, 1996 (1996).

50. L. Salymar, *Superconductivity Tunneling and Applications*, Chapman and Hall, London, 1972.

51. F. C. Wellstood, C. Urbina, and J. clark, PRB **49**, 5942 (1994).

52. M. Yu. Reizer, Phys. Rev. B **29**, 3733 (1984).

53. P. Kski, P. Tivinen, A. Savin, M. Zgirski, P. Törmä, J.Pekola, M. Prunnila, and J. Ahopelto, JAP 94, 3201 (2003).

54. A. M. Savin, M. Prunnila, P. P. Kivinen, J. P. Pekola, J. Ahopelto, and A. J. Manninen, Appl. Phys. Lett. **79**, 1417 (2001).

55. F. Giazotto, T. T. Heikkil*ä*, A. Luukanen, A. M. Savin, and J. P. Pekola, Rev. Mod. Phys. **78**, 217 (2006).

56. M. Nahum, T.M. Eiles, J.M. Martinis, Appl. Phys. Lett. **65**, 3123 (1994).

57. M. M. Leivo, J. P. Pekola, D. V. Averin, Appl. Phys. Lett. **68**, 1996 (1996).

58. A. M. Clark, N. A. Miller, A. Williams, S. T. Ruggiero, G. C. Hilton, L. R. Vale, J. A. Beall, K. D. Irwin, J. N. Ullom, Appl. Phys. Lett. **86**, 173508 (2005).

59. J. T. Muhonen, M. Meschke and J. P. Pekola, Rep. Prog. Phys. **75**, 046501 (2012).

60. J. Karvonen, *Thermal properties in low dimentional strucres below 1K*, Ph.D. thesis. University of Jyväskylä, 2009.

61. A. M. Savin, M. Prunnila, P. P. Kivinen, J. P. Pekola, J. Ahopelto, A. J. Manninen, Applied Physics Letters **79**, 1471 (2001).

62. C. D. W. Wilkinson and M. Rahman, Phil. Trans. R. Soc. Lond. A **362**, 125 (2004).

63. M. Tinkham, *Introduction to Superconductivity*, 2nd ed,McGraw-Hill, New York, 1966.

64. Y. Shinba, K. Nakamura, M. Fukuchi, and M. Sakata, J. Phys. Soc. Jpn. **51**, 157 (1982).

65. P. M. Echternach, M. E. Gershenson, H. M. Bozler, A. L. Bogdanov, and B. Nilsson, Phys. Rev. B **48**, 11516 (1993).

66. M. Prunnila, J. Ahopelto, A.M. Savin, P.P. Kivinen, J.P. Pekola, A.J. Manninen, Physics E **13**, 773 (2002).

67. A. Savin, M. Prunnila, J. Ahopelto, P. Kivinen, P. Torma, and J. Pekola, Physica B **329**, 1481 (2003).

68. A. Savin, J. Pekola, M. Prunnila, J. Ahopelto, and P. Kivinen, Physica Scripta **T114**, 57 (2004).

69. A. K. M. Wennberg, S. N. Ytterboe, C. M. Gould, and H. M. Bozler, Phys. Rev. B **34**, 4409 (1986).

70. P. Kivinen, A. Savin, M. Zgirski, P. Törmä, J. Pekola, M. Prunnila, and J. Ahopelto, J. Appl. Phys. **94**, 3201 (2003).

71. A. Sergeev, and V. Mitin, Phys. Rev. B **61**, 6041 (2000).

72. A. Sergeev, M. Yu. Reizer, and V. Mitin, Phys. PRL **94**, 136602 (2005).

73. P. Yu, and M. Cardona, *Fundamentals of Semiconductors*, 3rd ed.,Springer-Verlag, Berlin, 2001.

74. P. Kivinen, *Electrical and thermal transport properties of semiconductor and metal structure at low temperature*, Ph.D. thesis. University of Jyväskylä, 2005.

75. M. J. Prest, J. T. Muhonen, M. Prunnila, D. Gunnarsson, V. A. Shah1, J. S. Richardson-Bullock, A. Dobbie, M. Myronov, R. J. H. Morris, T. E. Whall, E. H. C. Park, and D. R. Leadley, Appl. Phys. Lett. **99**, 251908 (2011).

76. J. T. Muhonen, M. J. Prest, M. Prunnila, D. Gunnarsson, V. A. Shah, A. Dobbie, M. Myronov, R. J. H. Morris,T. E. Whall, E. H. C. Parker, and D. R. Leadley, Appl. Phys. Lett. **98**, 182103 (2011).

77. M. Prunnila, P. Kivinen, A. Savin , P. Törmä , and J. Ahopelto, Phys. Rev. Lett. **95**, 206602 (2005).

78. G. Ghislotti, and C. E. Bottani, Phys. Rev.B **50**, 12131 (1994).

79. N. Perrin, and H. Budd, Phys. Rev. Lett. **28**, 1701 (1972).

80. K. Suzuki,and N. Mikoshiba, Phys. Rev. B **3**, 2550 (1971).

81. J. T. Karvonen, L. J. Taskinen, and I. J. Maasilta, Phys. Rev. Lett. **72**, 012302 (2005).

82. M. L. Roukes, M. R. Freeman, R. S. Germain, R. C. Richardson, and M. B. Ketchen, Phys. Rev. Lett. **55**, 422 (1985).

83. F. C. Wellstood, C. Urbina, and J. Clarke, Phys. Rev. B **49**, 5942 (1994).

84. M. E. Gershenson, D. Gong, T. Sato, B. S. Karasik, and A. V. Sergeev, Appl. Phys. Lett. **79**, 2049 (2001).

85. J. T. Karvonen, L. T. Taskinen, and I. J. Maasilta, Phys. Stat. Sol. **11**, 2799 (2004).

86. P. M. Echternach, M. E. Gershenson, H. M. Bozler, A. L. Bogdanov, and B. Nilsson, Phys. Rev. B **48**, 11516 (1993).

87. J. T. Karvonen, and I. J. Maasilta, Phys. Rev. Lett. **99**, 145503 (2007).

88. J. Parsons, *Relaxation of strained silicon on virtual substrates*, Ph.D. thesis. University of Warwick, 2007.

89. Vishal Ajit Shah, *Reverse Graded High Content (x>0.75) $Si_{1-x}Ge_x$ Virtual Substrates*, Ph.D. Thesis University of Warwick, 2009.

90. D. J. Dunstan, S. Young, and R. H. Dixon, J. Appl. Phys.**70**, 3038 (1991).

91. R. Peoule and J. C. Bean. Apply. Phys. Lett. **49**. 322 (1985).

92. W. T. Read Jr, Philos Mag. **45**, 1119 (1954).

93. J. Bardeen and W. Shockley, Phys. Rev. **80**, 72 (1950).

94. J. S. Koehler, Phys. Rev. **60**, 398 (1941).

95. D. L. Dexter, Phys. Rev. **85**, 936 (1952).

96. D. L. Dexter and F. Seitz, Phys. Rev. **86**, 964 (1952).

97. S. M. Sze, *VLSI Technology*, 2nd ed., McGraw-Hill, New jersey, 1988.

98. G. S. Oehiein, G. M. W. Kroesen, E. de Fr′esart, Y. Zhanhg, and T. D. Bestwick, J. Vac. Sci. Technol. A **9**, 768 (1991).

99. N. G. Einspruch, and G. Gildenblat, *Advanced MOS Device Physics*, Academic Press INC, California, 1989.

100. G. B. Bronner, MRS Proceedings 158, 1989.

101. U. W. Pohl, *Epitaxy of Semiconductor*, Springer, Berlin, 2013.

102. J. D. Cressler, *SiGe and Si strained-layer epitaxy for silicon heterostructure devices*, CRC Press & Tayolr francis Group, Boca Raton, 2008.

103. E. H. C. Parker, *The Technology and Physics of Molecular Beam Epitaxy*, Plenum Press, New York, 1985.

104. Y. Hamakawa, Y. Matsumoto, G. Hirata, and H. Okamoto, Mat. Res. Soc. Symp. Proc. **164**, 291 (1990).

105. M. du Plessis, J. Select. Topics Quantum Electron. **8**, 1412 (2002).

106. M. Belmonte, P. Ferro , A. J. S. Fernandes, F. M. Costa , J. Sacramento , R. F. Silva, Diamond Relat. Mater. **12**, 738 (2003).

107. C. R. Stoldt, C. Carraro, W. R. Ashurst, D. Gao, R. T. Howe, and R. Maboudian, Sensors Actuators A **97**, 410 (2002).

108. R. Ghodssi, and P. Lin, *MEMS Materials and Processes Handbook*, Springer, New York, 2011.

109. H. O. Pierson, *Handbook of Chemical Vapor Deposition*, Noyes Publications, Park Ridge, 1992.

110. J. I. Goldstein *et al*., *Scanning Electron Microscope and X-ray Microanalysis*, 2nd ed., Springer Science, 1992.

111. Y. Leng, *Materials characterization introduction to microscopic and spectroscopic methods*, John Wiley & Sons (Asia) Pte Ltd, Singapore, 2008.

112. R. C. Jaeger, *Introduction to Microelectronic Fabrication*, 2nd ed., Prentice Hall, 2002.

113. K. Jain, Electron. Devic. Lett. **3**, 53 (1982).

114. S. M. SZE, and M. K. Lee, *Semiconductor Device*, 3rd ed.,Wiley & Sons, Singapore, 2013.

115. Y. Taga, Surf. Coat. Tech. **112**, 339 (1999).

116. C. D. W. Wilkinson, and M. Rahman, Trans. R. Soc. Lond. A **362**, 125 (2004).

117. J. Krupka, Meas. Sci. Technol. **24**, 062001 (2013).

118. A. Kumar, J. B. M. Krishna, D. Das , and S. Keshri, Appl. Surf. Sci. **258**, 2237 (2012).

119. P. Prabukanthan , R. Dhanasekaran, Mater. Res. Bull **43**, 1996 (2008).

120. N. Roxhedao, F. Niklaus, A. C. Fischer, F. Forsberg, L. Höglund, and et al., in Proceedings of SPIE Vol. 7726, edited by F. Berghmans, A. G. Mignani, and C. A. van Hoof (Brussels, Belgium, 2010), 772611-1-772611-10.

121. L. Guo, K. Li, D. Liu, Y. Ou, J. Zhang, Qi. Yi, and S., J. Cryst. Growth. **801**, 227 (2011).
122. C. Claeys, and E. Simoen, *Germanium-based technologies* , Elsevier, Oxford, 2007.
123. S. Franssila, *Introduction to Microfabrication*, 2nd ed.,Wiley, New York, 2010.
124. M. A. Blauw, E. van der Drift, G. Marcos, and A. Rhallabi, J. Appl. Phys. **94**, 6312 (2003).
125. Q. Qian, W. Sun, D. Han, S. Liu, Z. Su, and L. Shi, Solid-State electron. **63**, 154 (2011).
126. T. Bao, Y. Bar, D. Fong, and M. Godbole, in Proceedings of SPIE, Vol. 6922, edited by J. A. Allgair, and C. J. Raymond (San Jose, CA, 2008), 69223G-1-69223G-8.
127. H.-B. Fang, J.-Q. Liu, Z.-Y. Xu, L. Dong, L. Wang, D. Chen, B.-C. Cai, and Y. Liude, Microelectr. J. **37**, 1280 (2006).
128. G. S. Oehrlein, Phys. Today **39**, 26 (1986).
129. R. d'Agostino, and D. L. Flamm, J. Appl. Phys. **52**, 162 (1981).
130. T. Syau, B. J. Baliga, and R. W. Hamaker, J. Electrochem Soc. **10**, 138 (1991).
131. H. Zou, Microsyst. Technol. **10**, 603 (2004).
132. R. Legtenberg, H. Jansen, M. de Boer, and M. Elwenspoek, J. Electrochem Soc. **142**, 2020 (1995).
133. K. -H. Shim, Y. -H. Kil, H. D. Yang, B. K. Park, S. Kang, T. S. Jeong, and T. S. Kim, Mat. Sci. Semicon. Proc. **15**, 364 (2012).
134. A. Campo, C. Cardinaud, and G. Turban, J. Vac. Sci. Technol. **13**, 235 (1995).
135. D. Korzec, T. Kessler, and J. Engemann, Appl. Surf. Sci. **46**, 299 (1990).
136. Z. Liu, Y. Wu, B. Harteneck, and D. Olynick, Nanotechnology **24**, 015305 (2013).
137. Y. H. Lee, and M. M. Chen, J. Vac. Sci. Technol B. **4**, 468 (1986).
138. C. J. Mogab, and H. J. Levinstein, J. Vac. Sci. Technol. **17**, 721 (1980).
139. Y. H. Lee, M. M. Chen and A. A. Bright, Appl. Phys. Lett. **46**, 260 (1985).
140. I. W. Rangelow, Surf. Coating Tech. **97**, 140 (1997).
141. A. M. Krings, K. Eden, H. Beneking, Microelectron. Eng. **6**, 553 (1987).
142. G . K. Fedder, R. T. Howe, T. J. K. Liu, and E. P. Quevy, Proc.IEEE **96**, 306, (2008).

143. M. C. Hoang, and K. Hane, Sensors Actuators A **165**, 422 (2011).
144. A. Nannini, D. Paci, F. Pieri, and P. Toscano, Sensors Actuators B **118**, 343 (2006).
145. N. A. Miller, G. C. O'neil, J. A. Beall, G. C. Hilton, K. D. Irwin, D. R. Schmidt, L. R. Vale, and J. N. Ullom, Appl. Phys. Lett. **92**, 1163501 (2008).
146. G. Kaltsas, and A. G. Nassiopoulou, Sensors and Actuators **76**, 133 (1999).
147. V. A. Shah, M. Myronov, C. Wongwanitwattana, L. Bawden, M. J. Prest, J. S. Richardson-Bullock, S. Rhead, E. H. C. Parker, T. E. Whall, and D. R. Leadley, Sci. Technol. Adv. Mater. **13**, 055002 (2012).
148. M. J. Griffin, Nucl. Instrum. Methods A **444**, 397 (2000).
149. J. S. Youa, D. Kimb, J. Y. Huhb, H. J. Parkc, J. J. Pakc, C. S. KangaJae ,Solar Energy Materials & Solar Cells **66**, 37 (2001).
150. V. A. Shah, A. Shchepetov, M. Myronov, M. J. Prest, M. Prunnila, C. Wongwanitwattana, T. E. Whall, E. H. C. Parker, and D. R. Leadley, *The Effects of Tensile and Compressive Strain on Ge Membranes,* 7th International Conference on Si Epitaxy and Heterostructures (ICSI-7), Leuven, Belgium, Sept. (2011).
151. S. Enderling, C. L. Brown, S. Smith, M. H. Dicks, J. Stevenson, M. Mitkova, M. N. Kozicki, J. W. Anthony, IEEE Trans. Semic. Manuf. **19**, 2 (2006).
152. J. M. Gildemeister, A. T. Lee, and P. L. Richards, Appl. Phys. Lett. **74**, 886 (1999).
153. J. J. Bock, D. Chen, P. D. Mauskopf, and A. E. Lange, Space. Sci. Rev. **74**, 229 (1995).
154. F. B. Kiewiet, M. P. Bruijn, H. F. C. Hoevers, A. C. Bento, W. A. Mels, and P. A. J. de Korte, IEEE Trans. Appl. Supercond. **9**, 1051 (1999).
155. O. Paul, P. Ruther, L. Plattner, and H. Baltes, IEEE Trans. Semicond. Manuf. **13**, 159 (2000).
156. M. M. Leivo, and J. P. Pekola, Appl. Phys. Lett. **72**, 1305 (1998).
157. M. Nahum, and J. M. Martinis, Appl. Phys. Lett. **66**, 3203 (1995).
158. C. S. Yung, D. R. Schmidt, and A. N. Cleland, Appl. Phys. Lett. **81**, 31 (2002).
159. O. G. Schmidt, K. Eber, Nature **410**,168 (2001).
160. E. Yang, *Microelectronic Devices*, New York, McGraw-Hill, 1988.

161. J. Hess, J. Schreiber, S. Hildebrandt, and R. Labusch, Phys. Status. Solidi. B **172**, 225 (1992).

162. S. A. Shevchenko, J. Exp. Theor. Phys. **88**, 66 (1999).

163. Yu. A. Osip'yan, V. I. Tal'yanskiĭ, A. A. Kharlamov, and S. A. Shevchenko, Sov. Phys. JETP **49**, 840 (1979).

164. R. Leoni, B. Buonomo, G. Castellano, F. Mattioli, G. Torrioli, L. Di Gaspare, and F. Evangelisti, Nucl. Instrum. Meth. A **520**, 44 (2004).

165. Minghao Shen, *Low Temperature Electron-Phonon Interaction in Disordered Metal Thin Films and Applications to Fast, SensitivenSub-Millimeter Photon Sources and Detectors*, PhD thesis, Yale University, 2005

166. L. J. Taskinen, J. T. Karvonen, and I. J. Maasilta, Nucl. Instrum. Meth. A **559**, 639 (2006).

167. P. P. Kivinen, A. M. Savin, M. Zgirski, P. Törmä, J. P. Pekola, M. Prunnila, and J. Ahopelto, J. Appl. Phys. **94**, 3201 (2003).

Appendix A

This appendix presents the measurement of step height for section 4.3 by using technique in section 3.4.3.

0% oxygen content	Si	Ge	Ge:P [L]	Ge:P [H]	PR
1	51.00	51.00	52.00	40.00	102.00
2	32.00	52.00	51.00	41.00	86.00
3	31.00	52.00	52.00	41.00	94.00
4	29.00	53.00	52.00	43.00	82.00
5	28.00	52.00	51.00	42.00	95.00
6	27.00	51.00	51.00	41.00	83.00
7	28.00	50.00	51.00	40.00	79.00
8	29.00	52.00	52.00	41.00	82.00
9	30.00	51.00	50.00	42.00	112.00
10	29.00	53.00	53.00	43.00	106.00
11	27.00	54.00	53.00	41.00	98.00
12	26.00	54.00	51.00	45.00	94.00
13	28.00	52.00	51.00	45.00	89.00
14	32.00	53.00	51.00	43.00	105.00
15	27.00	51.00	50.00	42.00	95.00
16	29.00	52.00	52.00	42.00	105.00
17	30.00	51.00	52.00	44.00	87.00
18	31.00	52.00	51.00	44.00	75.00
19	28.00	52.00	53.00	42.00	98.00
20	27.00	51.00	54.00	40.00	78.00
avergae (nm)	29.95	51.95	51.65	42.10	92.25
stadard deviation	5.25	1.05	1.04	1.55	10.60
Etching time (sec)	5.00	5.00	5.00	5.00	5.00
Etch Rate (nm/min)	359.40	623.40	619.80	505.20	1107.00

5% oxygen content	Si	Ge	Ge:P [L]	Ge:P [H]	PR
1	53.00	76.00	88.00	60.00	87.00
2	50.00	78.00	86.00	61.00	75.00
3	51.00	74.00	86.00	67.00	82.00
4	54.00	76.00	87.00	64.00	82.00
5	52.00	79.00	86.00	65.00	78.00
6	54.00	75.00	82.00	67.00	91.00
7	53.00	78.00	85.00	68.00	86.00
8	51.00	74.00	86.00	69.00	79.00
9	52.00	76.00	85.00	67.00	69.00
10	53.00	79.00	86.00	68.00	71.00
11	52.00	75.00	86.00	63.00	62.00
12	54.00	74.00	87.00	64.00	87.00
13	53.00	74.00	88.00	64.00	95.00
14	51.00	78.00	86.00	63.00	67.00
15	52.00	75.00	86.00	62.00	75.00
16	52.00	75.00	87.00	67.00	78.00
17	50.00	76.00	85.00	68.00	82.00
18	50.00	78.00	86.00	64.00	84.00
19	51.00	75.00	83.00	64.00	65.00
20	52.00	76.00	82.00	65.00	81.00
avergae (nm)	52.00	76.05	85.65	65.00	78.80
stadard deviation	1.30	1.70	1.66	2.53	8.76
Etching time (sec)	7.00	7.00	7.00	7.00	7.00
Etch Rate (nm/min)	445.71	651.86	734.14	557.14	675.43

20% oxygen content	Si	Ge	Ge:P [L]	Ge:P [H]	PR
1	139.00	67.00	63.00	60.00	67.00
2	141.00	66.00	69.00	62.00	71.00
3	145.00	64.00	75.00	63.00	78.00
4	146.00	64.00	69.00	61.00	43.00
5	145.00	62.00	70.00	62.00	67.00
6	145.00	62.00	67.00	61.00	73.00
7	142.00	61.00	69.00	58.00	62.00
8	142.00	64.00	65.00	59.00	60.00
9	143.00	63.00	70.00	58.00	57.00
10	142.00	63.00	77.00	62.00	49.00
11	143.00	60.00	78.00	62.00	53.00
12	143.00	59.00	75.00	62.00	67.00
13	140.00	59.00	72.00	62.00	61.00
14	141.00	60.00	78.00	61.00	65.00
15	138.00	61.00	77.00	61.00	46.00
16	138.00	61.00	72.00	61.00	58.00
17	141.00	63.00	74.00	62.00	57.00
18	141.00	63.00	74.00	62.00	61.00
19	140.00	62.00	74.00	64.00	48.00
20	142.00	61.00	72.00	61.00	62.00
avergae (nm)	141.85	62.25	72.00	61.20	60.25
stadard deviation	2.28	2.12	4.24	1.51	9.22
Etching time (sec)	30.00	30.00	30.00	30.00	30.00
Etch Rate (nm/min)	283.70	124.50	144.00	122.40	120.50

35% oxygen content	Si	Ge	Ge:P [L]	Ge:P [H]	PR
1	115.00	58.00	57.00	59.00	59.00
2	116.00	57.00	62.00	62.00	70.00
3	117.00	56.00	57.00	59.00	63.00
4	118.00	59.00	58.00	61.00	68.00
5	120.00	54.00	55.00	62.00	79.00
6	108.00	54.00	59.00	61.00	70.00
7	112.00	55.00	59.00	58.00	81.00
8	112.00	55.00	54.00	59.00	78.00
9	110.00	55.00	59.00	58.00	68.00
10	117.00	54.00	61.00	62.00	73.00
11	119.00	57.00	58.00	64.00	53.00
12	118.00	57.00	57.00	62.00	81.00
13	117.00	59.00	59.00	63.00	68.00
14	120.00	58.00	55.00	61.00	86.00
15	119.00	58.00	60.00	61.00	72.00
16	115.00	54.00	58.00	60.00	73.00
17	117.00	56.00	60.00	62.00	80.00
18	110.00	56.00	58.00	62.00	65.00
19	109.00	52.00	54.00	59.00	58.00
20	109.00	51.00	57.00	61.00	78.00
avergae (nm)	114.90	55.75	57.85	60.80	71.15
stadard deviation	4.01	2.20	2.18	1.67	8.71
Etching time (sec)	40.00	40.00	40.00	40.00	40.00
Etch Rate (nm/min)	172.35	83.63	86.78	91.20	106.73

50% oxygen content	Si	Ge	Ge:P [L]	Ge:P [H]	PR
1	106.00	166.00	164.00	162.00	180.00
2	112.00	167.00	162.00	162.00	184.00
3	109.00	168.00	166.00	154.00	172.00
4	115.00	162.00	165.00	157.00	186.00
5	112.00	158.00	168.00	154.00	197.00
6	110.00	156.00	168.00	155.00	175.00
7	106.00	159.00	165.00	153.00	189.00
8	110.00	160.00	167.00	152.00	169.00
9	112.00	161.00	165.00	161.00	173.00
10	109.00	157.00	169.00	161.00	183.00
11	109.00	156.00	168.00	160.00	170.00
12	110.00	161.00	167.00	152.00	165.00
13	112.00	158.00	167.00	154.00	168.00
14	115.00	162.00	168.00	156.00	179.00
15	110.00	161.00	168.00	156.00	191.00
16	115.00	156.00	168.00	153.00	174.00
17	108.00	157.00	165.00	157.00	190.00
18	109.00	162.00	165.00	158.00	180.00
19	115.00	162.00	164.00	159.00	159.00
20	114.00	165.00	167.00	159.00	192.00
avergae (nm)	110.90	160.70	166.30	156.75	178.80
stadard deviation	2.86	3.69	1.84	3.35	10.19
Etching time (sec)	120.00	120.00	120.00	120.00	120.00
Etch Rate (nm/min)	55.45	80.35	83.15	78.38	89.40

70% oxygen content	Si	Ge	Ge:P [L]	Ge:P [H]	PR
1	119.00	245.00	254.00	197.00	212.00
2	117.00	243.00	256.00	198.00	197.00
3	120.00	245.00	256.00	197.00	186.00
4	115.00	244.00	257.00	201.00	192.00
5	112.00	248.00	262.00	198.00	189.00
6	110.00	248.00	259.00	201.00	211.00
7	112.00	245.00	260.00	199.00	179.00
8	107.00	243.00	258.00	198.00	186.00
9	108.00	245.00	256.00	197.00	192.00
10	115.00	242.00	254.00	199.00	187.00
11	114.00	245.00	256.00	203.00	201.00
12	116.00	246.00	255.00	205.00	181.00
13	114.00	252.00	259.00	204.00	186.00
14	112.00	251.00	260.00	201.00	175.00
15	114.00	241.00	258.00	201.00	196.00
16	112.00	255.00	256.00	195.00	179.00
17	110.00	254.00	261.00	196.00	188.00
18	118.00	253.00	255.00	195.00	220.00
19	119.00	247.00	256.00	203.00	198.00
20	118.00	247.00	256.00	201.00	179.00
avergae (nm)	114.10	246.95	257.20	199.45	191.70
stadard deviation	3.74	4.07	2.31	2.95	12.09
Etching time (sec)	200.00	200.00	200.00	200.00	200.00
Etch Rate (nm/min)	34.23	74.09	77.16	59.84	57.51

90% oxygen content	Si	Ge	Ge:P [L]	Ge:P [H]	PR
1	44.00	124.00	124.00	129.00	460.00
2	41.00	126.00	126.00	130.00	456.00
3	44.00	125.00	125.00	128.00	440.00
4	43.00	122.00	122.00	130.00	485.00
5	42.00	120.00	123.00	129.00	453.00
6	41.00	119.00	125.00	128.00	472.00
7	43.00	119.00	124.00	129.00	463.00
8	42.00	121.00	124.00	130.00	459.00
9	40.00	123.00	123.00	128.00	471.00
10	43.00	120.00	122.00	130.00	466.00
11	43.00	121.00	121.00	128.00	449.00
12	45.00	119.00	124.00	128.00	478.00
13	45.00	121.00	125.00	129.00	464.00
14	40.00	119.00	125.00	129.00	460.00
15	42.00	120.00	122.00	128.00	468.00
16	41.00	119.00	125.00	125.00	471.00
17	41.00	120.00	123.00	127.00	452.00
18	43.00	119.00	122.00	128.00	451.00
19	42.00	120.00	122.00	126.00	475.00
20	43.00	120.00	122.00	129.00	449.00
avergae (nm)	42.40	120.85	123.45	128.40	462.10
stadard deviation	1.47	2.11	1.43	1.31	11.36
Etching time (sec)	600.00	600.00	600.00	600.00	600.00
Etch Rate (nm/min)	4.24	12.09	12.35	12.84	46.21

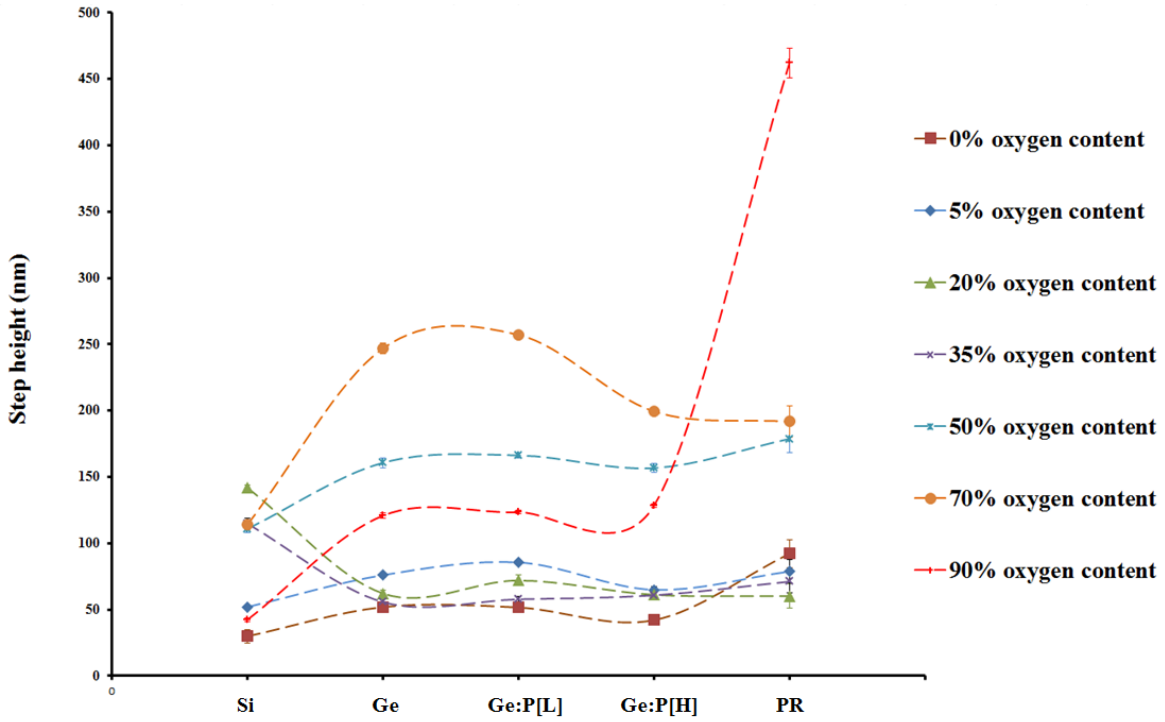
Step height (nm)
500
450
400
350
300
250
200
150
100
50
0
0
Si
Ge
Ge:P[L]
Ge:P[H]
PR
0% oxygen content
5% oxygen content
20% oxygen content
35% oxygen content
50% oxygen content
70% oxygen content
90% oxygen content

Appendix B

This appendix presents the measurement of angle of sidewall profile for section 4.4.

0% oxygen content	Si	Ge	Ge:P [L]	Ge:P [H]
1	25.12	23.71	27.25	38.95
2	24.85	23.76	27.26	38.82
3	24.46	24.21	27.24	38.90
4	24.37	23.54	27.53	39.25
5	24.56	23.52	27.14	38.58
6	24.76	23.68	27.12	38.76
7	25.08	23.75	27.08	38.82
8	24.76	23.72	27.10	39.12
9	24.72	23.76	27.12	38.45
10	24.32	23.45	27.08	38.48
11	24.36	23.42	27.24	38.56
12	24.58	23.45	27.02	38.82
13	24.38	24.11	27.12	38.59
14	24.76	24.12	27.02	39.21
15	24.56	23.56	27.42	38.85
16	24.56	23.56	27.06	38.72
17	24.76	23.48	27.08	38.94
18	24.76	23.76	27.15	38.56
19	24.65	23.56	27.24	38.92
20	25.12	23.48	27.06	38.72
avergae (degree)	24.67	23.68	27.17	38.80
stadard deviation	0.24	0.23	0.13	0.23

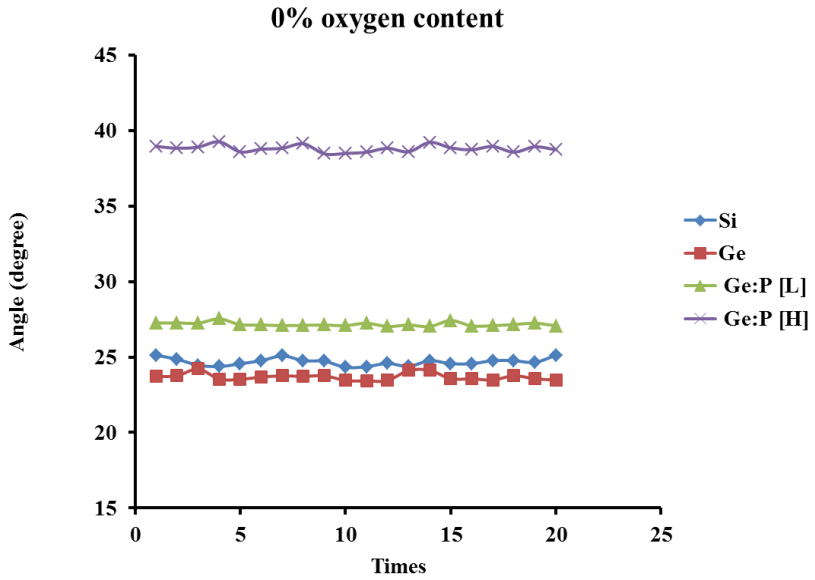

5% oxygen content	Si	Ge	Ge:P [L]	Ge:P [H]
1	44.26	37.24	32.39	41.95
2	44.21	37.82	32.35	41.82
3	44.62	37.62	32.22	41.54
4	44.56	37.24	32.76	41.56
5	44.35	37.25	32.51	41.62
6	44.76	37.34	32.45	41.69
7	45.12	37.78	32.78	41.23
8	45.10	37.45	32.34	41.21
9	44.68	37.80	32.12	41.67
10	44.45	37.56	32.45	41.78
11	44.70	37.20	32.45	41.45
12	44.78	37.45	32.50	41.56
13	44.56	37.44	32.45	41.45
14	44.81	37.65	32.26	41.60
15	44.56	37.78	32.68	41.45
16	44.21	37.76	32.34	41.12
17	44.56	37.21	32.68	41.45
18	44.81	37.31	32.56	41.42
19	44.23	37.24	32.71	41.45
20	44.56	37.24	32.24	41.56
avergae (degree)	44.59	37.47	32.46	41.53
stadard deviation	0.26	0.23	0.19	0.20

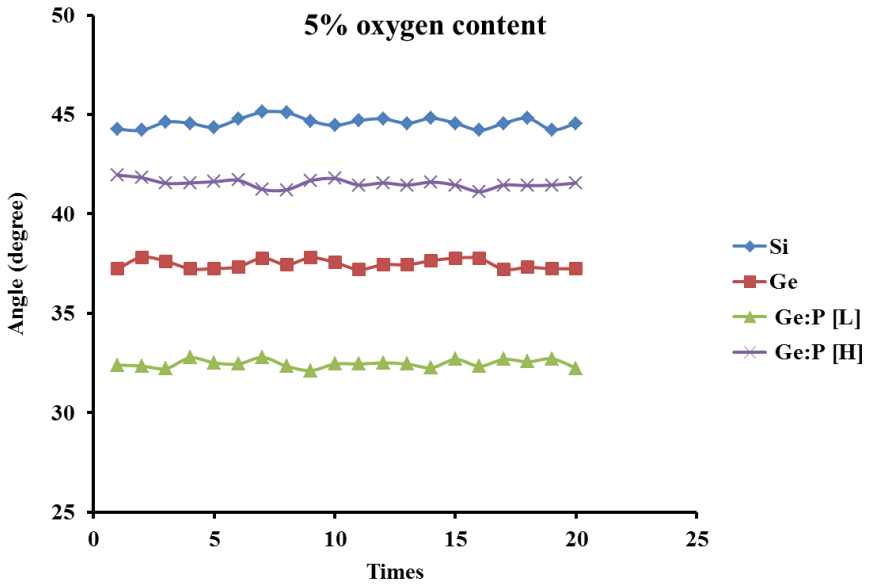

20% oxygen content	Si	Ge	Ge:P [L]	Ge:P [H]
1	85.54	85.24	86.78	85.12
2	84.92	85.56	86.96	85.23
3	85.34	89.45	88.24	84.46
4	85.34	90.02	87.24	84.56
5	85.14	86.34	89.91	84.21
6	85.23	89.12	90.23	85.21
7	89.45	86.12	90.45	86.75
8	84.78	85.12	87.24	89.20
9	85.22	85.78	86.24	89.15
10	85.67	86.78	86.80	84.86
11	85.78	86.23	88.12	84.22
12	89.20	86.12	90.00	90.00
13	89.23	85.42	90.00	89.95
14	84.23	89.23	89.50	85.14
15	84.45	89.20	86.24	85.26
16	84.38	85.23	86.78	84.24
17	89.56	85.78	89.72	84.22
18	84.24	85.78	89.50	89.10
19	90.00	89.55	86.24	85.75
20	89.50	90.21	86.22	85.56
avergae (degree)	86.36	87.11	88.12	86.11
stadard deviation	2.15	1.88	1.61	2.10

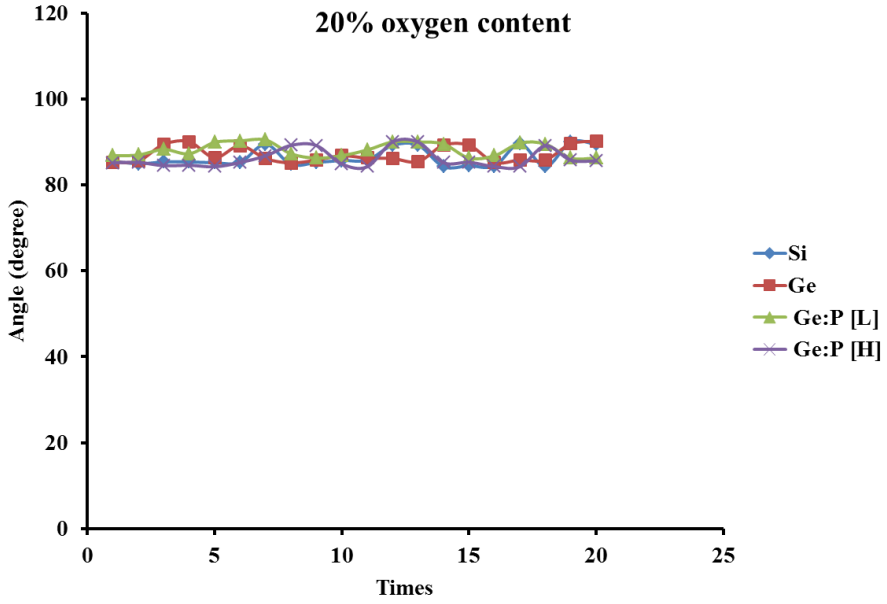

35% oxygen content	Si	Ge	Ge:P [L]	Ge:P [H]
1	105.56	108.92	112.78	124.98
2	105.60	108.95	112.42	124.92
3	105.34	109.21	112.78	125.15
4	105.89	108.45	112.85	124.98
5	106.02	108.21	112.12	124.98
6	105.78	108.95	112.64	125.12
7	106.43	108.21	112.78	124.85
8	105.44	108.45	113.08	124.84
9	105.78	108.45	112.95	124.85
10	105.65	108.56	112.64	125.12
11	106.12	109.22	112.98	124.86
12	105.34	108.45	112.34	124.92
13	105.45	109.12	112.52	124.95
14	105.24	108.97	112.45	124.98
15	105.45	108.65	112.98	124.86
16	105.22	108.45	113.12	124.45
17	105.56	108.24	112.45	124.45
18	106.24	108.56	112.21	124.85
19	106.45	109.12	112.26	124.98
20	105.12	108.82	112.26	124.98
avergae (degree)	105.68	108.70	112.63	124.90
stadard deviation	0.40	0.34	0.31	0.18

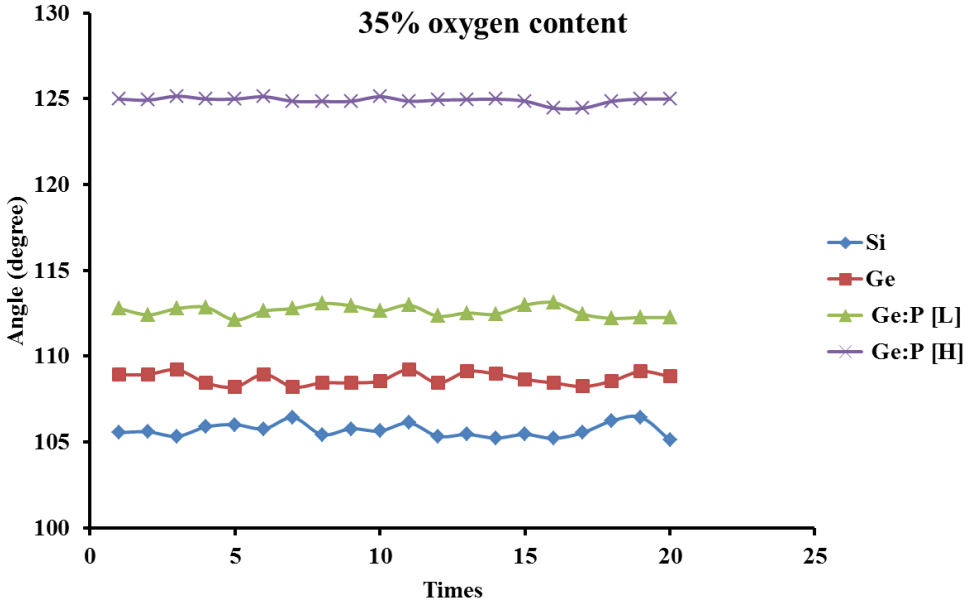

50% oxygen content	Si	Ge	Ge:P [L]	Ge:P [H]
1	120.22	122.80	117.50	127.45
2	120.45	122.98	117.45	127.28
3	119.98	122.45	117.50	126.80
4	120.12	122.28	117.28	126.59
5	120.50	122.48	117.28	126.61
6	120.52	122.98	117.95	126.84
7	120.24	123.12	117.84	126.87
8	120.24	122.21	117.45	126.90
9	120.50	122.56	117.76	126.45
10	120.26	122.68	117.56	126.75
11	120.24	122.70	117.84	126.42
12	119.98	122.45	117.85	126.45
13	120.05	122.56	117.45	126.78
14	120.18	123.24	117.25	126.25
15	120.25	122.45	117.80	126.80
16	120.50	122.56	117.95	126.78
17	120.45	122.80	117.50	127.24
18	120.12	122.24	117.21	126.10
19	120.26	122.45	117.30	126.11
20	120.28	122.90	117.86	127.28
avergae (degree)	120.27	122.64	117.58	126.74
stadard deviation	0.17	0.29	0.25	0.38

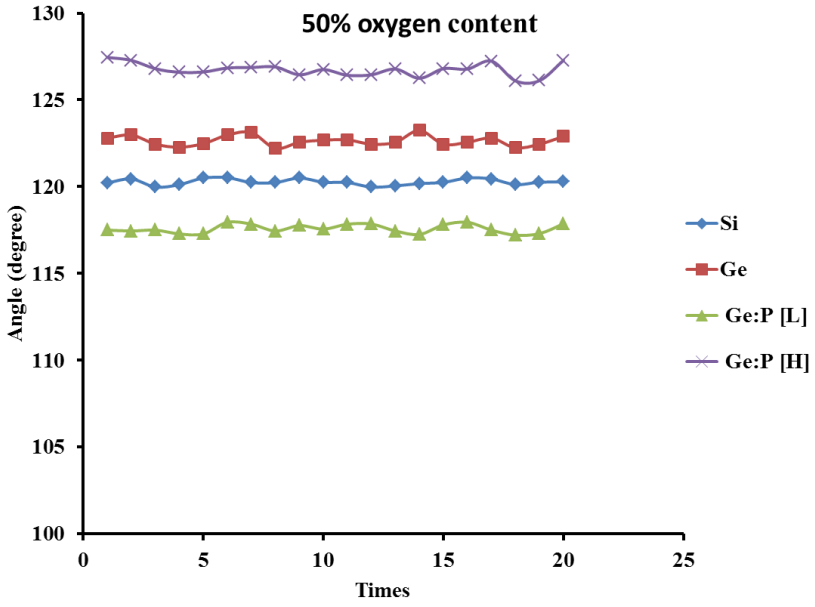

70% oxygen content	Si	Ge	Ge:P [L]	Ge:P [H]
1	152.68	126.20	126.95	133.12
2	152.90	126.11	127.10	132.84
3	153.12	125.98	126.85	132.60
4	152.84	126.25	126.98	132.78
5	152.45	126.45	127.05	132.75
6	152.58	125.95	126.95	132.65
7	152.25	126.14	126.75	132.95
8	152.81	126.45	127.12	132.50
9	152.55	126.50	126.95	132.38
10	152.89	125.98	126.75	132.47
11	152.45	126.25	126.89	132.82
12	152.42	126.30	126.91	133.00
13	152.11	126.41	126.92	132.98
14	152.60	126.22	126.06	132.45
15	153.12	126.25	126.98	132.60
16	152.98	126.45	126.95	132.75
17	152.56	126.20	126.91	132.57
18	152.21	126.24	127.01	132.81
19	152.80	125.95	126.85	132.45
20	152.45	126.11	126.89	132.80
avergae (degree)	152.64	126.22	126.89	132.71
stadard deviation	0.29	0.17	0.22	0.21

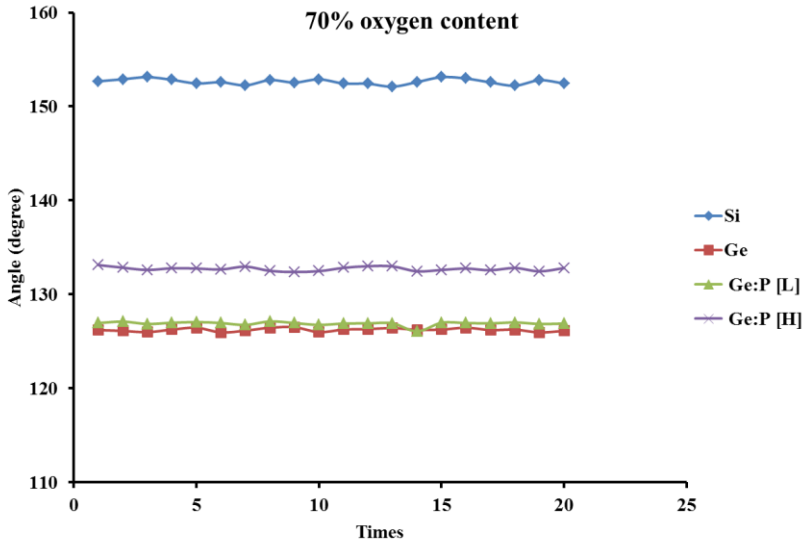

90% oxygen content	Si	Ge	Ge:P [L]	Ge:P [H]
1	166.75	162.91	160.21	152.60
2	166.98	162.90	159.95	152.55
3	166.45	163.05	159.74	152.47
4	166.70	162.86	160.20	151.95
5	167.10	162.94	160.05	152.45
6	166.95	162.95	159.92	151.96
7	166.40	163.01	159.75	152.65
8	166.45	162.85	160.10	152.79
9	166.90	162.91	159.55	152.54
10	166.58	162.74	160.22	152.42
11	166.50	162.89	159.82	151.98
12	166.45	162.95	160.25	152.24
13	166.75	162.87	160.07	152.68
14	166.95	162.92	160.05	152.51
15	167.05	163.06	160.25	152.42
16	166.25	162.45	160.25	152.41
17	166.45	162.98	160.01	152.56
18	166.75	163.11	160.11	152.68
19	166.81	162.71	160.24	152.56
20	166.35	162.52	159.92	152.70
avergae (degree)	166.68	162.88	160.03	152.46
stadard deviation	0.26	0.17	0.20	0.25